(2)

Borehole Electroseismic Phenomena: Field Measurements and Theory

by

Oleg Mikhailov

B.S., Physics, Moscow Institute of Physics and Technology (1991)
M.S., Mechanical Engineering, Dartmouth College (1993)

Submitted to the Department of
Earth, Atmospheric, and Planetary Sciences
in partial fulfillment of the requirements
for the degree of
Doctor of Philosophy in Geophysics

at the

MASSACHUSETTS INSTITUTE OF TECHNOLOGY

July 1998
[September 1998]

Signature of Author.....
Department of Earth, Atmospheric, and Planetary Sciences
July 27, 1998

Certified by.....
Professor M. Nafi Toksöz
Thesis Advisor

Accepted by.....
Professor Ronald G. Prinn
Chair, Department of Earth, Atmospheric, and Planetary Sciences

Borehole Electroseismic Phenomena: Field Measurements and Theory

by

Oleg Mikhailov

Submitted to the Department of Earth, Atmospheric, and Planetary Sciences
on July 27, 1998, in partial fulfillment of the requirements
for the degree of
Doctor of Philosophy

Abstract

A Stoneley wave propagating in a borehole generates a flow of pore fluid in permeable zones intersected by the borehole. In turn, this flow of pore fluid induces a streaming electrical field. This thesis is an experimental and theoretical investigation of the electrical fields induced by Stoneley waves. The main emphasis of this thesis is to understand the electroseismic phenomena that are observed in the field.

In the first experiment described in this thesis, we measured Stoneley-wave-induced electrical fields in a borehole drilled through fractured igneous rocks. Analysis of field data confirms that the electrical fields that we measured were induced by fluid flow in fractures. The normalized amplitude of these electrical fields correlated with the fracture density log.

In the second experiment, we measured Stoneley-wave-induced electrical fields in several boreholes in vuggy dolomite. In dolomite, the normalized amplitude of the Stoneley-wave-induced electrical field correlates with the porosity of the formation around the borehole. Further, the Stoneley-wave-induced electrical fields have anomalously high amplitudes at an isolated fracture that intersected two boreholes.

To explain the experimental results, we developed a theoretical model for the Stoneley-wave-induced electrical fields. According to the model, the normalized amplitude of the Stoneley-wave-induced electrical field is proportional to the porosity and inversely proportional to the pore space tortuosity of a formation around a borehole. Moreover, the amplitude-versus-frequency behavior of this electrical field depends on the permeability of the formation.

To further test the theory's prediction, we measured electrical potentials induced by the borehole Stoneley wave in the frequency range from $100Hz$ to $4kHz$. The normalized amplitudes of the Stoneley-wave-induced electrical potentials measured in the field were consistent with the amplitudes predicted by the theory. Also, the amplitude-versus-frequency dependence of the electroseismic signals recorded at the depth of the large fracture roughly followed the trend predicted by the theory. However, the general amplitude-versus-frequency dependence of the electroseismic signals recorded in the field is more complicated than that predicted by the theory.

The main contributions of this thesis are:

1. This thesis develops a borehole electroseismic measurement technique and demonstrates that it works in the field. This technique can be used to make electroseismic logging measurements.

2. This thesis investigates an electrical field induced by a borehole Stoneley wave. This electroseismic phenomenon is explained, measured in the field and modeled theoretically.

3. This thesis derives from field data a parameter that describes local electroseismic coupling in a formation around a borehole. This parameter, the normalized amplitude of the Stoneley-wave-induced electrical field, is defined as the ratio of an electrical field amplitude to a pressure amplitude in the Stoneley wave at a certain depth. This thesis demonstrates that the normalized amplitude of the Stoneley-wave-induced electrical field can be used to identify permeable fractures in situ.

4. This thesis uses field electroseismic measurements to quantitatively characterize rock formations around a borehole. Using the theoretical model developed in this thesis, a porosity log for fractured granite is derived from electroseismic field data.

Thesis supervisor: M. Nafi Toksöz
Title: Professor of Geophysics

Acknowledgment

This thesis is a result of efforts by many people and it is my pleasure to thank them all for the help and encouragement that I received during my five years at MIT.

First of all, I would like to thank my thesis advisor, Professor M. Nafi Toksöz for his support and guidance throughout my stay at MIT. The Earth Resources Laboratory, established by Professor Toksöz, has been a tremendous resource for me. No matter what technical or organizational problem I had, there always was someone within the lab who could help me with it. Also, being associated with such a reputable scientist as Professor Toksöz opened many doors and allowed me to collaborate with great scientists in academia and the oil industry.

This thesis would have been impossible without the help of Mr. Peter Britton of Hamilton, Massachusetts. I had the privilege to conduct field experiments at Mr. Britton's beautiful property. Mr. Britton encouraged me in my quest to characterize fractures, provided me with all the geophysical data on the site and always rescued me with his tractor whenever my truck got stuck in snow. I would like to thank Mr. Britton on behalf of all graduate students who have collected data for their thesis on his property.

Dr. John Queen of CONOCO, Inc. has given me tremendous support in my research. Together we worked on designing the measurement devices, making field measurements, interpreting the data and convincing other people that what we see is real. John and I became great friends and I hope to continue this friendship for many more years.

Dr. Dan Burns has always been a source of inspiration and encouragement for me. Dan helped me with the theoretical part of this thesis and with data analysis. Dan never allowed me to give up and always reminded me that the ultimate goal of one's life is to be happy.

At MIT, I had the privilege to meet and work with Professor Ted Madden. Ted helped me with developing the measurement technique, with the field experiments and processing the data. Ted also gave me great insights into the physics of the electroseismic phenomena. Ted has always encouraged me and I am grateful to him for that.

The foundation for the work described in this thesis was established with the help of Dr. Randall Mackie. During my second year at MIT I worked very closely with Randy on making electroseismic field measurements and on processing electroseismic data. Randy's help was crucial in unmasking the electroseismic signals from beneath

the noise that was hundreds of times stronger than the signal.

The experiment in Belvidere, Illinois was made possible by Dr. Frederick Paillet of USGS. Dr. Paillet supplied me with a great amount of supporting geophysical data and helped me with the data interpretation. I also would like to thank the Region V U.S. Environmental Protection Agency office in Chicago for providing funding for the field work and for providing access to the site.

Professor Gene Simmons gave me a lot of help with the Hamilton experiment. Professor Simmons provided geophysical data, gave great suggestions on how to understand the results of electroseismic experiments and was a source of moral support. I also would like to thank Hager-Richter Geoscience for the help in data acquisition and for acquiring geophysical logs for the Hamilton well.

This thesis was inspired by Dr. Matthijs Haartsen. Matthijs is a fascinating person with many great ideas. Following Matthijs' footsteps as a Ph.D. student at ERL was a great challenge for me. Early on I decided to make my thesis on electroseismic phenomena as different from his as possible. However, I have to confess that as time went by, I found myself reading his thesis more and more often.

I would like to thank Dr. Ernie Majer of Lawrence-Berkeley Laboratory and Dr. Tom Plona of Schlumberger-Doll Research for providing me with the equipment for the experiments.

I would like also to thank the following people for helping me with designing the experiment, processing the signals and interpreting the electroseismic data: Dr. Arthur Thompson of Exxon, Professor Gary Olhoeft of Colorado School of Mines, Dr. Roger Turpening of MIT, Dr. Rama Rao of MIT, Dr. Zhenya Zhu of MIT, Mr. John Beck of AMOCO, Dr. Ben Jeffryes of Schlumberger Cambridge Research, Professor Richard Gibson of Texas A&M University, Dr. Keith Katahara of ARCO, Professor Yves Bernabe of Institut de Physique de Globe, Mr. Sergei Osechinsky of Pacific Scanning, Inc., and Dr. Valentine Mikhailov of the United Institute of Physics of the Earth in Moscow.

I am also grateful to all my friends who helped me with field measurements: Mr. Vitaly Granovsky, Mr. Ivan Djikaev, Ms. Jennifer Sigmund, Dr. Grigory Boubnov, Dr. Svetlana Panasyuk, Dr. Dmitry Kroujiline, Mr. Alexander Zelikin, Dr. Viktor Oancea, and Lt. Scott Carter (USAF). This thesis would have not been possible without their help.

During the five years that I spent at ERL I have received great help and encouragements from Sue Turbak, Sara Brydges, Liz Henderson, Naida Buckingham and

Lori Weldon. They not only dealt with my manuscripts, purchase orders, letters and etc, but also wiped my tears and shared my smiles. I really thank them for making ERL a warm and friendly place.

I would like to thank my officemates Tony Sena, Francesca Scire-Scapuzzo, Hafiz Alshammery, Kate Jesdale and Phil Reppert for their friendship. I would like to especially thank Francesca for the great years that we were officemates. Francesca's friendship is one of the most important things that I gained at MIT. I only wish is that we stayed officemates longer. I want also to thank Kate Jesdale for making me smile during the most difficult times.

My technical writing has been greatly improved with the help of Ms. Kate Jesdale, Dr. Karen Muller, Mr. Chuck Doll, Dr. Shirley Rieven, Dr. Rob Reilinger, Dr. William Rodi and Dr. Joe Matarese. I would like to thank Dr. Matthias Imhof, Dr. Joe Matarese, Ms. Jane Maloof and Mr. Chuck Doll for helping me to tame wild computers by which I am sometimes intimidated.

I would like to thank all my fellow students and visiting scientists at ERL for all the things that we shared at MIT and for loading the heavy equipment into the truck: Jon Kane, Franklin Ruiz, Bob Greaves, Tony Delilla, Maria Perez, Jie Jang, Yulia Garipova, Mary Krasovec, Xiaojun Huang, Wei Chen, Feng Shen, Jesus Sierra, David Cist, Bertram Nolte, Weiqun Shi, Matthias Imhof, Shirley Rieven, John Sogade, Yervant Vichabian and John Olson.

Finally, I would like to thank my girlfriend Jennifer for all that she has endured during the last two years of my Ph.D. program. Her love and support kept me sane during the most crazy times. I always kept telling her that once I defend my thesis, everything will become normal. Now the thesis has been defended but it does not seem that craziness is subsiding. I am starting to wonder whether it had anything to do with the thesis in the first place...

Contents

1 Introduction **13**

1.1 The main goal of the thesis 13

1.2 Electroseismic phenomena and their possible applications 14

1.2.1 Electroseismic phenomena as a method for measuring streaming potentials in situ 15

1.2.2 Electroseismic phenomena as a method for detecting seismic-wave-generated flow of pore fluid 18

1.3 Previous studies of electroseismic phenomena 21

1.4 Thesis outline and summary of results 26

2 Low-frequency measurements of electrical fields induced by borehole Stoneley waves **34**

2.1 Electroseismic phenomena caused by a borehole Stoneley wave 35

2.1.1 Electrical field induced by a Stoneley-wave-generated fluid flow in permeable formations 35

2.1.2 Electrical field and electromagnetic radiation generated by a Stoneley wave at an isolated fracture 37

2.2 Borehole electroseismic measurements in fractured igneous rocks . . . 38

2.2.1 Experimental site 39

2.2.2 Field experimental procedure 40

2.2.3 Noise reduction in the electrical data 41

2.2.4 Full-waveform electroseismic data 42

2.3 Analysis of the Stoneley-wave-induced electrical fields in fractured igneous rocks 44

2.3.1 Definition of the normalized amplitude of the Stoneley-wave-induced electrical fields 44

2.3.2 Analysis showing that the Stoneley-wave-induced electrical fields are caused by the fluid flow in fractures 46

2.3.3 Summary: using borehole electroseismic measurements to identify fractured zones 48

2.4 Borehole electroseismic measurements in dolomite: general description of the experimental site 49

2.4.1 Permeable zones in the subsurface and estimates of their hydraulic transmissivity 50

2.4.2 Porosity measurements 51

2.4.3 Borehole televiewer images of a fracture and vugs in dolomite 52

2.4.4 Gamma, resistivity and SP measurements 53

2.4.5 Correlation of the formation properties between different boreholes 55

2.5 Borehole electroseismic measurements in dolomite: data and its interpretation 56

2.5.1 Field experimental procedure 56

2.5.2 Full-waveform electroseismic data 56

2.5.3 Borehole T6 57

2.5.4 Borehole T7 60

2.5.5 Borehole T2 61

2.5.6 Borehole T1 62

2.5.7 Summary of the results of the dolomite experiment 64

2.6 Conclusions 65

3 Theoretical model for the Stoneley-wave-induced electrical field 98

3.1 Stoneley-wave-induced electrical field in a homogeneous, porous, permeable formation 99

3.1.1 Pressure distribution in the borehole and in the formation around the borehole created by the Stoneley wave 99

3.1.2 Streaming and conducting electrical currents induced by pore fluid flow in the formation 100

3.1.3 The analytical solution for the amplitude of the electrical field induced by the Stoneley wave 101

3.1.4 Comparison of the amplitudes predicted by the theoretical model to the amplitudes measured in granite 102

3.1.5 Consistency of the theoretical model with the field measurements in dolomite 103

3.2 Determining porosity from the normalized amplitude of the Stoneley-wave-induced electrical fields at low frequencies 105

3.2.1 Deriving a porosity log for granite from the electroseismic field data 105

3.3 High amplitude anomaly at the isolated fracture in dolomite: the tortuosity effect 107

3.4 Determining permeability from the amplitude-versus-frequency behavior of the Stoneley-wave-induced electrical potential 109

3.4.1 Permeability dependence of the electroseismic coupling coefficient for the rock formation 110

3.4.2 Modification of electrical potential amplitude by the borehole presence: $\frac{\sigma_f}{\sigma_r}$ effect 113

3.5 Relationship between the amplitude of the Stoneley-wave-induced electrical field and the lithology 115

3.6 Conclusion 117

4 Electroseismic logging: broadband measurements of the Stoneley-wave-induced electrical potential 123

4.1 Introduction 123

4.2 Electroseismic logging technique 125

4.2.1 Stoneley wave source 125

4.2.2 Electrode configuration and the noise reduction processing . . 126

4.3 Field experiment 128

4.3.1 Experimental site 128

4.3.2 Field experimental procedure 129

4.3.3 Full-waveform electroseismic data 131

4.4 Analysis of the Stoneley-wave-induced electrical potential 133

4.4.1 Deriving the normalized amplitudes of the Stoneley-wave-induced electrical potential at different frequencies from the field data 134

4.4.2 Comparing the amplitude of the Stoneley-wave-induced electrical potential with other geophysical measurements 135

4.5 Comparison of the field data and theory: amplitude-versus-frequency dependence of the Stoneley-wave-induced electrical potential 136

4.5.1 Synthetic amplitude-versus-frequency curves for the Stoneley-wave-induced electrical potential 136

4.5.2 Comparison between the synthetic curves and the field data . 137

4.6 Discussion 138

4.7 Conclusion 140

5 Conclusions **158**

5.1 Suggestions for future work 161

A Analysis of the electrical signals generated by the Stoneley wave's action on the electrodes or on the borehole wall **174**

A.1 Electrical signals due to the electrode motion induced by the Stoneley wave 175

A.2 Streaming potentials due to the fluid motion along the borehole wall . 176

A.3 Streaming potentials due to the fluid motion along the surface of the electrodes 177

B Solution for the amplitude and phase of the Stoneley-wave-induced electrical field **179**

C Analysis of the mysterious electrical signal M-M **182**

D Sensitivity functions of the 4 and 2-electrode measurements **186**

D.1 Relationships between the amplitude of the electrical potential oscillation and the amplitudes of the signals measured using the 4-electrode array 186

D.2 Relationships between the amplitude of the electrical potential oscillation and the amplitudes of the signals measured using the 2-electrode arrays 188

E Instrument response of the measuring devices **193**

Chapter 1

Introduction

1.1 The main goal of the thesis

Detection and characterization of permeable zones in the subsurface is an important challenge for geophysical exploration. In this thesis we investigate a new method for detecting and characterizing permeable zones around a borehole. In our experiments, a Stoneley wave propagating in a borehole creates an oscillating pressure gradient in a rock formation around the borehole. If a formation is permeable, then this pressure gradient generates a flow of pore fluid. We detect this flow of pore fluid by measuring the streaming electrical field that it induces [1]. Thus, our method utilizes electroseismic phenomena (i.e., electrical fields induced by seismic waves) to characterize rock formations around a borehole.

[1] Recently, a method for determining formation permeability from Stoneley wave attenuation has been developed (Winkler *et al.*, 1989; Tang *et al.*, 1991). In this method, a Stoneley-wave-generated fluid flow in a formation around a borehole is detected by measuring the attenuation of the Stoneley wave that is caused by the flow. Our electroseismic method uses a different physical phenomena to detect the Stoneley-wave-generated fluid flow.

Electroseismic phenomena in porous media are very complex. They involve processes on scales from $10^{-8}m$ (the charged double layer in the vicinity of the pore surfaces) to $10^{-6}m$—$10^{-3}m$ (sizes of pores where fluid flow takes place) to $1m$—$10^{2}m$ (lengths of seismic waves that generate the fluid flow). To understand the electroseismic phenomena one has to study chemistry (to describe the adsorption of ions to the pore surfaces), thermodynamics (to determine the distribution of ions in the vicinity of the pore surfaces), fluid mechanics (to describe fluid flow on the pore scale) and poroelasticity theory (to understand how a seismic wave generates a pore fluid flow). This thesis does not intend to give a full description of all aspects of the electroseismic phenomena because each of them can be a subject of a separate monograph. This thesis intends to demonstrate the practical use of the electroseismic phenomena in geophysical exploration, given the present day understanding of what electroseismic phenomena are.

1.2 Electroseismic phenomena and their possible applications

The simplest way to understand electroseismic phenomena is as follows. A seismic wave propagating in a porous medium generates a flow of pore fluid. In turn, this flow of pore fluid induces a streaming electrical field. Numerous monographs have been written on wave propagation in porous media and on streaming potentials induced by fluid flows. Comprehensive reviews of these two subjects were written by Bourbie *et al.* (1987) and Morgan (1989). Instead of replicating these reviews, we will describe a few unique applications of electroseismic phenomena. These applications are feasible only because electroseismic phenomena combine streaming potentials and acoustics of porous media.

1.2.1 Electroseismic phenomena as a method for measuring streaming potentials in situ

Fluid flow through porous rocks induces a streaming electrical field [2] because the pore fluid saturating the rocks carries an excess electrical charge. This electrical charge is accumulated in the pore fluid because surfaces of most minerals adsorb ions of a certain polarity from the pore fluid, leaving an excess of ions of the opposite polarity in the fluid (Bockris and Reddy, 1970). For example, in quartz-bearing rocks filled with water, rock surfaces adsorb negative ions, leaving an excess positive electrical charge in water. The excess electrical charge within the pore fluid is concentrated in a thin layer along the pore surfaces. Whenever a pressure gradient forces the pore fluid to flow through the rock, the fluid displacement along the pore surfaces moves this excess electrical charge, thus creating a streaming electrical current. This streaming electrical current results in induction of an electrical field.

In the field, streaming potentials are traditionally used to detect large-scale flows such as water seepage through dams (Armbruster *et al.*, 1989) or hydrothermal convection (Hashimoto and Tanaka, 1995). Wurmstich and Morgan (1994) proposed to use streaming potentials to monitor oil well pumping and hydro-fracturing. Mizutani *et al.* (1976) proposed to use streaming potentials induced by fluid flow in a fault zone as a means for earthquake prediction. None of these applications have been established yet. In oil exploration, streaming potentials are measured as a part of a Self-Potential log. Even though the Self-Potential logs can identify permeable zones, the contribution of streaming potentials to the Self-Potential signals is small (Desbrandes, 1985).

A number of theoretical and laboratory studies showed that streaming potentials

[2] We would like to emphasize here that the terms streaming electrical potentials and streaming electrical field refer to the same phenomenon.

can be used to characterize porous rocks. Traditionally, the goal of these studies is permeability estimation. Theoretical studies (e.g., Pride, 1994 and Bernabe, 1998) related the streaming potential coupling coefficient (i.e., the ratio of the induced electrical potential to the applied pressure gradient) to the pore geometry of a medium and to salinity and conductivity of the pore fluid. The general consensus of the theoretical models is that the DC streaming potential coupling coefficient does not change with permeability, except for very tight rocks, where surface conductivity effects become important. Sprunt *et al.* (1994) measured the streaming potential coupling coefficient on a number of limestone samples and reported no variation of the coupling coefficient with permeability. Jouniaux and Pozzi (1995) reported a slight increase of the streaming potential coupling coefficient with permeability in their sandstone and limestone samples. Jouniaux and Pozzi (1995) attributed their results to a surface conductivity effect and used a simple theoretical model to validate their conclusion.

Even though at low frequencies there is no direct relationship between the streaming potential coupling coefficient and permeability, it is still possible to estimate permeability using streaming potentials. The following three methods have been proposed.

1. Chandler (1981) proposed to estimate permeability from the decay time of a pore pressure pulse applied to a porous medium. In laboratory experiments he used streaming potentials to observe time-varying fluid flow induced in a porous sample by a pressure pulse. Chandler (1984a,b) patented a borehole apparatus for permeability logging based on his method.

2. Po-zen Wong and colleagues (Pengra *et al.*, 1995; Li *et al.*, 1995) proposed to determine permeability from measuring the conductivity, streaming potential coupling coefficient and electro-osmosis coupling coefficient of a porous medium. Electro-

osmosis, i.e., fluid flow generated in a porous medium by an applied electrical field, is a reverse phenomenon of streaming potentials. Li *et al.* (1995) successfully determined permeability for a number of rock samples from the combination of these three media parameters. Wong (1995) patented his method and a borehole apparatus for permeability measurements.

3. Pride's (1994) model predicts that the frequency behavior of the streaming potential coupling coefficient depends on permeability. Reppert and Morgan (1998) measured the streaming potential coupling coefficient at different frequencies in a porous filter and a sandstone sample. Their results validate Pride's (1994) model. No borehole measurement technique that is used on Pride's (1994) model has been patented. It has not been clear how the frequency dependence of the streaming potential coupling coefficient can be measured in situ.

The studies referenced above demonstrate that streaming potential measurements can have important applications in oil exploration and environmental geophysics. However, all these methods were implemented only in the laboratory. Borehole methods patented by Chandler (1984a,b) and Wong (1995) have not been implemented in the field because they are based on establishing a hydrodynamically sealed contact between an apparatus and a rock formation in a borehole. Unfortunately, rock surfaces in boreholes are rarely polished as nicely as surfaces of laboratory samples. Without establishing a hydrodynamically sealed contact, it is not possible to initiate fluid flow in a formation in a controlled manner. Thus, measurements of streaming potentials initiated by a controlled source have never been made in the field.

Electroseismic phenomena provide a method for measuring streaming potentials initiated by a controlled source. Thus, by using these phenomena it is possible to implement the methods proposed by Chandler (1984b), Wong (1995) and Pride (1994) in reality. In electroseismic experiments the amplitude of a seismic wave can be mea-

sured simultaneously with the amplitude of the streaming potential that it induces. A combination of seismic and electrical measurements can be used to estimate the streaming potential coupling coefficient in situ. Moreover, by varying the frequency of a seismic source, it is possible to estimate the frequency dependence of the streaming potential coupling coefficient. In turn, in situ measurements of the streaming potential coupling coefficient can be used to characterize rock formations.

1.2.2 Electroseismic phenomena as a method for detecting seismic-wave-generated flow of pore fluid

The general equations describing the acoustics of porous media were derived by Biot (1956a,b, 1962). [3] Biot's equations are based on the assumption that stresses and strains in solid and fluid are linearly related (Biot, 1941; Biot and Willis, 1957) and the assumption that an oscillating force and an oscillating relative displacement between solid and fluid are linearly related (Schmitt, 1986). [4] Thus, in their general form (i.e., with complex, frequency-dependent moduli, permeability and tortuosity), Biot's equations are applicable to a variety of media. For a specific medium, moduli, permeability and tortuosity depend on the geometry of the pore space. Pore-geometry-dependent moduli for specific examples of fluid-saturated media were derived by Kuster and Toksöz (1974) and O'Connel and Budiansky (1977). General expressions for frequency-dependent permeability and tortuosity were derived by Johnson *et al.* (1987).

[3] For the sake of fairness, we need to mention that 12 years before Biot, Frenkel (1944) derived almost the same set of equations, except for one term - Frenkel (1944) did not consider inertial coupling between solid and fluid. Thus, Frenkel's (1944) equations are a special case of Biot's equations for a medium with a tortuosity of 1. Using his equations, Frenkel (1944) predicted the existence of two compressional waves and the attenuation of waves due to fluid flow. Biot was fully aware of Frenkel's results when he wrote his papers (Biot, 1956a,b).

[4] The latter linearity assumption is equivalent to Biot's postulate of quadratic kinetic energy and dissipative functions.

The Biot theory describes pore fluid flow generated by seismic waves and the attenuation associated with it. The seismic-wave-generated fluid flows are very small and cannot be observed directly. However, it is possible to detect these fluid flows by measuring the streaming electrical field that they induce. Figure 1-1 shows a diagram of a streaming electrical field induced by a compressional wave. A compressional wave propagating in a fluid-saturated porous rock creates a pressure gradient that drives the fluid flow from the zone of compression to the zone of extension. If the pore fluid carries an excess positive electrical charge, then the flow results in accumulation of a positive electrical charge in the zone of extension and a negative electrical charge in the zone of compression. This charge separation induces an electrical field that travels with the compressional wave.

Figure 1-2 shows results of surface electroseismic measurements at a site near Walden Pond, Massachusetts. Figure 1-2 shows that electrical field oscillations are induced by both a *P*-wave and a surface wave. The first motion of the *P*-wave is compressional and the "first motion" of the electrical field is negative. This result is consistent with the diagram in Figure 1-1. This experiment is a simple illustration for the idea of detecting seismic-wave-generated fluid flows by measuring the streaming electrical field that it generates.

The Biot theory predicts a second compressional wave in the medium that is referred to as the Biot slow wave. This wave attenuates rapidly in the medium due to the large fluid-solid displacements that it induces (Biot, 1956a,b). Biot slow waves have been observed only in laboratory experiments on synthetic media (Plona, 1980) and have not been observed in the field. However, when a fast compressional wave crosses an interface between two media, it generates a flow of pore fluid across the interface. In turn, this flow generates a slow compressional wave. The theoretical analysis of Gurevich and Lopatnikov (1995) demonstrated that fast compressional waves can be significantly attenuated in finely layered porous media due to fluid flow

across interfaces. The theoretical results of Gurevich and Lopatnikov (1995) have not been supported by field data because it has not been possible to observe directly this seismic-wave-generated fluid flow across interfaces in the subsurface.

Electroseismic phenomena in porous media can be used to detect fluid flow across an interface at the time when a fast compressional wave crosses it. Figure 1-3 is an illustration of the phenomenon called electroseismic conversion. Electroseismic conversion is the generation of an an electromagnetic wave by a compressional wave crossing an interface between two media. If the medium above the interface has a soft frame and the medium below has a hard frame, then the compressional wave creates higher pore pressure in the medium above the interface than in the medium below. The difference in pore pressure across the interface drives fluid flow from the medium above the interface to the medium below. This flow results in accumulation of a positive electrical charge below the interface and of a negative electrical charge above. This charge separation across the interface generates an electromagnetic wave that can be recorded on the surface (Figure 1-3). Figure 1-4 shows results of an experiment where such electromagnetic waves were recorded in the field. Figure 1-4 demonstrates that electroseismic measurements allow detection of fluid flow across an interface at the time when a compressional wave crosses it. The details of this experiment and results of numerical simulations of the field data are described in a paper by Mikhailov, Haartsen and Toksöz (1997).

The two examples that we described in this section demonstrate that studying electroseismic phenomena can contribute to understanding Biot-type attenuation of seismic waves in homogeneous media and at interfaces. In turn, understanding the attenuation of seismic waves is important for seismic exploration.

1.3 Previous studies of electroseismic phenomena

Various applications for electroseismic phenomena have been envisioned a long time ago. However, these phenomena were investigated in a very small number of studies. Electroseismic phenomena in porous media were first detected in the field by Ivanov (1939). Ivanov's (1939) experiments inspired Frenkel (1944) to develop the first theoretical model for electroseismic phenomena in porous media. The first laboratory observations of electroseismic phenomena in porous rocks were made by Antsyferov (1958) [5].

Until very recently, theoretical, laboratory and experimental investigations of electroseismic phenomena were completely independent. The most progress has been achieved in theoretical modeling. Frenkel (1944), Neev and Yeatts (1989) and Pride (1994) proposed various sets of equations that described electroseismic phenomena. Pride's (1994) set of equations is the most complete of these three. Pride (1994) combined Biot's and Maxwell's equations and also derived frequency-dependent coupling coefficients that relate pore fluid flow with electrical current. Pride and Haartsen (1996) have obtained plane-wave and point-source solutions for Pride's (1994) equations in a homogeneous medium. Pride and Haartsen (1996) predicted that in homogeneous media slow and fast compressional waves induce electrical fields and shear waves induce magnetic fields. Haartsen and Pride (1997) incorporated the plane-wave solutions of Pride and Haartsen (1996) into a numerical algorithm and numerically simulated acoustic and electromagnetic waves generated in a layered medium by a point explosion source. Their numerical calculations simulated electroseismic conversion at mechanical and fluid salinity contrasts. Haartsen and Pride (1997) simulated

[5] In the literature on electroseismic phenomena, terms *electroseismic* and *seismoelectric* are used interchangeably. In Russian literature the convention is to refer to electrical fields induced by seismic waves as a *seismoelectric* phenomena and to seismic waves induced by electrical fields as *electroseismic* phenomena. In order to add to the confusion, we refer to the electrical fields induced by seismic waves as *electroseismic* phenomena, which is opposite to the Russian convention.

both surface acquisition and VSP geometries. Haartsen *et al.* (1998) used Pride's (1994) model to investigate the sensitivity of the streaming electrical current induced by compressional and shear waves to various media properties.

Laboratory experiments on electroseismic phenomena can be divided into two groups. Experiments in the first group investigated electrical fields induced in vibrating porous samples (Antsyferov, 1958; Parkhomenko and Tsze-San, 1964; Chien-San and Zangirov, 1965; Antsyferov, 1966; Parkhomenko and Gaskarov, 1971; Gaskarov and Parkhomenko, 1974; Parkhomenko *et al.*, 1975; Chernyak, 1975, 1976; Migunov and Kokorev, 1977; Simonyan, 1985; Parkhomenko *et al.*, 1986; Simonyan, 1987; Migunov *et al.*, 1993; Mironov *et al.*, 1993; Parkhomenko and Topchian, 1994; Migunov *et al.*, 1995). In this group of experiments the relationship between the electroseismic amplitudes and various rock and fluid properties were investigated. We will summarize the most important conclusions that were made based on their results.

1. When water that saturates sandstone samples is frozen, no electroseismic signals can be detected (Gaskarov and Parkhomenko, 1974).

2. In general, the amplitude of electroseismic signals depends on the rock type. For example, it is higher in limestones than in sands (Gaskarov and Parkhomenko, 1974).

3. The amplitude of the electroseismic signals decreases with increasing salinity of water saturating the samples (Parkhomenko and Gaskarov, 1971; Gaskarov and Parkhomenko, 1974; Simonyan, 1987).

4. In sandstone samples saturated with a mixture of water and kerosene, the amplitude of electroseismic signals decreases with increasing kerosene content (Mironov *et al.*, 1993).

5. In partially saturated rocks, the amplitude of electroseismic signals first sharply increases with saturation and then decreases (Parkhomenko and Tsze-San, 1964; Chien-San and Zangirov, 1965; Parkhomenko and Gaskarov, 1971; Gaskarov and Parkhomenko, 1974).

6. In partially saturated shaly sandstones with approximately the same porosity, the amplitude of the electroseismic signals decreases with permeability (Parkhomenko *et al.*, 1975). [6]

7. The amplitude of the electroseismic signals increases with porosity (Migunov and Kokorev, 1977).

All these results can be explained within the current models of electroseismic coupling (e.g. Pride, 1994) and streaming potentials (e.g., Morgan *et al.*, 1989). We summarized these laboratory results results to give an idea of the complexity of electroseismic phenomena and their interpretation.

In the second group of experiments, emphasis was placed on simulating field acquisition geometries. Zhu *et al.* (1994) recorded electrical signals induced by P-waves and Rayleigh waves in a porous sample. Haartsen *et al.* (1995) simulated surface acquisition geometry and recorded an electroseismic conversion at an interface. Results of these laboratory measurements were modeled using Haartsen's (1995) algorithm. Zhu and Toksöz (1996) simulated a VSP acquisition geometry. Zhu and Toksöz (1997) simulated borehole acquisition geometry and recorded electrical fields induced by borehole Stoneley waves. One of the important results of the their experiments was that a Stoneley wave induced stronger electrical fields in permeable sand than in a non-permeable slate. Most recently, Zhu and Toksöz (1997, 1998) recorded electro-

[6] Parkhomenko *et al.* (1975) made their measurements at the $80kHz$ frequency. Their result does not contradict the fact that at zero frequency the streaming potential coupling coefficient is independent of permeability. Pride's (1994) model predicts that at high frequencies the streaming potential coupling coefficient decreases if permeability increases.

magnetic waves generated by a Stoneley wave at an interface between two media and at an isolated fracture intersected by a borehole. The experiments made by Dr. Zhu are indeed elegant. Dr. Zhu has simulated under controlled conditions all the electroseismic phenomena that have been observed in the field or predicted numerically. Unfortunately, the experimental results of Dr. Zhu cannot be used for a quantitative analysis because the experiments were made for illustrative purposes and amplitudes were not properly recorded.

Electroseismic phenomena were the least investigated in field experiments. The main reason is the difficulty of recording seismic-wave-induced electrical fields in situ. A typical signal-to-noise ratio encountered in experiments with a sledgehammer is 1/200 (Mikhailov *et al.*, 1997). Several reports of recording electroseismic signals in the field have been published (Ivanov, 1939, 1940; Neyshtadt and Osipov, 1959; Martner and Sparks, 1959; Zablocki and Keller, 1961; Broding *et al.*, 1963; Parkhomenko and Gaskarov, 1971; Tome, 1975; Skokan and Chi, 1990; Thompson and Gist, 1993; Butler *et al.*, 1994, 1996; Wolfe *et al.*, 1996; Mikhailov *et al.*, 1997; Russel *et al.*, 1997). More than a half of these reports explained the origin of the measured electroseismic signals (Neyshtadt and Osipov, 1959; Martner and Sparks, 1959; Broding *et al.*, 1963; Thompson and Gist, 1993; Butler *et al.*, 1994, 1996; Wolfe *et al.*, 1996; Mikhailov *et al.*, 1997; Russel *et al.*, 1997). Thompson and Gist (1993) were the first to provide a theoretical model and an amplitude estimate for the electroseismic conversions that they recorded. Mikhailov, Haartsen and Toksöz (1997) were the first to record electroseismic signals, explain their origin and compare field data with results of full waveform numerical modeling. Mikhailov *et al.* (1997) correctly modeled the arrival times, polarities and amplitude-versus-offset dependence of the electroseismic signals recorded in the field. The modeling was performed using Haartsen's (1995) algorithm based on Pride's (1994) model.

Traditionally, electroseismic experiments have been made on the surface and

were aimed at recording electroseismic conversions at interfaces. Thompson (1990) patented a method for electroseismic prospecting by delineating interfaces at which electroseismic conversions take place. However, our experience with surface electroseismic measurements convinced us that the use of electroseismic conversions in geophysical exploration still faces some difficulties. The main reasons for our conclusion are the following:

1. Electroseismic signals are extremely weak and it is problematic to measure electroseismic conversions at interfaces that are deep. Thompson and Gist (1993) recorded signals from a depth of $300m$. In the rest of the field experiments referenced above, the depths to the interfaces were less than $15m$.

2. Pride's model incorporates a vast number of media parameters, including drained and undrained frame moduli, porosity, permeability, tortuosity of pore space, fluid conductivity, fluid salinity, etc. It is very problematic to constrain these parameters of the subsurface from the surface. Thus, any inversion of electroseismic data runs into a problem of non-uniqueness.

These considerations convinced us to investigate electroseismic phenomena in boreholes. Our primary goal was to develop a real field method for characterizing porous rocks in situ. As always happens, we were not the first to come up with this idea.

Almost 60 years ago, Ivanov (1940) suggested using borehole electroseismic measurements to characterize rock formations in situ. Various ideas of borehole electroseismic measurements have been patented since 1947 (Doll, 1947, 1949, 1951, 1957; Ivanov, 1961; Semmelink, 1971). However, none of these ideas have been implemented in reality. Parkhomenko and Gaskarov (1971) made the first and only borehole electroseismic measurements and reported higher amplitudes of electroseismic signals in limestones than in shales. However, Parkhomenko and Gaskarov (1971) did not de-

termine which seismic wave induced these electrical signals and did not clarify which parameters of the rock formation can be deduced from borehole electroseismic measurements. Haartsen (1995) simulated electroseismic surveys in VSP or reverse VSP geometries. However, Haartsen (1995) did not simulate any electroseismic phenomena generated by waves propagating in a borehole. In his VSP simulations Haartsen (1995) recorded electrical fields at points along a vertical line in the subsurface and did not simulate any waves propagating in a borehole.

1.4 Thesis outline and summary of results

In this thesis, borehole electroseismic phenomena are investigated experimentally and theoretically. The main emphasis of this thesis is to understand the electroseismic phenomena that are observed in the field.

In Chapter 2, we first explain how a Stoneley wave propagating along a borehole in a permeable formation induces an electrical field. Then, we describe a borehole electroseismic measurement technique and present results of field experiments in a borehole drilled through fractured granite and diorite at a site in Hamilton, Massachusetts. In the field data we identify the electrical fields induced by the Stoneley wave. Analysis of the normalized amplitudes of these electrical fields shows that they were induced by the Stoneley-wave-generated fluid flow in fractures. The normalized amplitudes of the Stoneley-wave-induced electrical fields correlate with the fracture density log in granite.

Further in Chapter 2, we present measurements of the Stoneley-wave-induced electrical fields in four boreholes drilled through sedimentary rocks (dolomite) at a site in Belvidere, Illinois. In dolomite, the normalized amplitudes of the Stoneley-wave-induced electrical fields correlate with the porosity of a formation around a

borehole. Also, the Stoneley-wave-induced electrical fields have anomalously high amplitudes at an isolated fracture that intersects two of the boreholes.

In Chapter 3, we develop a Biot-theory-based model for the Stoneley-wave-induced electrical fields. The amplitudes of the electrical fields predicted by the theoretical model agree with the amplitudes measured in the field. According to the theoretical model, the normalized amplitude of the Stoneley-wave-induced electrical field is proportional to the porosity of a formation around the borehole. This result is consistent with the results of borehole electroseismic measurements in dolomite. We use the theoretical model to derive a porosity log for the granite formation from the electroseismic field data collected at the Hamilton site.

Further, according to the theoretical model, the normalized amplitude of the Stoneley-wave-induced electrical field is inversely proportional to the pore space tortuosity of a formation around a borehole. We use this result to explain the anomalously high amplitudes of the Stoneley-wave-induced electrical fields measured at the isolated fracture in the dolomite. We attribute this high amplitude anomaly to the tortuosity of the fracture being lower than the tortuosity of the pore space in the vuggy dolomite. Finally, the theoretical model predicts that the amplitude-versus-frequency behavior of the Stoneley-wave-induced electrical field depends on the permeability of the formation. The field data presented in Chapter 2 do not allow us to test this theoretical result.

In Chapter 4, we investigate experimentally the amplitude-versus-frequency behavior of the electrical fields induced by Stoneley waves. We develop an experimental technique that allows logging-type measurements of the Stoneley-wave-induced electrical potentials. Using this technique, we make electroseismic measurements in the borehole drilled through fractured igneous rocks. In our experiments we record Stoneley-wave-induced electrical potential in the frequency range from $300Hz$ to $4000Hz$.

The normalized amplitude of the Stoneley-wave-induced electrical potential identifies a large fracture intersected by the borehole.

By combining the data described in Chapter 4 with the data described in Chapter 2, we obtain the amplitude-versus-frequency dependence of the Stoneley-wave-induced electrical potentials in the frequency interval from $100Hz$ to $4000Hz$. We compare this amplitude-versus-frequency dependence with the predictions of the theoretical model. From this comparison we find that the theoretical model predicts the correct magnitudes for the electrical potentials induced by the Stoneley wave. Also, the amplitude-versus-frequency dependence of the electroseismic signals recorded at the depth of the large fracture roughly follows the trend predicted by the theory. However, the general amplitude-versus-frequency dependence of the electroseismic signals recorded in the field is more complicated than the one predicted by the theory. This can be attributed to (a) imperfection of the measurement devices; (b) failure of the theoretical model to correctly describe the phenomenon observed in the field; or (c) presence of some other electroseismic phenomenon that we do not account for.

The main contributions of this thesis are:

1. This thesis develops a borehole electroseismic measurement technique and demonstrates that it works in the field. This technique can be used to make electroseismic logging measurements.

2. This thesis investigates an electrical field induced by a borehole Stoneley wave. This electroseismic phenomenon is explained, measured in the field and modeled theoretically.

3. This thesis derives from field data a parameter that describes local electroseismic coupling in a formation around a borehole. This parameter, the normalized amplitude of the Stoneley-wave-induced electrical field, is defined as the ratio of an

electrical field amplitude to a pressure amplitude in the Stoneley wave at a certain depth. This thesis demonstrates that the normalized amplitude of the Stoneley-wave-induced electrical field can be used to identify permeable fractures.

4. This thesis uses field electroseismic measurements to quantitatively characterize rock formations around a borehole. Using the theoretical model developed in this thesis, a porosity log for fractured granite is derived from electroseismic field data.

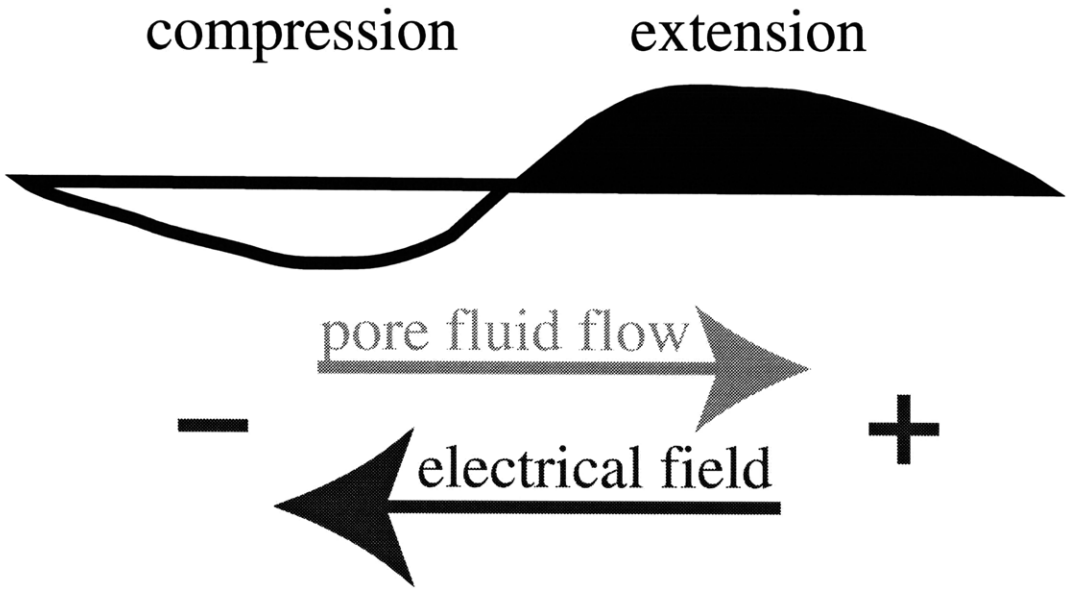

Figure 1-1: Diagram of a streaming electrical field induced by a compressional wave. A compressional wave propagating in a fluid-saturated porous rock creates a pressure gradient that drives the fluid flow from the zone of compression to the zone of extension. If the pore fluid carries an excess positive electrical charge, then the flow results in accumulation of a positive electrical charge in the zone of extension and a negative electrical charge in the zone of compression. This charge separation induces an electrical field that travels with the compressional wave.

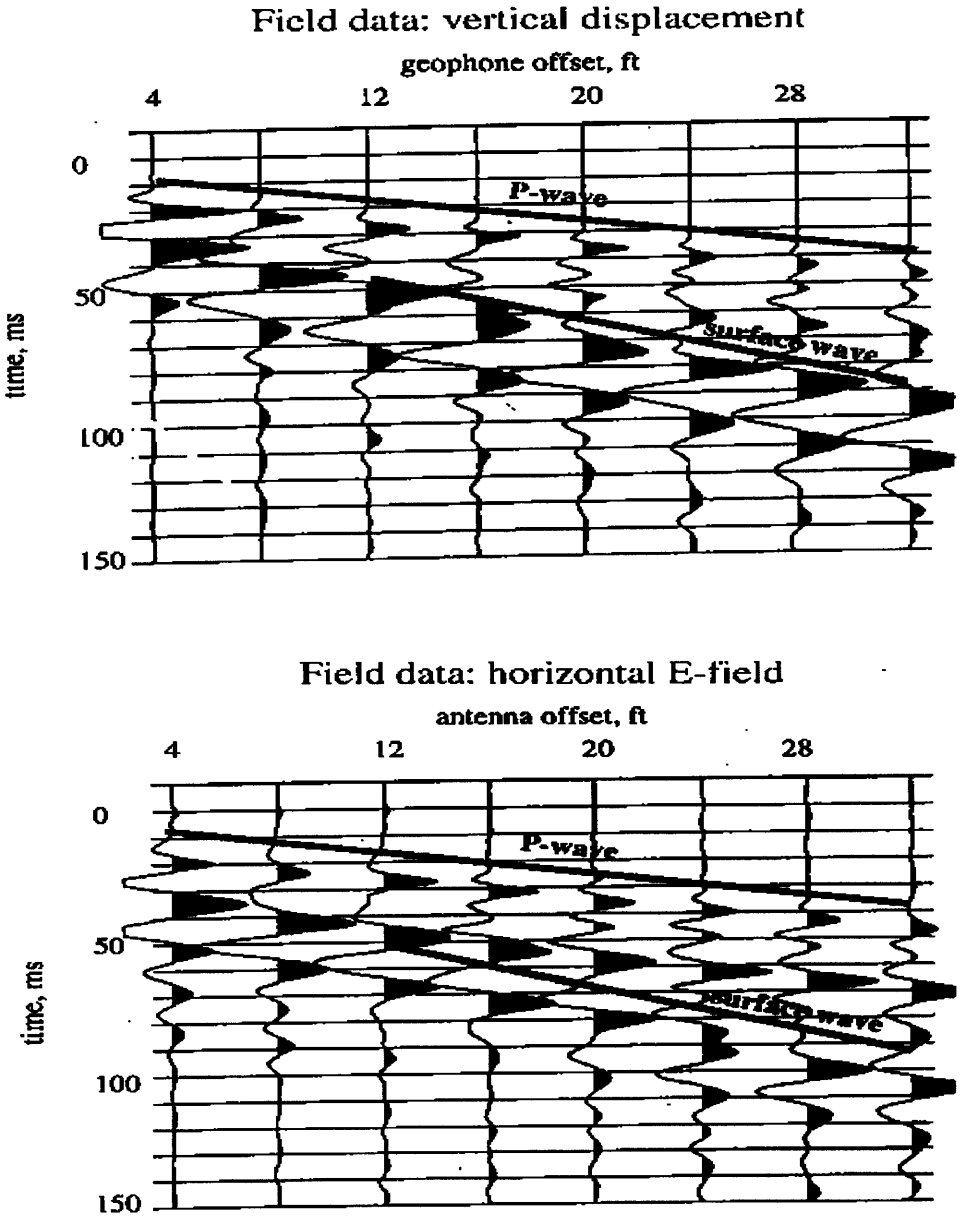

Figure 1-2: Measurements of vertical displacements and horizontal electrical fields at a site near Walden Pond, Massachusetts. The electrical data show that oscillations of the electrical field are induced by both the *P*-wave and the surface wave. The first motion of the *P*-wave is compressional and the "first motion" of the electrical field is negative. This result is consistent with the diagram in Figure 1-1.

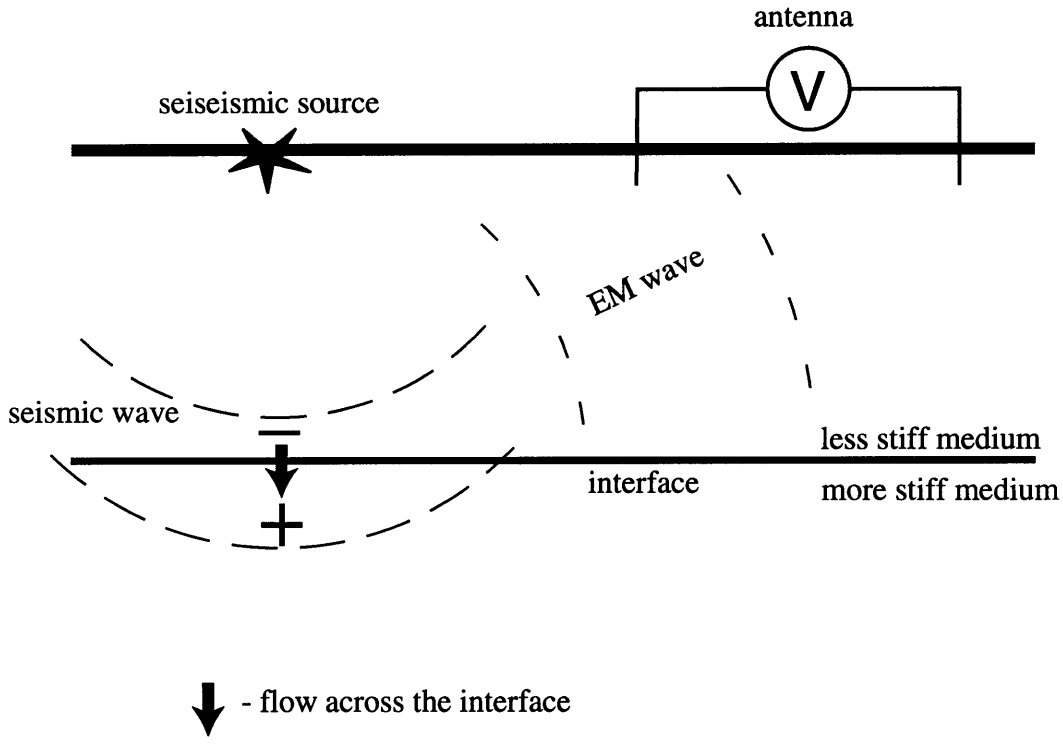

Figure 1-3: Diagram of an electromagnetic wave generated by a compressional wave crossing an interface between two media. If the medium above the interface has a soft frame and the medium below has a hard frame, then the compressional wave creates higher pore pressure in the medium above the interface than the pore pressure in the medium below. The difference in pore pressure across the interface causes pore fluid to flow from the medium above the interface to the medium below. This flow results in accumulation of a positive electrical charge below the interface and of a negative electrical charge above. This charge separation across the interface generates an electromagnetic wave that can be recorded on the surface.

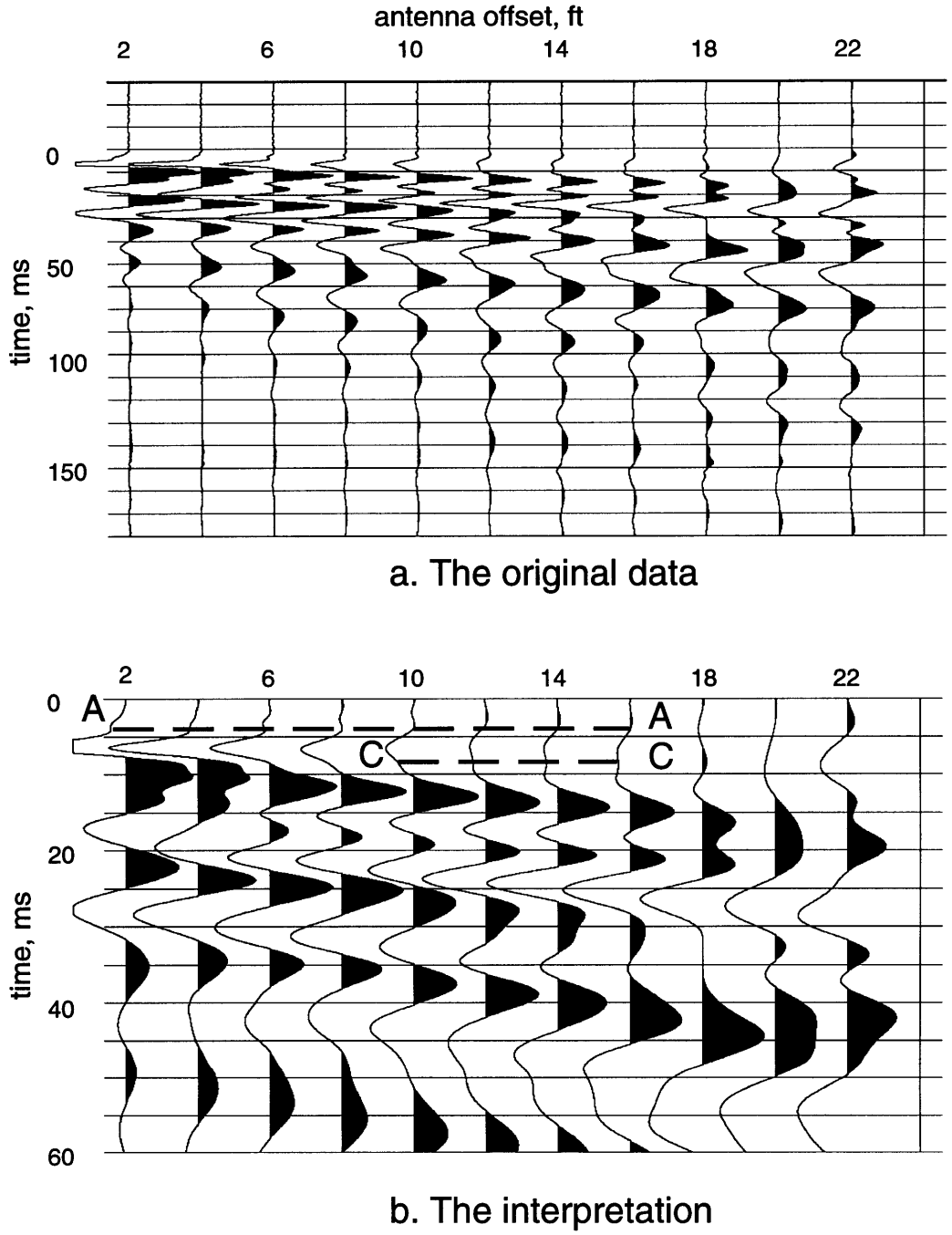

Figure 1-4: a) Electroseismic data collected at a site in Hamilton, Massachusetts. b) the first 60 ms of these data. Event A–A is the electroseismic conversion at the top soil–glacial till interface. Event C–C is, possibly, the electroseismic conversion at the watertable. Dashed lines mark the onset of these signals.

Chapter 2

Low-frequency measurements of electrical fields induced by borehole Stoneley waves

In this Chapter we describe an electroseismic phenomenon that is the primary focus of our investigation. This phenomenon is an electrical field induced by a borehole Stoneley wave. In permeable formations, this electrical field is induced by a Stoneley-wave-generated pore fluid flow.

This Chapter has two goals. The first goal is to demonstrate that this electroseismic phenomenon can be observed in the field. We describe a borehole electroseismic measurement technique and present results of field experiments in fractured igneous rocks and sedimentary rocks (dolomite). In the field data we identify the electrical fields induced by the Stoneley wave. From the analysis of their normalized amplitudes, we conclude that these electrical fields were induced by a pore fluid flow in the formation around a borehole.

The second goal of this Chapter is to investigate how this electroseismic phenomenon can be used for characterizing fluid transport properties of a formation around the borehole. From our field data we derive a parameter that describes local electroseismic coupling at each depth. This parameter is the normalized amplitude of the Stoneley-wave-induced electrical field. We demonstrate that in the experiment in fractured granite, this normalized amplitude correlates with the fracture density log. In the experiments in dolomite, the normalized amplitude of the Stoneley-wave-induced electrical fields correlates with the porosity of a formation around a borehole. Also, the Stoneley-wave-induced electrical fields have anomalously high amplitudes at an isolated fracture that intersects two boreholes.

2.1 Electroseismic phenomena caused by a borehole Stoneley wave

In this section we explain how a Stoneley wave induces an electrical field when propagating along a permeable formation. This electrical field moves along the borehole together with the Stoneley wave. When a Stoneley wave encounters an isolated fracture, it locally induces an electrical field and also generates an electromagnetic wave. This electromagnetic wave propagates in all directions with a velocity much higher than the velocities of seismic waves.

2.1.1 Electrical field induced by a Stoneley-wave-generated fluid flow in permeable formations

A seismic wave propagating in a fluid-saturated permeable rock induces an electrical field because the pore fluid saturating the rock carries an excess electrical charge. This

electrical charge is accumulated in the pore fluid because surfaces of most minerals adsorb ions of a certain polarity from the pore fluid, leaving an excess of ions of the opposite polarity in the fluid. This excess electrical charge is concentrated in a thin layer of pore fluid along the pore surfaces (Morgan *et al.*, 1989). For example, in quartz-bearing rocks filled with water, rock surfaces adsorb negative ions, leaving an excess positive electrical charge in water in the vicinity of rock surfaces. Whenever a pressure gradient, created by a seismic wave, forces the pore fluid to flow through the rock, the fluid displacement along the pore surfaces moves this excess electrical charge, thus creating a streaming electrical current. This streaming electrical current results in the induction of an electrical field.

Figure 2-1 is a diagram of an electrical field induced by a borehole Stoneley wave. A Stoneley wave propagating in a borehole creates a pressure gradient in a formation around the borehole. This pressure gradient drives the fluid flow from the zone of compression to the zone of extension. If the pore fluid carries a positive electrical charge (as in quartz-bearing rocks saturated with water), then the flow results in accumulation of a positive electrical charge in the zone of extension, and a negative electrical charge in the zone of compression. Thus, the Stoneley wave creates a capacitor-like electrical charge separation that moves along the borehole together with the wave. This charge separation induces an electrical field that also moves along the borehole together with the Stoneley wave.

We argue that the charge separation created by the Stoneley wave propagating along a homogeneous formation does not radiate electromagnetic waves. If the formation is homogeneous, then the charge separation and the electrical field created by the Stoneley wave do not change in magnitude as the wave propagates along the borehole. Thus, in a reference frame that moves along the borehole with the Stoneley wave velocity, the capacitor-like charge separation created by the Stoneley wave is stationary and constant. A stationary and constant charge separation does not radi-

ate electromagnetic waves (Duckworth, 1960). Overall, the electroseismic phenomena caused by a Stoneley wave in a homogeneous medium are similar to the electroseismic phenomena caused by a head wave. Numerical simulations (Haartsen, 1995) and field measurements (Mikhailov *et al.*, 1997) demonstrate that a head wave propagating along an interface between two homogeneous media creates an electrical field that moves together with the head wave, but does not radiate electromagnetic waves.

2.1.2 Electrical field and electromagnetic radiation generated by a Stoneley wave at an isolated fracture

When a Stoneley wave encounters an isolated fracture intersected by a borehole, it locally induces an electrical field and also generates an electromagnetic wave. Figure 2-2 is a diagram of these phenomena. A Stoneley wave creates an oscillating flow of fluid within the fracture. This flow carries a streaming electrical current that results in an oscillating charge separation within the fracture. The oscillating electrical charge induces an electrical field within and in the vicinity of the fracture. Also, this oscillating electrical charge radiates an electromagnetic wave that propagates in all directions with a velocity much higher than the velocities of seismic waves. Electromagnetic waves generated by Stoneley waves at isolated fractures are observed in laboratory experiments (Zhu and Toksöz, 1998) and in the field experiments described further in this Chapter.

Let's suppose that a homogeneous permeable formation consists of a system of fractures evenly distributed through the medium. In such a medium, the total electromagnetic radiation is a sum of electromagnetic waves generated at each fracture. Fractures in the compressional part of the Stoneley wave radiate electromagnetic waves out of phase with fractures in the extensional part of the Stoneley wave. If the fractures are evenly distributed, then at any point in space the electromagnetic

waves from all the fractures will cancel each other. Therefore, a Stoneley wave propagating along a homogeneously fractured formation does not radiate electromagnetic waves. This argument is consistent with the statement we made in the previous section that a Stoneley wave propagating in a homogeneous medium does not generate electromagnetic radiation.

In this section we described electroseismic phenomena that one can anticipate to encounter in the field. When propagating along a borehole in a permeable formation, a Stoneley wave will induce an electrical field. This electrical field will move along the borehole together with the Stoneley wave. Also, if the Stoneley wave encounters a large isolated fracture, then in addition to inducing an electrical field locally, the Stoneley wave will generate electromagnetic radiation. In order to determine whether these phenomena are indeed observable, we conducted field experiments.

2.2 Borehole electroseismic measurements in fractured igneous rocks

In this section we demonstrate that electroseismic phenomena caused by a Stoneley wave can be observed in a field experiment. We describe the measurement technique and present field data measured in a borehole at a site in Hamilton, Massachusetts. In the field data we identify two electroseismic phenomena. The first phenomenon is an electrical field induced by the Stoneley wave. This electrical field moves along the borehole together with the Stoneley wave. The second phenomenon is electromagnetic radiation generated by the Stoneley wave. The electromagnetic waves propagate in all directions with a velocity much higher than velocities of seismic waves.

2.2.1 Experimental site

We conducted our first borehole electroseismic experiments in a well that was drilled through fractured igneous rock at a site in Hamilton, Massachusetts. The upper $137m$ of the well is in granite, and below the depth of $137m$ is in diorite. Within the diorite section there are three zones of monzodiorite $5m$, $9m$ and $17m$ thick at depths of $137m$, $168m$ and $280m$, respectively. A $6m$ thick felsite dike intersects the well at the depth of $152m$ (GEOSS, 1984b).

Figure 2-3 presents the results of various geophysical measurements in the well demonstrating that both the granite and diorite sections of the well are highly fractured. The borehole video log showed small and large fractures intersecting the well throughout the entire $300m$ depth of investigation. The borehole video and the borehole televiewer logs demonstrate that most of the fractures are horizontal. The fracture density log derived from the borehole video shows that at some depths there are up to 10 fractures per meter. The borehole caliper log also shows numerous enlargements of the borehole wall at depths where a drill bit encountered fractures in the hard rock. The P-wave slowness log shows numerous kicks (off scale) corresponding to highly fractured zones. The conductivity log shows relatively high conductivity values for igneous rock, again corresponding to highly fractured granite and diorite.

Analysis of the cuttings from the well (GEOSS, 1984a,b) demonstrates that in the granite and the diorite the rock matrix has no porosity. Thus, all the porosity and permeability of the granite and the diorite formations are due to fractures. A pumping test in another well that is $12m$ away from the experimental well yielded a flow rate of $300gal/min$ ($1.9 \cdot 10^{-2} m^3/s$) that was sustained for 26 days (Haley and Aldrich, Inc., 1990). The main flow conduit identified by the pumping test was the fractured zone between the depths of $55m$ and $61m$. The pumping test demonstrated that there is a flow communication between the two wells through the horizontal fractures

in the subsurface. Therefore, we can conclude that the fractures intersecting the experimental well are permeable.

The experimental well was cased only through the top $10m$ of overburden, and was uncased in the granite and diorite. This allowed pressure communication between the borehole and the fractures. When the Stoneley wave propagated along the borehole, it induced a flow of fluid within the fractures. Thus, the borehole was suitable for electroseismic experiments.

2.2.2 Field experimental procedure

In the experiments we generated a Stoneley wave at the top of the well by vertically striking the casing with a sledge hammer. This Stoneley wave had a center frequency of $150Hz$ which corresponds to a wavelength of $9.3m$. We measured pressure oscillations created by the wave as it propagated in the borehole, using hydrophones suspended in the borehole fluid. We measured the electrical field induced by the Stoneley wave as a potential difference between two lead electrodes. The diagram of the electrical field measurements is given in Figure 2-4. In the experiment the electrodes were suspended in the borehole fluid and were connected to a data acquisition system at the surface by an unarmored cable. We would like to emphasize the simplicity of the measurement devices. They were nothing more than hydrophones and pairs of lead electrodes suspended in the borehole fluid.

To record the signals measured by the hydrophones or the electrode pairs we used a seismic data acquisition system (OYO Geospace model DAS-1) with a dynamic range of $120dB$ and a crosstalk between channels of less than $-100dB$. The sampling rate of the recording was $0.125ms$. During the experiments we recorded either 3 hydrophone traces or 4 electrical traces at a time. To collect measurements throughout the $280m$

section of the well at a $1m$ spacing between the traces we moved the hydrophone string or the electrode string along the well and repeated the source. In the electrical experiments we stacked the data 20 times at each depth and in the hydrophone experiments, 5 times at each depth.

2.2.3 Noise reduction in the electrical data

The electrical records made in the experiment contained electrical fields induced by the borehole Stoneley wave but also contained electrical fields induced by remote power lines and by telluric currents in the ground. The amplitude of the Stoneley-wave-induced electrical fields detected in the experiments was less than $25\mu V/m$, while the power line and telluric noise was about $2mV/m$, i.e., 80 times larger. In order to reduce this noise we used the two-step processing sequence summarized below. The specific details of our noise-reduction processing were described and illustrated in a paper by Mikhailov *et al.* (1997).

The first step in the noise-reduction processing was remote referencing. This technique is commonly used in field electroseismic measurements (Thompson and Gist, 1993; Butler *et al.*, 1996; Wolfe *et al.*, 1996; Mikhailov *et al.*, 1997). To reduce the noise in the electrical data, we used the observation that at the frequency of the Stoneley wave in the experiments ($150Hz$) the power line and telluric noise did not change phase throughout the depth of investigation, i.e., the noise was practically the same in the borehole and on the surface. In the field, while recording the electrical signals in the borehole, we simultaneously recorded the electrical noise on two mutually perpendicular electrical dipoles on the surface. During signal processing we subtracted the noise recorded on the surface from the measurements in the borehole. This reduced the noise by a factor up to 50.

To further reduce the noise induced by remote power lines, we used $60Hz$ harmonic subtraction (Butler and Russell, 1993). This step further reduced the noise by a factor up to 5. Overall, this noise-reduction processing improved the signal-to-noise ratio in the electrical records by a factor up to 250.

2.2.4 Full-waveform electroseismic data

Using the measurement technique and the noise-reduction processing described in the previous section, we were able to detect electroseismic phenomena caused by the Stoneley wave. Figures 2-5—2-7 present the hydrophone and electrical signals that were recorded in the field.

The pressure measurements in Figure 2-5 show the direct Stoneley wave propagating from the top of the well (Event A-A). Large fractures and enlargements of the borehole wall generate reflections of the Stoneley wave propagating upward. We would like to emphasize that our borehole was intersected by fractures throughout the entire depth of investigation (Figure 2-3). The distinct Stoneley wave reflections in Figure 2-5 are generated by the largest of them.

Figures 2-6 and 2-7 show the electrical signals recorded in two separate experiments made on different days with two different electrode separations. The electrical signals in Figure 2-6 were measured with a $0.5m$ separation between the electrodes, and signals in Figure 2-7 were measured with a $1.0m$ electrode separation. In the electrical data we identify three events.

1. The most visible event in the data is an electrical signal moving along the borehole at the Stoneley wave velocity (Event A-A). Comparison of the electrical data with the pressure data shows that this signal arrives at each depth simultaneously with the Stoneley wave. The electrical data shows that such an electrical field is generated

by both the direct and reflected Stoneley waves propagating in the borehole.

2. The electrical data in Figures 2-6 and 2-7 show an electrical signal arriving at zero time at all depths. This signal is an electromagnetic wave generated when a metal sledgehammer hits the metal casing. Similar signals were described by Butler et al. (1994) and Mikhailov et al. (1997).

3. The electrical data show weak electrical signals arriving simultaneously at all depths at the times of $60ms$ (Event C-C in Figure 2-6) and $40ms$ (Event B-B in Figure 2-7). The apparent zero moveout of these signals indicates that they propagate with a velocity much higher than the velocities of seismic waves. We suggest that Events B-B and C-C are electromagnetic waves generated when a Stoneley wave encounters large fractures at depths of $87m$ and $63m$, respectively. Such electromagnetic waves generated by a Stoneley wave at isolated fractures have been observed in laboratory experiments (Zhu and Toksöz, 1998). These electromagnetic waves are not the focus of this thesis because their amplitudes are barely above the noise level. We point them out to illustrate what kinds of electroseismic phenomena can be observed in the field.

Traditionally, electroseismic field experiments are aimed at recording electromagnetic waves generated by seismic waves at heterogeneities (Thompson and Gist, 1993; Butler *et al.*, 1996) and the electrical fields locally induced by seismic waves are neglected. This thesis is focussed on the electrical fields induced locally by the Stoneley wave (Event A-A). We argue that these electrical fields are caused by the Stoneley-wave-generated fluid flow in fractures. We also develop a theoretical model that relates the normalized amplitudes of these electrical fields to the porosity and permeability of the formation around the borehole.

2.3 Analysis of the Stoneley-wave-induced electrical fields in fractured igneous rocks

In this section we present evidence that the electrical field moving along the borehole together with the Stoneley wave (Event A-A in Figures 2-6 and 2-7) is caused by the Stoneley-wave-generated fluid flow in fractures. We demonstrate that the normalized amplitude of the Stoneley-wave-induced electrical field correlates with the fracture density log in granite.

2.3.1 Definition of the normalized amplitude of the Stoneley-wave-induced electrical fields

The conclusion that the electroseismic phenomena observed in the experiments are caused by the fluid flow within fractures is based on the analysis of the normalized amplitude of the Stoneley-wave-induced electrical field. We define the normalized amplitude of the Stoneley-wave-induced electrical field at a certain depth as a ratio of the amplitude of the electrical field oscillation at this depth to the amplitude of pressure oscillation at this depth. The normalized amplitude, defined in this way, characterizes the local electroseismic coupling. It is also independent of the pressure amplitude because it represents the electrical field induced at a certain depth by a unit pressure oscillation at this depth.

Figure 2-8 illustrates how we derived the normalized amplitude of the Stoneley-wave-induced electrical field from the field data. The first plot in Figure 2-8 is the rms amplitude of the pressure oscillation in the direct Stoneley wave (Event A-A in Figure 2-5). We calculated this amplitude for the main wavelet of the direct Stoneley wave. Figure 2-8 shows that as the Stoneley wave propagates down the borehole, its

amplitude decreases due to backscattering and attenuation.

The second plot in Figure 2-8 is the rms amplitude of the electrical potential difference recorded by electrode pairs with a $0.5m$ separation (Event A-A in Figure 2-6) and by electrode pairs with a $1.0m$ separation (Event A-A in Figure 2-7). Using the same procedure as for pressure, we calculated these amplitudes for the main wavelet of Event A-A. Figure 2-8 shows that, on average, the amplitude of the electrical signals decreases with depth because the amplitude of the pressure oscillations decreases as the Stoneley wave propagates down the borehole. Further, Figure 2-8 shows that at each depth the potential difference between electrodes separated by $1.0m$ was two times higher than the potential difference between electrodes separated by $0.5m$. This result is consistent with the fact that the wavelength of the electrical field oscillation is the same as the Stoneley wavelength (about $9.3m$ in the experiment). The distances between the electrodes in both cases are significantly less than the wavelength, and therefore the potential difference between the electrodes is proportional to the distance between them.

The third plot in Figure 2-8 is the normalized amplitude of the Stoneley-wave-electrical field. We calculated it for each depth by first obtaining the electrical field amplitude as the potential difference amplitude divided by the distance between the electrodes. Then, we divided the amplitude of the electrical field at each depth by the amplitude of the pressure oscillation at the same depth. Figure 2-8 shows the agreement between the normalized amplitudes of the Stoneley-wave-induced electrical fields measured in two different experiments using a $0.5m$ electrode separation (Event A-A in Figure 2-6) and a $1.0m$ electrode separation (Event A-A in Figure 2-7). This result demonstrates that the electroseismic phenomenon observed in the experiment is repeatable.

2.3.2 Analysis showing that the Stoneley-wave-induced electrical fields are caused by the fluid flow in fractures

We argue that the electrical fields measured in the experiments are caused by the Stoneley-wave-generated fluid flow in fractures. Our argument is based on the following analysis.

1. The electrical fields measured in the experiments were not generated by the action of the Stoneley wave on the electrodes. The analysis in Appendix A shows that the motion of the electrodes caused by the Stoneley wave could not generate the electrical signals with the amplitudes recorded in the experiments. Also, the analysis in Appendix A demonstrates that streaming potentials induced by the fluid motion along the surface of the electrodes also could not cause these signals.

2. The electrical fields measured in the experiments were generated within the rock formation. Figure 2-8 shows that the normalized amplitudes of the Stoneley-wave-induced electrical fields in the granite section (10-137m) is between $5nV/(m \cdot Pa)$ and $20nV/(m \cdot Pa)$. At the same time, in the diorite section (177-280m) the normalized amplitude is around $3nV/(m \cdot Pa)$. Thus, the amplitudes of the electroseismic signals are sensitive to the rock type. The analysis in Appendix A shows that the streaming potentials induced by the fluid motion along the borehole wall could not generate the electrical signals recorded in the experiments. Thus, the fact that the normalized amplitude of the electrical field is sensitive to the rock type together with the fact that these electrical fields cannot be generated on the surface of the borehole suggest that the electrical fields measured in the experiments were generated within the rock formation around the borehole.

3. The electrical fields measured in the experiments were not caused by the piezoelectric effect. The analysis of the cuttings from the borehole (GEOSS, 1984b)

shows that the granite does not have any prefered orientation of quartz or any other crystals. Random orientation of the mineral grains leads to a net zero piezoelectric constant. Moreover, the amplitude of the electroseismic signals varies by a factor of 4 within the granite section (10-137m), while the cuttings show no variation in the mineral composition or the orientation of crystals in the granite section.

4. The electrical fields measured in the experiments were generated within the fractured zones. Figure 2-9 shows a comparison between the fracture density log for the granite section of the well and the normalized amplitude of the Stoneley-wave-induced electrical fields. The first plot in Figure 2-9 is the fracture density (the number of fractures per meter) derived from the borehole video log. The second plot in Figure 2-9 is the fracture density log averaged over the Stoneley wavelength (9.3m in the experiment) using a cosine-shaped weighting function. The third plot in Figure 2-9 is the normalized amplitude of the Stoneley-wave-induced electrical field. Figure 2-9 shows that there is a good correlation between the averaged fracture density plot and the normalized amplitudes of the electrical fields. The more fractures there are around a certain depth, the higher the normalized amplitude of the Stoneley-wave-induced electrical field is. Therefore, we conclude that this electrical field was generated within the fractured zones.

We make the comparison between the fracture density log and the normalized amplitude of the Stoneley-wave-induced electrical fields in the granite section of the well because in this section the Stoneley-wave-induced electrical fields are very clear in the data (signal-to-noise ratio of up to 5). In the diorite section of the well these electrical fields are barely visible above the noise (Figures 2-6 and 2-7). The poor signal-to-noise ratio in diorite is due to (a) low amplitudes of the Stoneley wave in the diorite section (Figure 2-8) and (b) a lower streaming potential coupling in diorite than in granite. The difference between the streaming potential coupling in granite and in diorite will be discussed in the next Chapter of this thesis.

5. The normalized amplitudes of the electrical fields measured in the experiment agree with the predictions of the theoretical model for the electrical fields induced by the Stoneley-wave-generated pore fluid flow. This theoretical model and its comparison with the field data are presented in the next Chapter.

Overall, the correlation of the normalized amplitude with the fracture density log and the consistency of the experimental data with the theoretical model lead us to the conclusion that the electrical fields observed in the experiments were induced by the Stoneley-wave-generated fluid flow in fractures. We would like to emphasize that in the granite and the diorite at the Hamilton site, the rock matrix has no porosity (GEOSS, 1984a,b). Thus, all the porosity and permeability of the granite and the diorite formations are due to fractures.

2.3.3 Summary: using borehole electroseismic measurements to identify fractured zones

In this section we have presented measurements of the electrical fields induced by the borehole Stoneley wave in fractured igneous rocks. Analysis of these electrical fields showed that they were induced by fluid flow in fractures. Moreover, the normalized amplitude of the Stoneley-wave-induced electrical field correlates with the fracture density log for the granite section.

Based on these results we suggest using measurements of the Stoneley-wave-induced electrical fields to detect fractured zones in tight igneous rocks, where any significant permeability is associated with fractures. If electrodes placed at a certain depth in a borehole detect a streaming electrical field when a Stoneley wave propagates past them, then the formation at this depth is fractured. This conclusion can be made because the Stoneley wave induces a flow of the electrically charged pore fluid in the

formation at this depth. If the Stoneley wave does not induce an electrical field, then the formation at this depth is not fractured.

In the fractured granite at the Hamilton site, both porosity and permeability are due to fractures. Thus, the correlation of the normalized amplitude of the Stoneley-wave-induced electrical field with the fracture density log does not allow us to conclude whether this normalized amplitude is sensitive to porosity or permeability of a formation around a borehole. Thus, it was necessary to conduct more field experiments in order to investigate the sensitivity of electroseismic phenomena to these formation properties.

2.4 Borehole electroseismic measurements in dolomite: general description of the experimental site

We conducted field experiments in four boreholes drilled through shaly dolomite at a site in Belvidere, Illinois. In these boreholes (labeled T1, T2, T6 and T7), a number of logging measurements were made in order to characterize the subsurface properties (Paillet, 1997; Paillet *et al.*, 1998). Below, we summarize all the available information about the site that we will later use to interpret the results of borehole electroseismic measurements. The boreholes will be analyzed in the following order: T6, T7, T2 and T1. The reason why we chose this order will become evident when we interpret the electroseismic data.

2.4.1 Permeable zones in the subsurface and estimates of their hydraulic transmissivity

Figure 2-10 (from Paillet (1997)) presents a vertical cross-section of the subsurface at the site. It shows four major permeable zones that were identified by borehole flowmeter measurements and cross-borehole pumping tests. The first zone (labeled *a* in Figure 2-10) is a bedding plane fracture intersecting boreholes T6 and T7 at the depth of $12m$. The second zone (labeled *b*) is a near vertical fracture intersecting boreholes T1 and T2 around the depth of $25m$. The width of the intersection is $3.1m$ in borehole T1 and $1.7m$ in borehole T2. The third permeable zone (labeled *c*) is a porous layer intersecting all the boreholes between the depths of $27.5m$ and $30.5m$. The fourth permeable zone (labeled *d*) is also a porous layer intersecting all the boreholes between the depths of $42.5m$ and $55m$ (Paillet, 1997).

Paillet *et al.* (1998) used wireline packer measurements in boreholes T1 and T6 to estimate relative hydraulic transmissivity of the dolomite in various depth intervals. Hydraulic transmissivity of a certain depth interval is defined as a product of the thickness of the interval to its hydraulic conductivity (Davis and DeWeist, 1966). In turn, hydraulic conductivity of a formation is defined as a ratio of water flow through a formation to the applied pressure gradient. Thus, hydraulic transmissivity is proportional to the permeability and the thickness of a depth interval (Davis and DeWeist, 1966).

Wireline packer measurements can be used to deduce only relative and not absolute values of hydraulic transmissivity (Paillet *et al.*, 1998). Paillet *et al.* (1998) defined the relative hydraulic transmissivity of a certain depth interval as a ratio of the hydraulic transmissivity of this interval to the hydraulic transmissivity of a "reference" interval. The values of the relative hydraulic transmissivity in boreholes T6 and T1 are presented in Figures 2-23 and 2-29, respectively. Paillet *et al.* (1998)

estimated relative hydraulic transmissivity in intervals of approximately the same thickness. Thus, the plots of relative hydraulic transmissivity versus depth in Figures 2-23 and 2-29 reflect the variation of averaged permeability with depth in boreholes T6 and T1.

2.4.2 Porosity measurements

To measure porosity of the dolomite, sonic and neutron logs were run in boreholes T6 and T1. Both sonic and neutron logs are indicators of porosity of a formation around a borehole. Figure 2-11 presents the porosity logs deduced from sonic and neutron logs in boreholes T6 and T1. To deduce the dolomite porosity from the sonic log, we used the Wyllie equation (Hilchie, 1978):

$$\phi = \frac{\frac{1}{V_p} - \frac{1}{V_0}}{\frac{1}{V_f} - \frac{1}{V_0}}. \tag{2.1}$$

Here, $\frac{1}{V_p}$ is the P-wave slowness of the formation, $\frac{1}{V_0} = 43.5\frac{\mu s}{ft} = 142.7\frac{\mu s}{m}$ is the P-wave slowness of dolomite with zero porosity, and $\frac{1}{V_f} = 206\frac{\mu s}{ft} = 675\frac{\mu s}{m} = 1/(1480\frac{m}{s})$ is the P-wave slowness in pure water. The resulting sonic porosity logs are plotted in Figure 2-11 with dashed lines.

The neutron logging tool used in boreholes T6 and T1 was calibrated for limestone in an $8in$ borehole, according to the standard of the American Petroleum Institute. Thus, the original neutron log data represented the "apparent limestone porosity". To recalibrate this data into dolomite porosity, we subtracted a constant value from the "apparent limestone porosity" values. This constant shift accounted for the dolomite correction of -7% (Schlumberger, 1972) and the borehole radius correction. We chose this constant shift so that the neutron porosity logs matched the sonic porosity logs. The resulting neutron porosity logs for dolomite are plotted in Figure 2-11 with solid lines.

In borehole T1, the neutron and the sonic porosity logs have the same values and the same variation with depth. This match demonstrates that the procedure that we used to deduce porosity from the sonic and the neutron logs is correct. In borehole T6, the neutron and the sonic porosity logs agree below the depth of $25m$. Above the depth of $25m$, the sonic log deviates towards higher porosity values but has the same variation with depth as the neutron porosity log. This deviation can be interpreted in two ways: (1) above the depth of $25m$ the "zero porosity" slowness is higher than that of dolomite or (2) above the depth of $25m$ the lithological correction for the neutron log is lower than that for dolomite. In either case, this mismatch between the neutron porosity and the sonic porosity logs indicates that at the depth of $25m$ the lithological composition of the formation changes (Hilchie, 1978). One of the possible interpretations of this lithological change that is consistent with all other logs is the presence of chert in dolomite above the depth of $25m$ (Paillet, private communication). However, based on the data that is available, the lithological composition cannot be determined uniquely.

2.4.3 Borehole televiewer images of a fracture and vugs in dolomite

Borehole televiewer logs were run in all boreholes. A borehole televiewer is an acoustic device for imaging a borehole wall. Borehole televiewer images can be used to identify fractures intersecting a borehole and to estimate their strike and dip. Charts made from borehole televiewer images show fracture intersection with boreholes T2 (Figure 2-28) and T1 (Figure 2-30) at the depth of $25m$.

Borehole televiewer images show all irregularities of a borehole wall, including washout zones and caverns. In all the boreholes at the Belvidere site, the borehole televiewer images show numerous vugs that constitute a significant portion of the

dolomite's porosity. At some depths there are so many vugs that the formation resembles Swiss cheese. Figure 2-12 shows a section of a borehole televiewer image in borehole T1. This image is of the depth interval from $27.5m$ ($90ft$) to $33.5m$ ($110ft$). Black areas in the televiewer image are vugs in the dolomite. The presence of vugs in the dolomite is also evident in caliper logs. For example, the caliper log in borehole T7 (Figure 2-14) is highly irregular. This irregularity is due to the vugs intersected by the borehole wall.

While contributing to porosity, the vugs do not necessarily contribute to permeability. Comparison of the porosity logs and the relative hydraulic conductivity estimates in boreholes T6 (Figure 2-23) and T1 (Figure 2-29) show that porosity logs do not correlate with the relative hydraulic transmissivity and, therefore, with permeability.

2.4.4 Gamma, resistivity and SP measurements

Figure 2-13 present the gamma, the resistivity, the Self-Potential and the porosity logs in borehole T6. The gamma log is, in general, an indicator of the shale content in the formation (Schlumberger, 1972; Hilchie, 1978). The gamma log has several peaks (e.g., around the depths of $25m$, $37m$ and $44m$). These peaks indicate shale layers (Hilchie, 1978). Figure 2-13 also demonstrates that the values of the gamma logs are higher in the interval from $22m$ to $52m$ than in the intervals from $14m$ to $22m$ and from $52m$ and $58m$. This result suggests that between the depths of $22m$ and $52m$ the shale content in dolomite is higher than at other depths.

The resistivity log in borehole T6 is almost uniform below the depth of $23m$. It has only a minor decrease at the depth of $37m$ where the gamma log indicates a shale layer. Above the depth of $23m$ the resistivity log has a sharp increase by a factor of 3.

The resistivity log in borehole T7 (plotted with a dashed line in Figure 2-13) does not have this high resistivity anomaly above the depth of $23m$. The same high resistivity anomaly was detected in borehole T1 (Figure 2-16) and was not detected in borehole T2 (Figure 2-15). Below we describe a possible interpretation of this anomaly that was suggested by Paillet (private communication).

Boreholes T6 and T1 were logged in spring right after snow had melted. Boreholes T7 and T2 were logged several months later. Thus, the high resistivity anomaly above the depth of $23m$ in boreholes T6 and T1 is interpreted to be due to the infiltration of fresh water from melted snow into the dolomite formation. The sharp boundary of the resistivity anomaly means that the infiltration was interrupted by an impermeable layer (possibly a shale streak). This interpretation is supported by the SP log in borehole T6 (Figure 2-13). The SP curve changes abruptly by $-50mV$ at the depth of $21m$ [1]. This change is consistent with a situation when there is fresh water above $21m$, salty water below $21m$ and a semi-permeable shale membrane in between (Schlumberger, 1972). Note that the SP log in borehole T7 (Figure 2-14) does not have such an anomaly.

We made borehole electroseismic measurements in October. Therefore, we expect that at the time of the experiments, resistivity of the dolomite formation around boreholes T6 and T1 was similar to the resistivity of the dolomite around boreholes T7 and T2, i.e., almost uniform. We also expect that during our measurements there were no significant SP anomalies in all the boreholes, as is the case in borehole T7 (Figure 2-14).

[1] The mismatch between the depths of the resistivity and SP anomalies can be attributed to the mismatch of the "zero depth" points in the two logs.

2.4.5 Correlation of the formation properties between different boreholes

Boreholes T6 and T7 were drilled $2.7m$ away from each other. Comparison of Figures 2-13 and 2-14 demonstrates that the gamma logs in T6 and T7 agree throughout the entire depth of the boreholes. The resistivity logs in T6 and T7 agree below the depth of $23m$. As we mentioned earlier, the high resistivity anomaly above the depth of $23m$ in borehole T6 was due to the infiltration of fresh water into the dolomite formation right after snow had melted. Overall, comparison of the logs in T6 and T7 shows that the formation properties around these two boreholes are similar.

Boreholes T2 and T1 were drilled $2m$ away from each other. We do not have digital log data to make a comparison between these two boreholes [2]. Figures 2-15 and 2-16 are copied from the paper by Paillet (1997). Comparison of the logs in these Figures demonstrates that the formation properties around boreholes T2 and T1 are similar. The only difference is the high resistivity anomaly above the depth of $23m$ in borehole T1.

Boreholes T6 and T1 were drilled $16.8m$ away from each other. Figure 2-17 presents a comparison of neutron porosity and P-wave slowness logs in boreholes T6 and T1. Figure 2-17 demonstrates that the neutron porosity logs in boreholes T6 and T1 match in the depth interval from $16m$ to $60m$ [3]. The P-wave slowness logs in boreholes T6 and T1 correlate in the depth interval from $25m$ to $60m$. Above the depth of $25m$ there is a significant mismatch between these two logs. We suggest that this mismatch is due to the change of lithological composition in the formation around borehole T6 at depths above $25m$. Overall, agreement of various logs in all four boreholes suggests that the formation properties around all four boreholes are

[2]The data was accidentally erased at USGS (Paillet, private communication).
[3]The bottom of the casing in T6 was at the depth of $15.5m$.

similar below the depth of $25m$.

2.5 Borehole electroseismic measurements in dolomite: data and its interpretation

2.5.1 Field experimental procedure

We used exactly the same procedure as in the Hamilton experiment to make borehole electroseismic measurements in boreholes T6, T7, T2 and T1. In these boreholes we made electrical measurements with a $0.5m$ spacing between the electrodes (Figure 2-4). In each borehole, pressure and electrical signals were recorded every half meter over a depth interval from the bottom of the casing down to the depth of $58.8m$.

One of the challenges in the Belvidere experiment was that the site was in the middle of a power line grid. Nevertheless, the noise-reduction processing worked, and clear electroseismic signals were recorded.

2.5.2 Full-waveform electroseismic data

Field data demonstrates that electrical fields induced by borehole Stoneley waves can be measured in dolomite. Figure 2-18a shows hydrophone measurements of a direct Stoneley wave in borehole T1. Figure 2-18b shows results of electrical measurements in borehole T1. Two events are present in the electrical data. The first is an electromagnetic wave generated at time zero by striking the metal casing with a metal sledgehammer. This wave propagates with a velocity much higher than the velocities of seismic waves and, therefore, arrives "simultaneously" at all depths at time zero.

The second event in the electrical data is an oscillating electrical field that moves along the borehole together with the Stoneley wave. This Stoneley-wave-induced electrical field was described and analyzed earlier in this Chapter.

To characterize local electroseismic coupling at each depth, we derived the normalized amplitudes of the Stoneley-wave-induced electrical fields from full-waveform data in each borehole. The definition of the normalized amplitude and the method of its calculation were described earlier in this Chapter. Figures 2-19, 2-20, 2-21, and 2-22 present amplitudes of pressure and electrical signals measured in boreholes T6, T7, T2 and T1, respectively. Each Figure contains plots of the amplitudes of pressure and electrical potential oscillations generated by the Stoneley wave and plots of the normalized amplitudes of the Stoneley-wave-induced electrical fields.

Figures 2-19 to 2-22 demonstrate that in all four boreholes the normalized amplitudes of Stoneley-wave-induced electrical fields vary significantly with depth. In the following sections we demonstrate that the normalized electroseismic amplitude correlates with the porosity of the formation around the borehole. This result further supports the argument that the electrical fields that we measure in field experiments are induced by the Stoneley-wave-generated fluid flow in a formation around a borehole.

We analyze the experimental results in boreholes in the following order: T6, T7, T2 and T1. We chose this order because it corresponds to the increasing complexity in the interpretation of the results.

2.5.3 Borehole T6

Figure 2-23 presents the neutron porosity log, the normalized amplitude of the Stoneley-wave-induced electrical fields and the relative hydraulic transmissivity mea-

surements in borehole T6. Figure 2-23 demonstrates that the porosity log does not correlate with the relative hydraulic transmissivity. The high value of the relative hydraulic transmissivity around the depth of $12m$ is due to a highly permeable bedding plane fracture. The neutron porosity log does not have any anomaly at that depth (the jump off scale is due to the casing). Further, the dolomite porosity around the depth of $30m$ is lower than around the depth of $50m$. At the same time, the relative hydraulic transmissivity around the depth of $30m$ is higher than around the depth of $50m$. As we mentioned before, the lack of correlation between porosity and relative hydraulic transmissivity is due to vuggy porosity of the dolomite formation.

We were not able to make borehole electroseismic measurements at the depth of the bedding plane fracture because it was too close to the casing. An electromagnetic wave generated at the time of the hammer impact on the metal casing totally obscured the electroseismic signal. In Figure 2-23, we compare the normalized electroseismic amplitudes to porosity and relative hydraulic transmissivity below the depth of $14m$. The first conclusion that can be made from Figure 2-23 is that below the depth of $14m$ the normalized electroseismic amplitude does not correlate with the relative hydraulic transmissivity of the dolomite formation. For example, the normalized electroseismic amplitude around the depth of $50m$ is slightly higher than around the depth of $30m$. At the same time, the relative hydraulic transmissivity around the depth of $50m$ is 5 times lower than around the depth of $30m$. Further, Figure 2-29 suggests that the normalized electroseismic amplitude and the neutron porosity log have similar variations with depth.

Figure 2-24 shows a direct comparison between the normalized amplitude of the Stoneley-wave-induced electrical field (the thin solid line), the neutron porosity log (the thick solid line) and the sonic porosity log (thin dashed line). We can plot all three curves on the same scale because, by mere coincidence, the values of the normalized electroseismic amplitude in $\frac{nV}{m \cdot Pa}$ match the values of porosity in percent.

Figure 2-24 demonstrates that the normalized electroseismic amplitude closely matches the neutron porosity log in the depth intervals from $27m$ to $44m$ and from $47m$ to $60m$. Figure 2-25 is a cross-plot of the porosity and the normalized electroseismic amplitude in the depth intervals from $27m$ to $44m$ and from $47m$ to $60m$. The solid line in Figure 2-25 is the best linear fit to the data. This line is fairly close to the diagonal (dashed line). The average deviation from the linear trend (dashed line) is $1.96\frac{nV}{m \cdot Pa}$. The correlation coefficient between the porosity and the normalized electroseismic amplitude in the depth intervals from $27m$ to $44m$ and from $47m$ to $60m$ is 0.69. For comparison, the correlation coefficient between the neutron porosity log and the sonic porosity log in the same depth interval is 0.74. Thus, we can conclude that the correlation between the normalized electroseismic amplitude and porosity is reasonable.

Figure 2-24 also demonstrates that the curves of the normalized electroseismic amplitude and the neutron porosity have significant mismatches above the depth of $27m$ and around the depth of $45m$. Based on the data available, we cannot explain the mismatch around the depth of $45m$. However, the mismatch between the normalized electroseismic amplitude and the neutron porosity log above the depth of $27m$ can be attributed to a change in lithological composition of the formation. Figure 2-24 demonstrates that above the depth of $27m$ the sonic porosity log deviates from the neutron porosity log towards higher values. At the same time, the normalized electroseismic amplitude deviates from the neutron porosity log towards lower values. One of the possible interpretations of these data is that the rock matrix is softer and the electroseismic coupling is lower in the formation above the depth of $27m$ than below.

Overall, the experimental results in borehole T6 suggest that the normalized amplitude of the Stoneley-wave-induced electrical field correlates with the porosity of the formation around the borehole. Also, this experiment demonstrates that the nor-

malized electroseismic amplitude is sensitive to the lithological composition of the formation.

2.5.4 Borehole T7

As we mentioned before, boreholes T6 and T7 are only $2.7m$ apart and the formation properties around them are similar. Thus, results of the experiments in boreholes T6 and T7 can be used to test the repeatability of borehole electroseismic measurements.

Figure 2-26 presents a comparison between the normalized amplitudes of the Stoneley-wave-induced electrical fields measured in boreholes T6 and T7. Figure 2-26 demonstrates that the normalized electroseismic amplitudes in boreholes T6 and T7 agree in values and have similar variation with depth. Figure 2-27 is a cross-plot of the normalized electroseismic amplitude values in boreholes T6 and T7. The solid line is the best linear fit to the data. The average deviation from the linear trend is $2.7\frac{nV}{m \cdot Pa}$. The correlation coefficient between the E/P-versus-depth curves in boreholes T6 and T7 is 0.66. For comparison, the correlation coefficient between the gamma logs in boreholes T6 and T7 is 0.63. Thus, we can conclude that there is a reasonable agreement between the normalized electroseismic amplitudes in boreholes T6 and T7.

Figure 2-26 also presents a comparison between the normalized electroseismic amplitude in borehole T7 and the neutron porosity log in borehole T6 [4]. Figure 2-26 demonstrates that below the depth of $27m$ the the normalized electroseismic amplitude in borehole T7 correlates with the porosity of the dolomite formation. Further, Figure 2-26 demonstrates that, similarly to borehole T6, the normalized electroseismic amplitude in borehole T7 deviates from the porosity log towards lower values

[4]Boreholes T6 and T7 are $2.7m$ apart. All the properties of the dolomite formation around them are similar (Figures 2-13 and 2-14). Therefore, the porosity logs in boreholes T6 and T7 should be similar.

above the depth of $25m$. Also there is a similar mismatch at the depth of $45m$. Thus, the mismatches between the neutron porosity log and the normalized electroseismic amplitude in boreholes T6 and T7 are due to changes of formation properties and not due to errors of the measurements.

Overall, the results of the electroseismic measurements in borehole T7 further support the argument that the normalized amplitude of the Stoneley-wave-induced electrical field correlates with the porosity of a formation around a borehole. Moreover, the agreement between the electroseismic measurements in boreholes T6 and T7 demonstrates the repeatability of the experimental results.

2.5.5 Borehole T2

In boreholes T2, T6 and T7, all the formation properties are similar below the depth of $25m$. Thus, the results of the electroseismic measurements in borehole T2 should be similar to the results in boreholes T6 and T7. Below we present the actual measurements in borehole T2.

Figure 2-28 presents a comparison between the normalized amplitude of the Stoneley-wave-induced electrical field in borehole T2 and the neutron porosity log in borehole T1 [5]. Figure 2-28 demonstrates that at the depth of $25m$, the Stoneley-wave-induced electrical field has an anomalously high amplitude of $30\frac{nV}{m \cdot Pa}$. This value is almost 3 times higher than the averaged values in boreholes T6 and T7. Comparison of the normalized electroseismic amplitude with the borehole televiewer image in borehole T2 shows that this high amplitude anomaly is at the depth of the isolated fracture. This result supports our earlier conclusion that borehole electroseismic

[5] Boreholes T2 and T1 are $2m$ apart. All the properties of the dolomite formation around them are similar (Figures 2-15 and 2-16). Therefore, the porosity logs in boreholes T2 and T1 should be similar.

measurements can be used to identify fractures.

Above the depth of $23m$ and below the depth of $30m$, the normalized electroseismic amplitude correlates with the neutron porosity log. Figure 2-28 shows that there are two main discrepancies between the normalized electroseismic amplitude and the neutron porosity log. The first mismatch is at the depth of $42m$. Based on the data available, we cannot explain this mismatch. The second mismatch is at the depth of $50m$. At this depth there is a 5% discrepancy between the sonic and the neutron porosity logs in borehole T1 (Figure 2-11). In the same way as in borehole T6, this discrepancy indicates a change of lithological composition at this depth. Thus, the mismatch at the depth of $50m$ can be attributed to a change in lithological composition of the formation.

Overall, the experiment in borehole T2 demonstrate that the Stoneley-wave-induced electrical fields have amplitudes that are 3 times higher at the isolated fracture than in the rest of borehole T2 or in boreholes T6 and T7. Also, in the rest of borehole T2, the normalized electroseismic amplitude correlated with the neutron porosity log. The two major discrepancies between the normalized electroseismic amplitude and porosity can be attributed to changes in the lithological composition of the formation.

2.5.6 Borehole T1

Results of the electroseismic measurements in borehole T1 are the most difficult to interpret. In our interpretation we will rely on the results of the electroseismic measurements in boreholes T6, T7 and T2.

Figure 2-29 presents a comparison between the normalized amplitude of the Stoneley-wave-induced electrical fields, the neutron porosity log and the relative hydraulic conductivity estimates in borehole T1. Figure 2-29 suggests that there is no cor-

relation between the normalized electroseismic amplitude and the relative hydraulic transmissivity. For example, the normalized electroseismic amplitude is higher around the depth of $30m$ than around the depth of $25m$. At the same time, the relative hydraulic amplitude is lower around the depth of $30m$ than around the depth of $25m$. Further, Figure 2-29 suggests that there is a similarity between the general trends of the normalized electroseismic amplitude and the neutron porosity log.

Figure 2-30 shows a direct comparison between the normalized electroseismic amplitude and the neutron porosity log in borehole T1. Figure 2-30 shows that below the depth of $41m$ and above the depth of $23m$ the values of the normalized electroseismic amplitudes in $\frac{nV}{m \cdot Pa}$ roughly agree with the values of the porosity log in percent. This result is consistent with the results of electroseismic measurements in boreholes T6, T7 and T2. However, there are several significant mismatches between the two curves. Similarly to the interpretation of such mismatches in the other boreholes, we suggest that some of them are due to changes in lithological composition of the formation.

Figure 2-30 shows that the Stoneley-wave-induced electrical fields have anomalously high amplitudes around the depth of $25m$. At this depth, the caliper log and the borehole televiewer log identify a near vertical fracture. These anomalously high amplitudes at the fracture are similar to the ones observed in borehole T2. Figure 2-30 also shows that the Stoneley-wave-induced electrical fields have anomalously high amplitudes between the depths of $28m$ and $37m$. This anomaly is not observed in borehole T2.

Figure 2-31 presents a comparison between the normalized electroseismic amplitudes measured in boreholes T1 and T2. Figure 2-31 demonstrates that the normalized electroseismic amplitudes in boreholes T1 and T2 agree below the depth of $40m$ and above the depth of $23m$. Also, the normalized electroseismic amplitudes agree

at the depth of the isolated fracture. Thus, Figure 2-31 demonstrates that the measurements in boreholes T1 and T2 are consistent everywhere except for the interval between the depths of $28m$ and $37m$ and around the depth of $40m$.

We do not have any data that can explain the anomalously high electroseismic amplitudes between the depths of $28m$ and $37m$. We can only present a hypothesis that is based on our intuition. In borehole T2 the borehole televiewer image demonstrates that the lengths of an intersection between the fracture and borehole is $1.7m$. In borehole T1, the length of the intersection is $3.1m$ (Paillet, 1997). Therefore, the fracture turns closer to vertical in the vicinity of borehole T1. If the fracture has the same dip below its intersection with borehole T1, then at the depth of $37m$ it is only $55cm$ away from the borehole and is even closer above $37m$. It is possible that the Stoneley-wave-generated pressure around the borehole induces fluid flow in the fracture even below its intersection with the borehole. In turn, this flow in the fracture induces an electrical field that is measured in the borehole.

Overall, despite the complexity of interpretation, the experimental results in borehole T1 demonstrated that the Stoneley-wave-induced electrical fields have anomalously high amplitudes at the depth of the isolated fracture. Also, at depths above $28m$ and below $37m$ the normalized electroseismic amplitudes in boreholes T1 and T2 are consistent.

2.5.7 Summary of the results of the dolomite experiment

Results of the electroseismic measurements in dolomite demonstrated that the normalized amplitude of the Stoneley-wave-induced electrical field correlates with the porosity of a formation around the borehole. The best correlation was obtained in boreholes T6 and T7.

Further, in borehole T2 and T1 the Stoneley-wave-induced electrical fields have anomalously high amplitudes at the depth of the isolated fracture. This result supports our earlier suggestion that borehole electroseismic measurements can be used to identify fractures.

In all four boreholes at the Belvidere site there were significant mismatches between the porosity log and the normalized electroseismic amplitude. In some cases, these mismatches corresponded to clearly identified changes of the lithological composition. In other cases, we could not explain the mismatches between the porosity and the normalized electroseismic amplitude based on the data that is available. This is not surprising because interpretation of even conventional logging measurements requires experience and often is not straightforward.

2.6 Conclusions

In this Chapter we described a new electroseismic phenomenon, the Stoneley-wave-induced electrical fields. We developed an experimental procedure and a noise-reduction processing that allows measurements of this electroseismic phenomenon. Using this procedure, we made borehole electroseismic measurements in fractured igneous rocks and in sedimentary rocks (dolomite). In the full-waveform electroseismic data we identified the Stoneley-wave-induced electrical fields. Analysis of the normalized amplitudes of these electrical fields shows that they were induced by the Stoneley-wave-generated fluid flow in a formation around a borehole.

From the field data we derive a parameter that describes local electroseismic coupling at each depth. This parameter is the normalized amplitude of the Stoneley-wave-induced electrical field. We defined this normalized amplitude as a ratio of the amplitude of the electrical field oscillation at a certain depth to the amplitude of the

pressure oscillation at this depth. Analysis of the experimental results demonstrated that:

1. In granite, the normalized amplitudes of Stoneley-wave-induced electrical fields correlate with the fracture density log.

2. In dolomite, the normalized amplitudes of the Stoneley-wave-induced electrical fields correlate with the porosity of the formation.

3. In dolomite, the Stoneley-wave-induced electrical fields have anomalously high amplitudes at the isolated fracture that intersects boreholes T1 and T2.

4. In all experiments, the normalized amplitudes of the Stoneley-wave-induced electrical fields are sensitive to lithology.

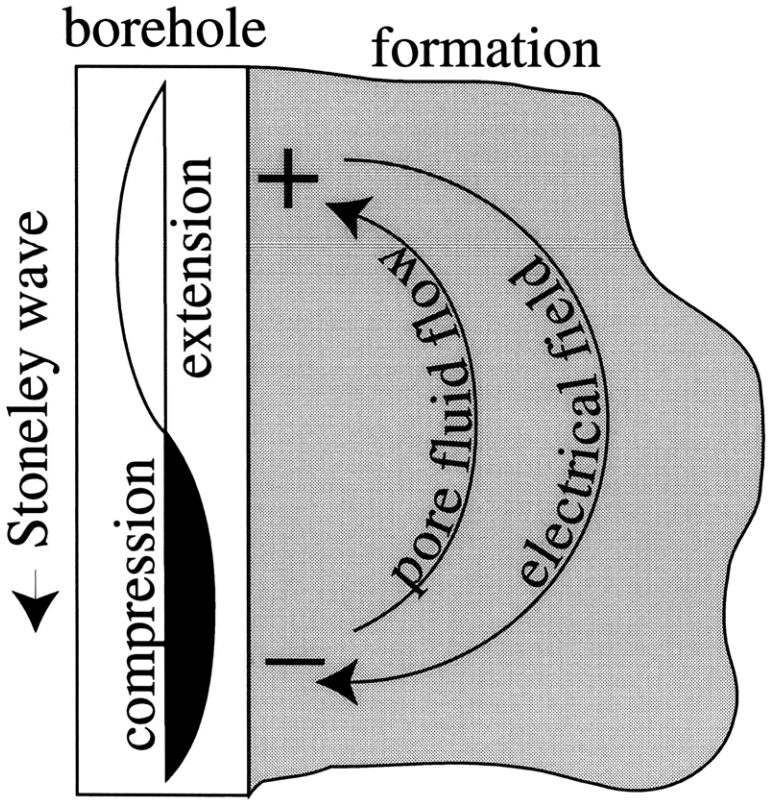

Figure 2-1: Diagram of an electrical field induced by a borehole Stoneley wave. A Stoneley wave propagating in a borehole creates a pressure gradient in a rock formation. This pressure gradient drives the pore fluid flow from the zone of compression to the zone of extension. If the fluid carries an excess positive electrical charge, then the flow results in accumulation of a positive electrical charge in the zone of extension and a negative electrical charge in the zone of compression. Thus, the Stoneley wave creates a capacitor-like electrical charge separation that moves along the borehole together with the wave. This charge separation induces an electrical field that also moves along the borehole together with the Stoneley wave.

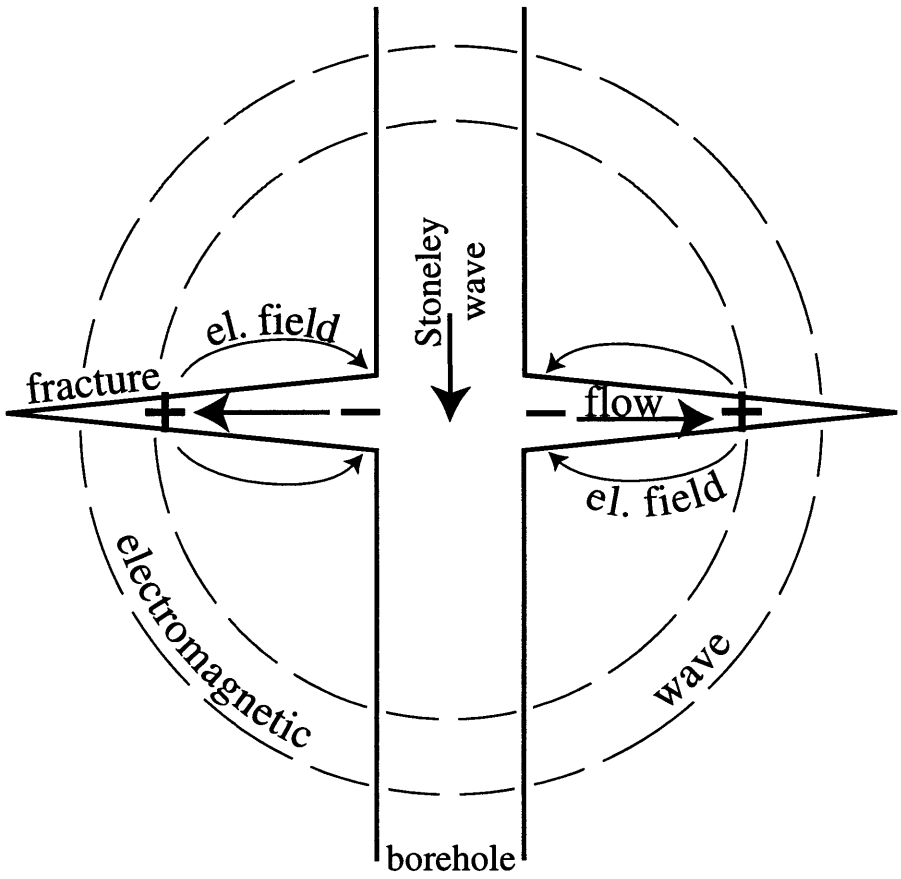

Figure 2-2: Diagram of a Stoneley wave locally inducing an electrical field and generating an electromagnetic wave radiation at an isolated fracture. The Stoneley wave creates an oscillating flow of fluid within the fracture. This flow carries a streaming electrical current that results in an oscillating charge separation within the fracture. The oscillating electrical charge induces an electrical field within and in the vicinity of the fracture. Also, this oscillating electrical charge radiates an electromagnetic wave that propagates in all directions with a velocity much higher than velocities of seismic waves.

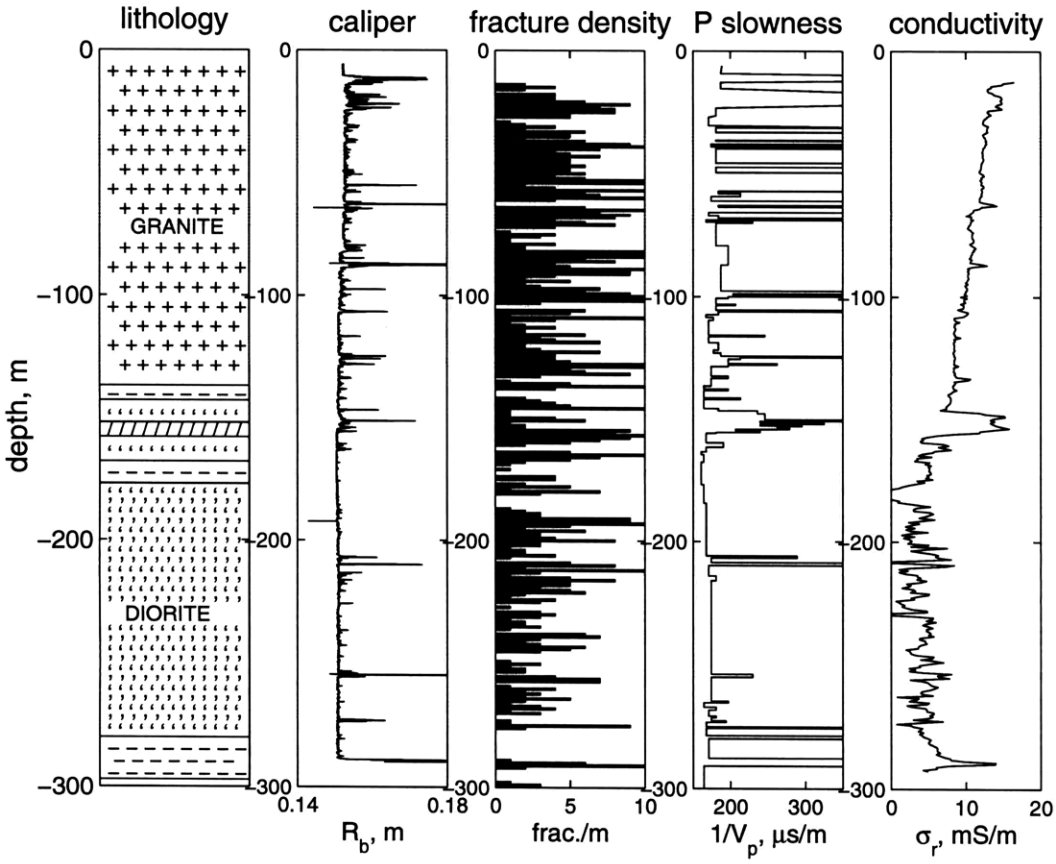

Figure 2-3: Lithology description and results of various geophysical measurements for the well in Hamilton, Massachusetts, where we made electroseismic measurements. The top $137m$ of the well is in granite and below $137m$ is in diorite. Within the diorite section there are three zones of monzodiorite $5m$, $9m$ and $17m$ thick at depths of $137m$, $168m$ and $280m$, respectively. A $6m$ felsite dike intersects the well at the depth of $152m$. The caliper log, the fracture density log and the P-wave slowness logs demonstrate that both the granite and diorite sections of the well are fractured.

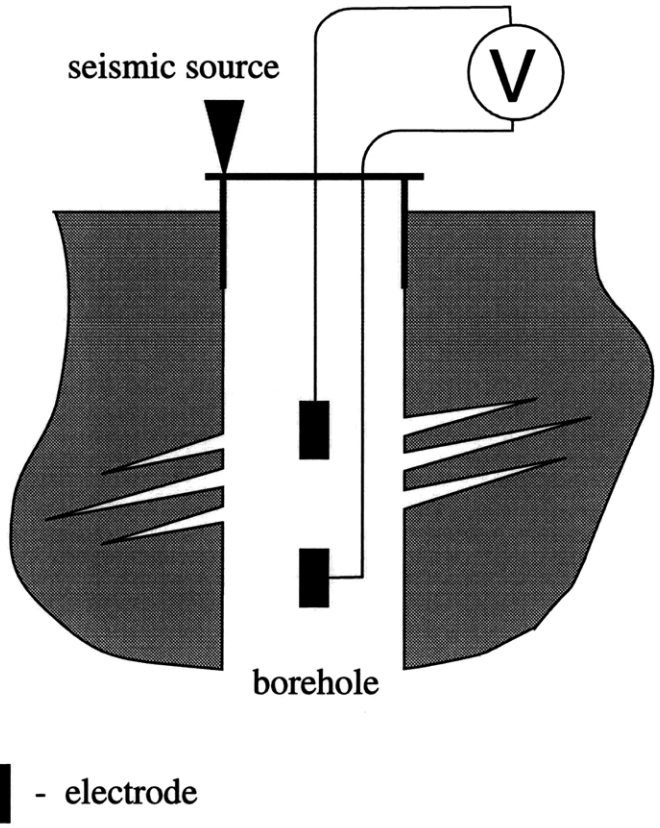

Figure 2-4: Diagram of the electrical measurements. We generated a Stoneley wave at the top of the well by striking the casing with a sledge hammer. We measured the electrical field induced by the Stoneley wave as a potential difference between two lead electrodes. The electrodes were suspended in the borehole fluid and were connected to a data acquisition system at the surface by an unarmored cable.

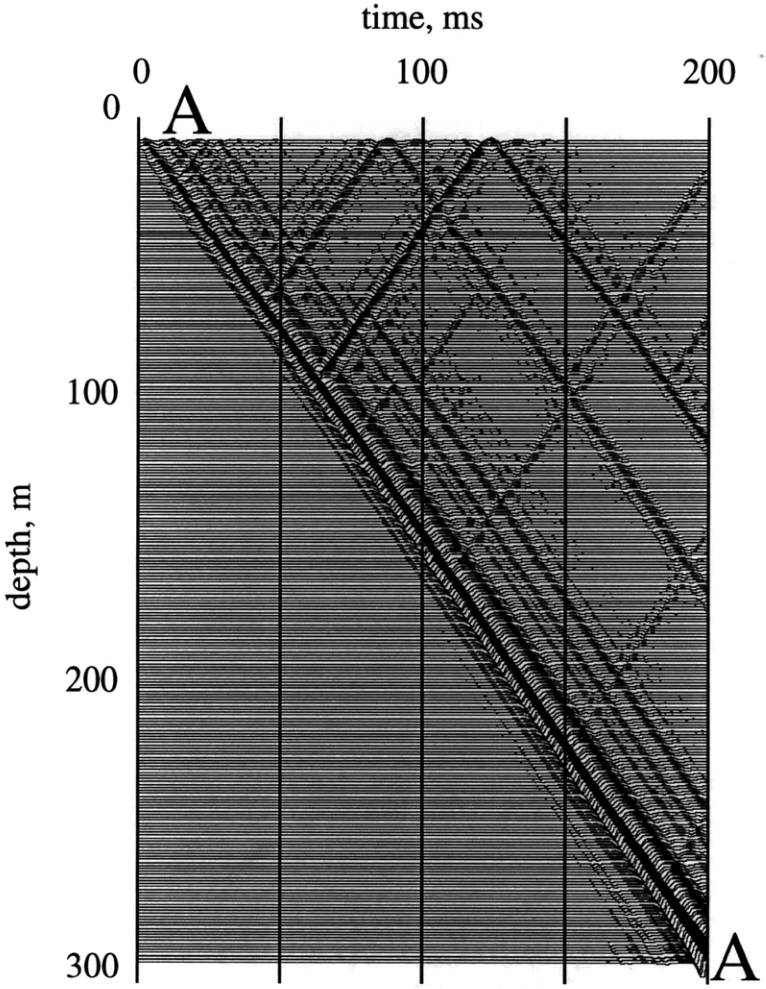

Figure 2-5: Pressure measurements. All the traces are plotted with no AGC. Each trace is individually scaled by its maximum amplitude. Event A-A is the direct Stoneley wave propagating from the top of the well.

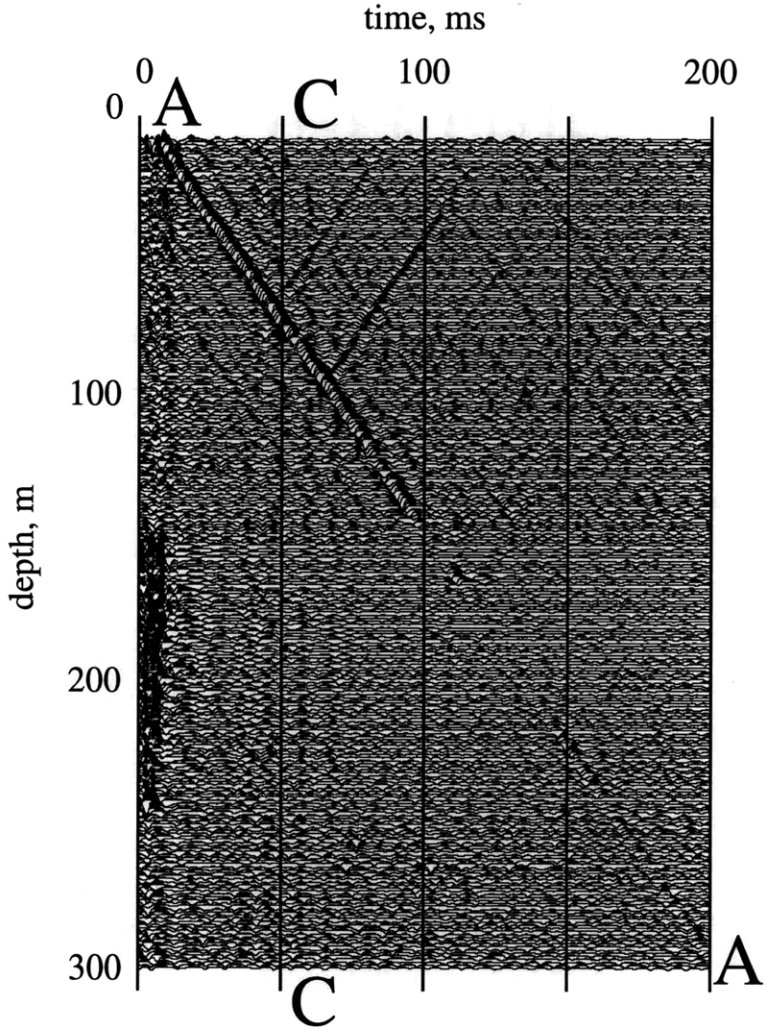

Figure 2-6: Electrical signals recorded using electrode pairs separated by $0.5m$. All the traces are plotted with no AGC. Each trace is individually scaled by its maximum amplitude. Event A-A is the electrical field induced by the direct Stoneley wave. This electrical field moves along the borehole together with the Stoneley wave. Event C-C is an electromagnetic wave generated by the direct Stoneley wave at a large fracture at the depth of $87m$. This electromagnetic wave propagates with a velocity much higher than velocities of seismic waves.

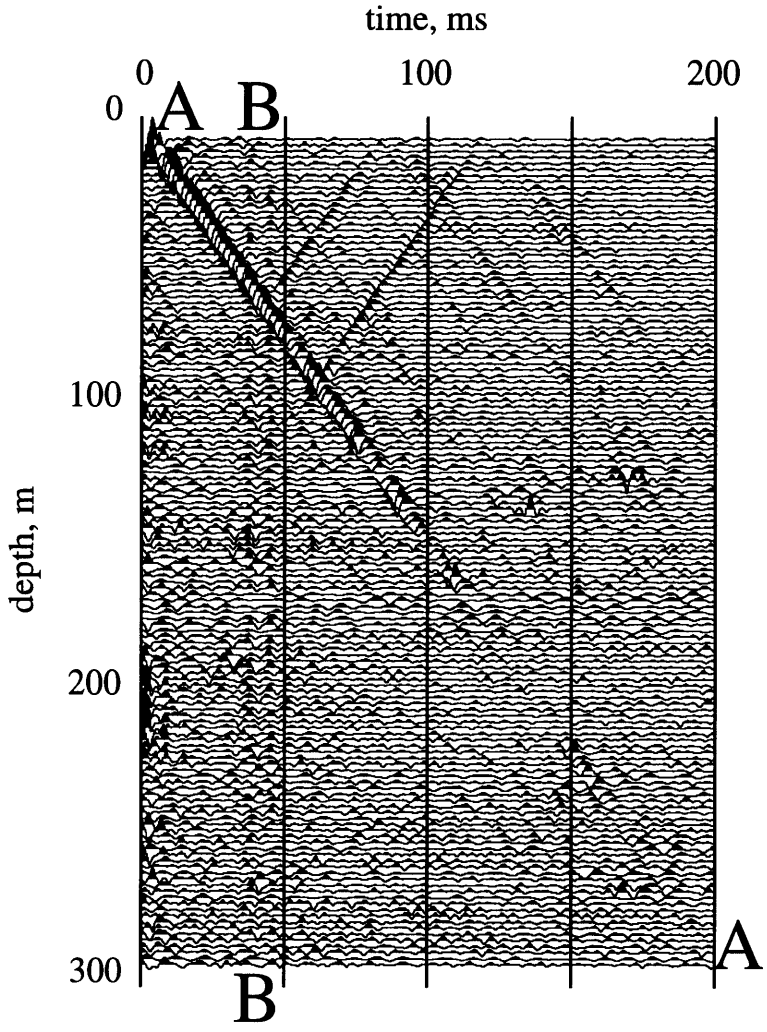

Figure 2-7: Electrical signals recorded using electrode pairs separated by $1.0m$. All the traces are plotted with no AGC. Each trace is individually scaled by its maximum amplitude. Event A-A is the electrical field induced by the direct Stoneley wave. This electrical field moves along the borehole together with the Stoneley wave. Event B-B is an electromagnetic wave generated by the direct Stoneley wave at a large fracture at the depth of $63m$. This electromagnetic wave propagates with a velocity much higher than velocities of seismic waves.

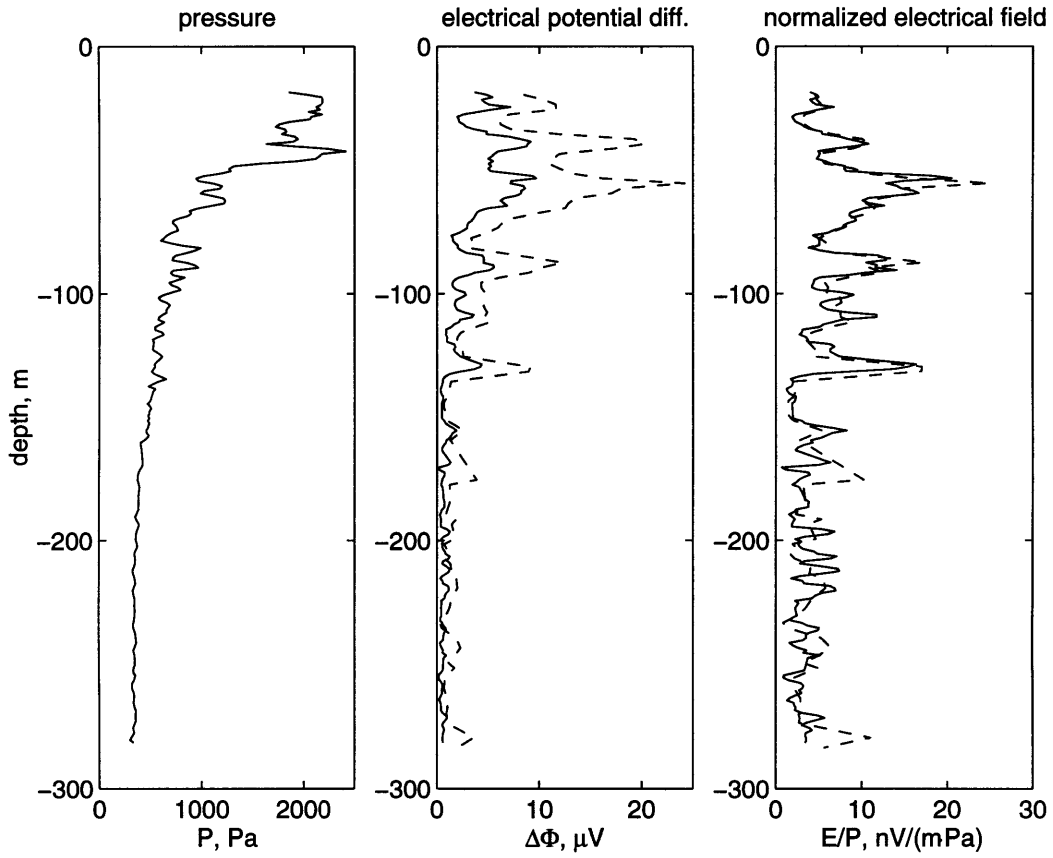

Figure 2-8: Derivation of the normalized amplitude of the Stoneley-wave-induced electrical field from the field data. The first plot is the rms amplitude of the pressure oscillation in the direct Stoneley wave. The second plot is the rms amplitude of the electrical potential difference recorded by electrode pairs with a $0.5m$ separation (solid line) and by electrode pairs with a $1.0m$ separation (dashed line). The third plot is the normalized amplitude of the Stoneley-wave-induced electrical field. To calculate it we divided the potential difference amplitude at each depth by the distance between the electrodes and by the amplitude of the pressure oscillation at the same depth. The normalized amplitudes of the Stoneley-wave-induced electrical fields measured in two different experiments using a $0.5m$ electrode separation (solid line) and $1.0m$ electrode separation (dashed line) agree.

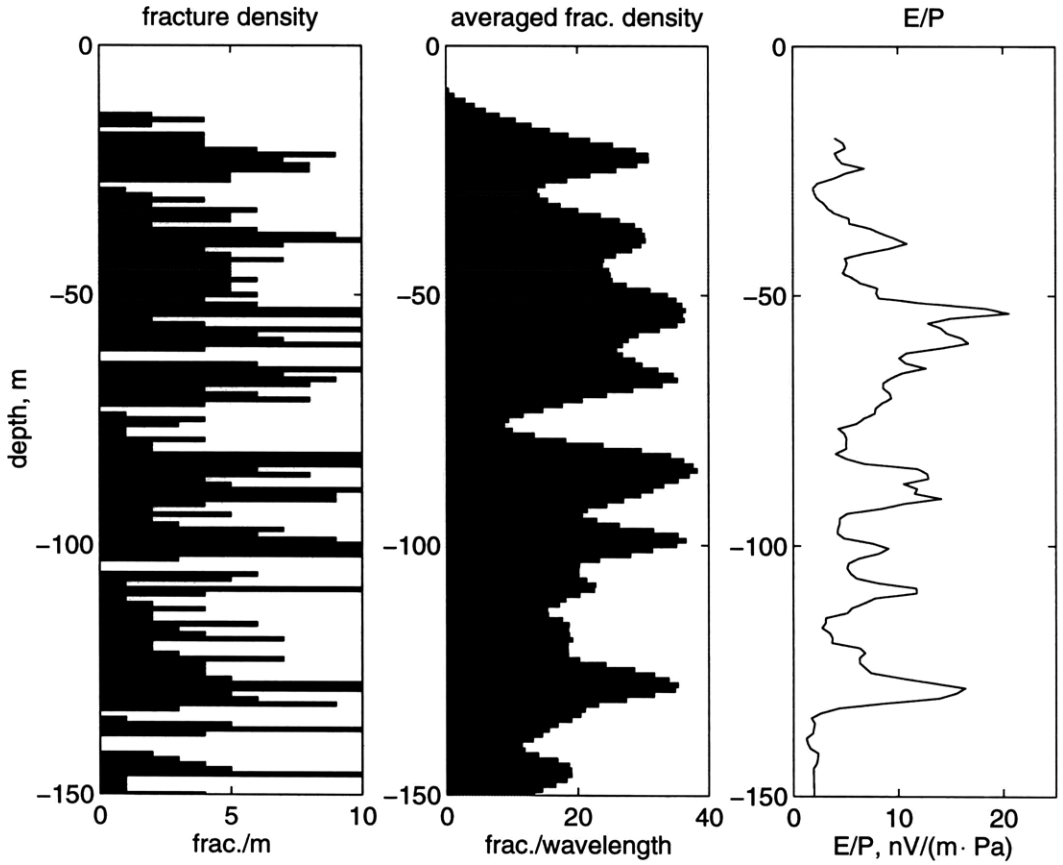

Figure 2-9: Comparison between the fracture density log for the granite section of the well and the normalized amplitude of the Stoneley-wave-induced electrical fields. The first plot is the fracture density (the number of fractures per meter) derived from the borehole video log. The second plot is the fracture density log averaged over the Stoneley wavelength ($9.3m$ in the experiment) using a cosine-shaped weighting function. The third plot is the normalized amplitude of the Stoneley-wave-induced electrical field. The normalized amplitudes of the electrical fields correlate with the averaged fracture density. The more fractures there are around a certain depth, the higher the normalized amplitude of the Stoneley-wave-induced electrical field is.

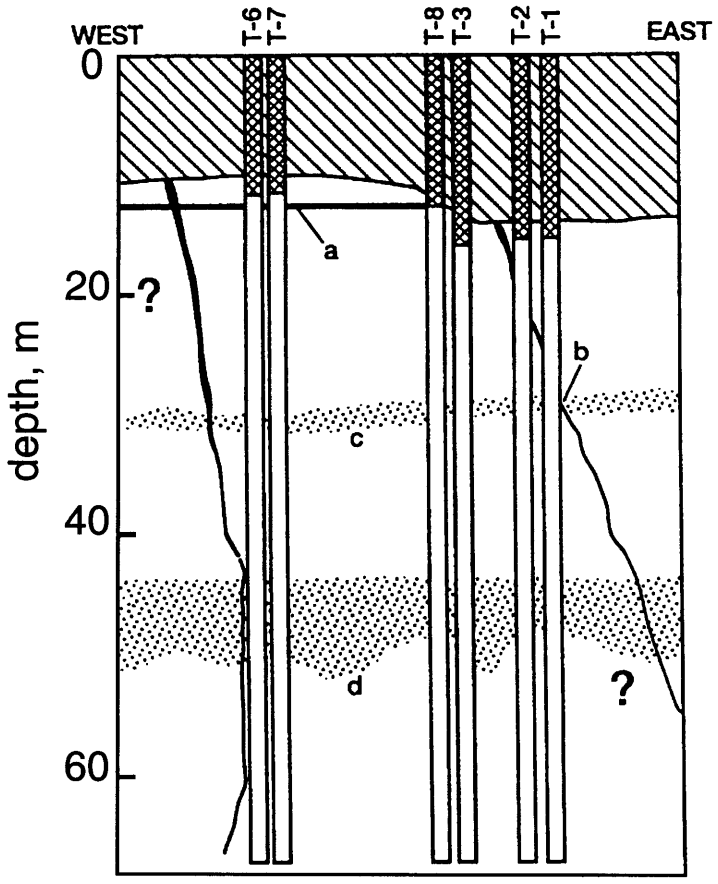

Figure 2-10: A vertical cross-section of the subsurface at the site in Belvidere, Illinois (from Paillet (1997)). The locations and connectivity of permeable zones and fractures in the subsurface were determined by cross-borehole pumping tests and by borehole flowmeter measurements. In the diagram: a is a permeable bedding plane, b is a nearly vertical fracture, c and d are porous permeable zones. The vertical fracture b intersects boreholes T1 and T2 around the depth of $25m$. The width of the intersection is $3.1m$ in borehole T1 and $1.7m$ in borehole T2. Electroseismic measurements were made in wells T1, T2, T6 and T7.

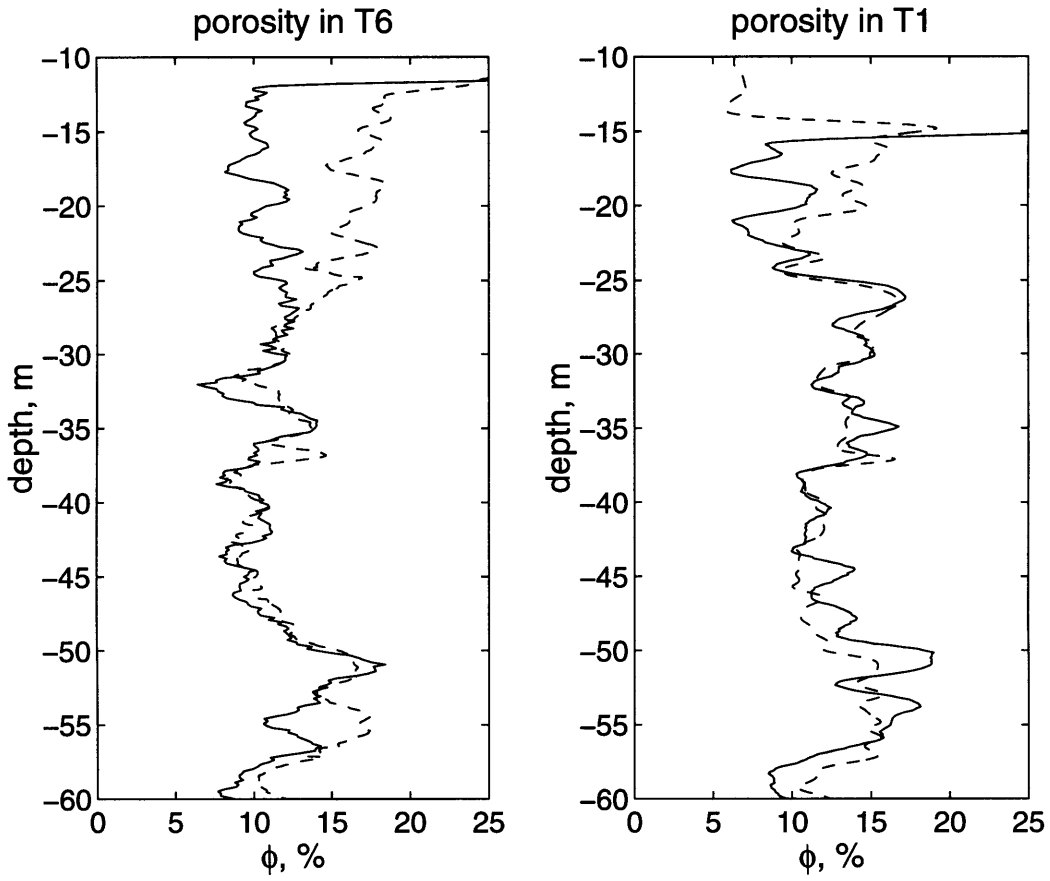

Figure 2-11: Porosity logs deduced from neutron logs (solid line) and from sonic logs (dashed line) in boreholes T6 and T1. In borehole T1, the neutron and the sonic porosity logs have the same values and the same variation with depth. This match demonstrates that the procedure that we used to deduce porosity from the sonic and the neutron logs is correct. In borehole T6, the neutron and the sonic porosity logs agree below the depth of $25m$. Above the depth of $25m$, the sonic log deviates towards higher porosity values but has the same variation with depth as the neutron porosity log. This deviation indicates that at the depth of $25m$ the lithological composition of the formation changes.

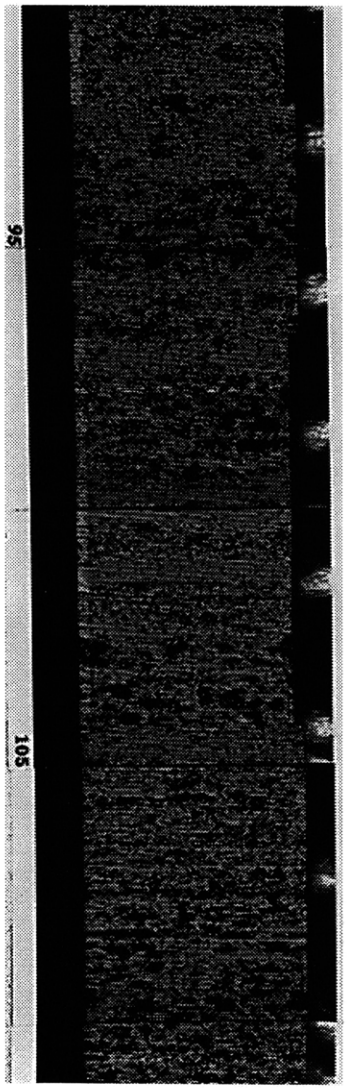

Figure 2-12: A section of a borehole televiewer image in borehole T1. This image is of the depth interval from $27.5m$ $(90ft)$ to $33.5m$ $(110ft)$. Black areas in the televiewer image are vugs in the dolomite. While contributing to porosity, the vugs do not necessarily contribute to permeability.

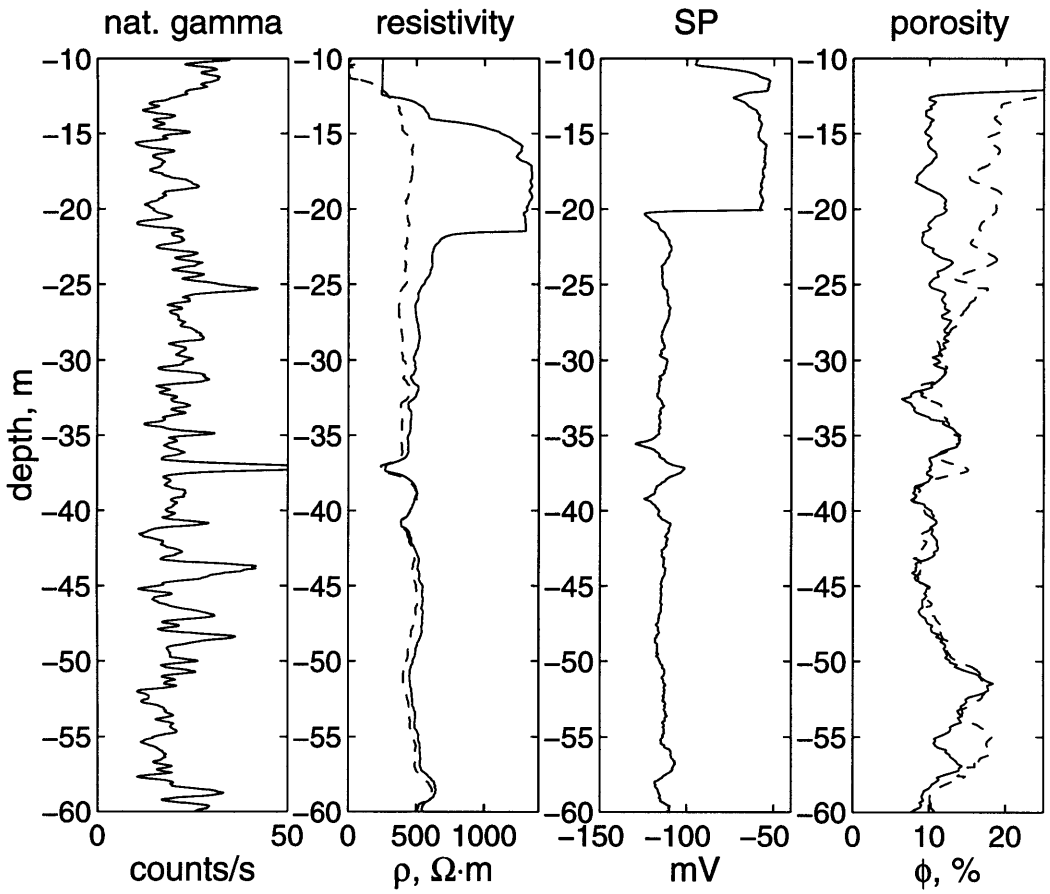

Figure 2-13: Results of various logging measurements in borehole T6. The gamma log has several peaks that indicate shale layers. The resistivity log is almost uniform below the depth of $23m$. Also, below the depth of $23m$, the resistivity log in borehole T6 agrees with the resistivity log in borehole T7 (dashed line). The high resistivity anomaly above the depth of $23m$ is interpreted to be due to the infiltration of fresh water from melted snow. This interpretation is consistent with the SP anomaly at the depth of $21m$.

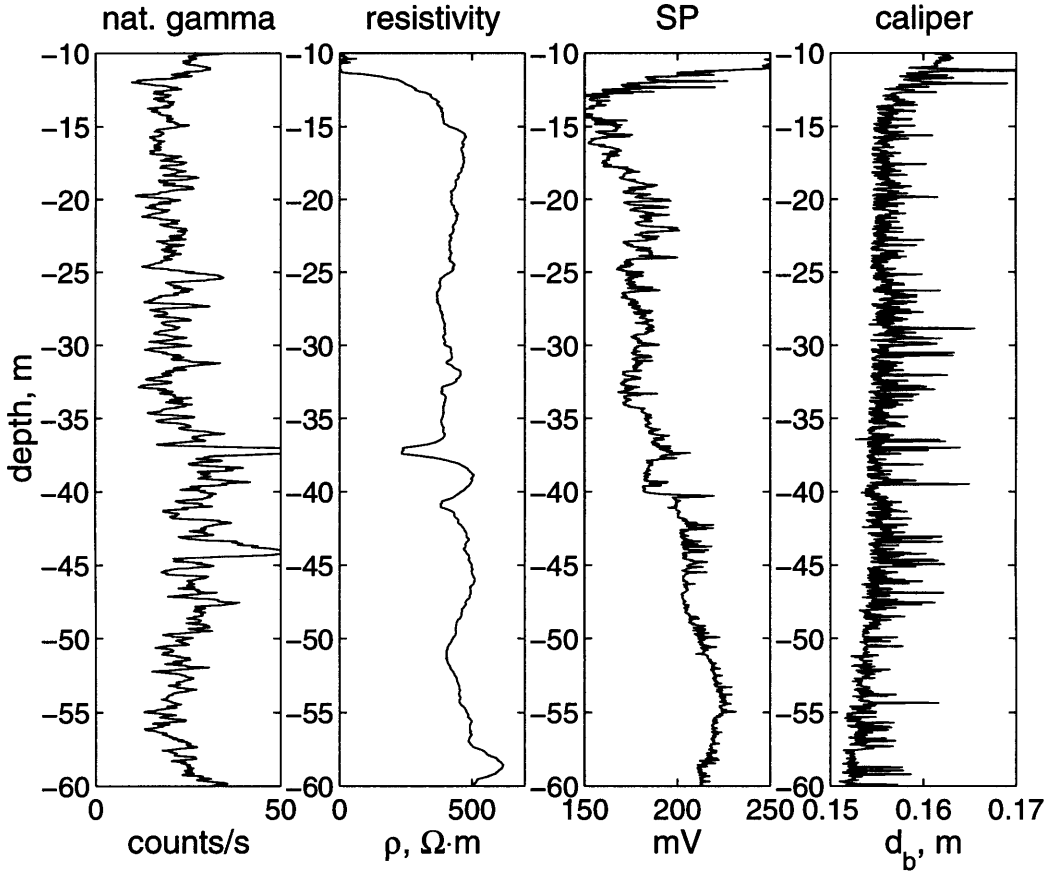

Figure 2-14: Results of various logging measurements in borehole T7. The gamma log in borehole T7 is similar to the one in borehole T6. The resistivity log is almost uniform and does not have an anomaly at the depth of $23m$. The SP log also does not have any anomaly at the $23m$ depth. The caliper log is highly irregular. This irregularity is due to vugs in the dolomite.

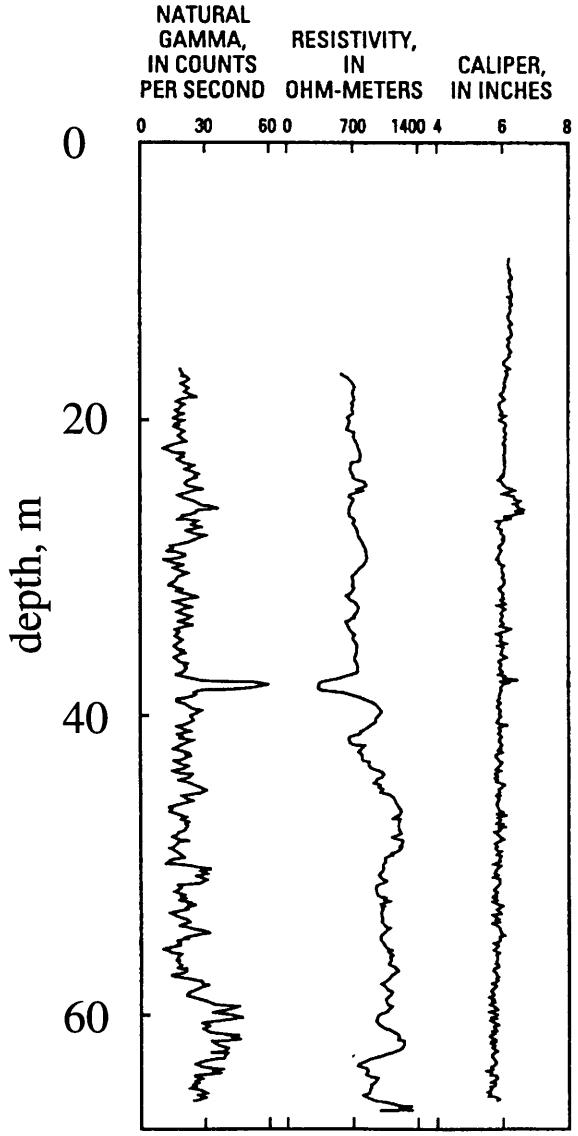

Figure 2-15: Results of various logging measurements in borehole T2 (from Paillet, 1997). The gamma log and the resistivity log in borehole T2 are similar to those in borehole T7. The caliper log identifies the isolated fracture at the depth of $25m$.

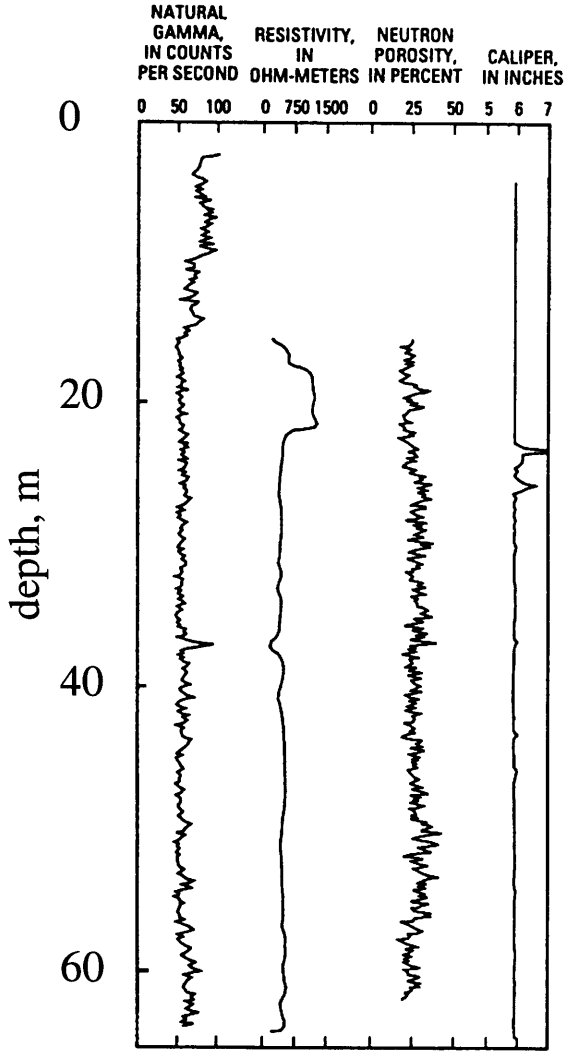

Figure 2-16: Results of various logging measurements in borehole T1 (from Paillet, 1997). The gamma log and the resistivity log in borehole T1 are similar to those in borehole T2. The caliper log identifies the isolated fracture at the depth of $25m$. The neutron porosity log plotted by Paillet (1997) represents values of the "apparent limestone porosity", i.e., it is shifted towards higher values.

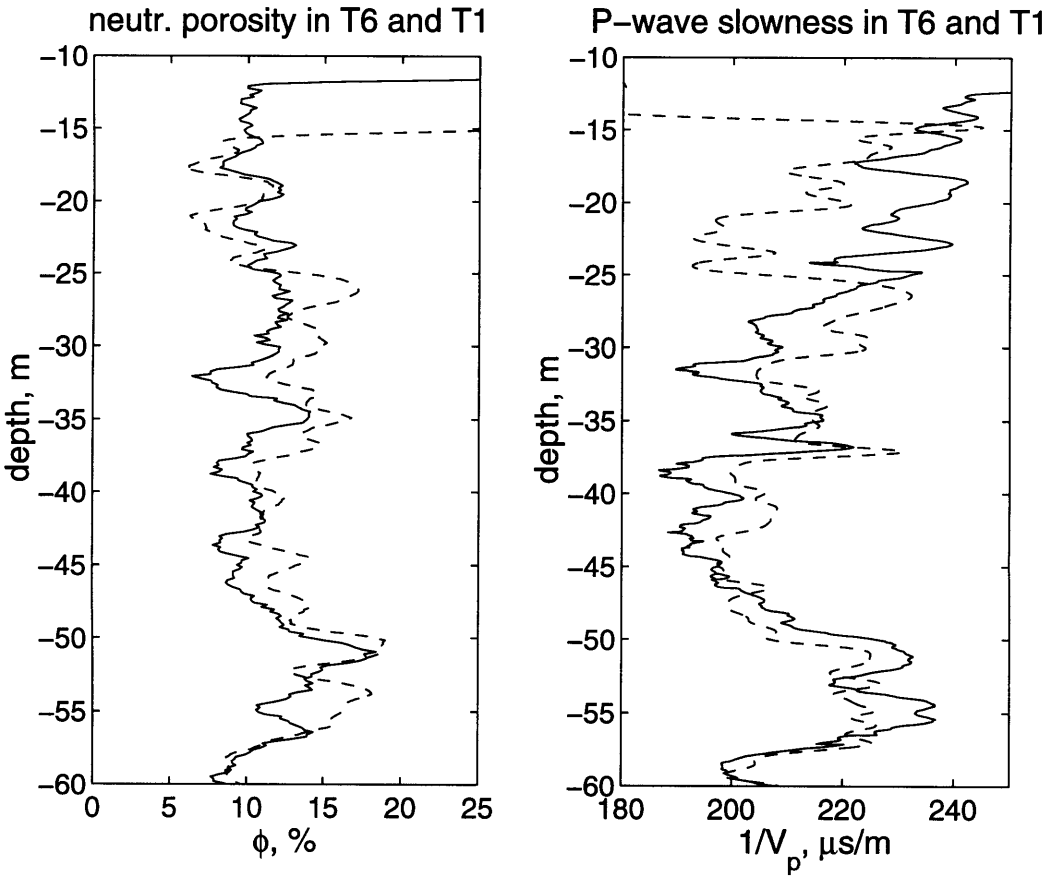

Figure 2-17: Comparison of neutron porosity and P-wave slowness logs in boreholes T6 (solid lines) and T1 (dashed lines). The neutron porosity logs in boreholes T6 and T1 match in the depth interval from $16m$ to $60m$. The P-wave slowness logs in boreholes T6 and T1 correlate in the depth interval from $25m$ to $60m$. Above the depth of $25m$ there is a significant mismatch between these two logs. This mismatch is due to the change of lithological composition in the formation around borehole T6 at the depths above $25m$.

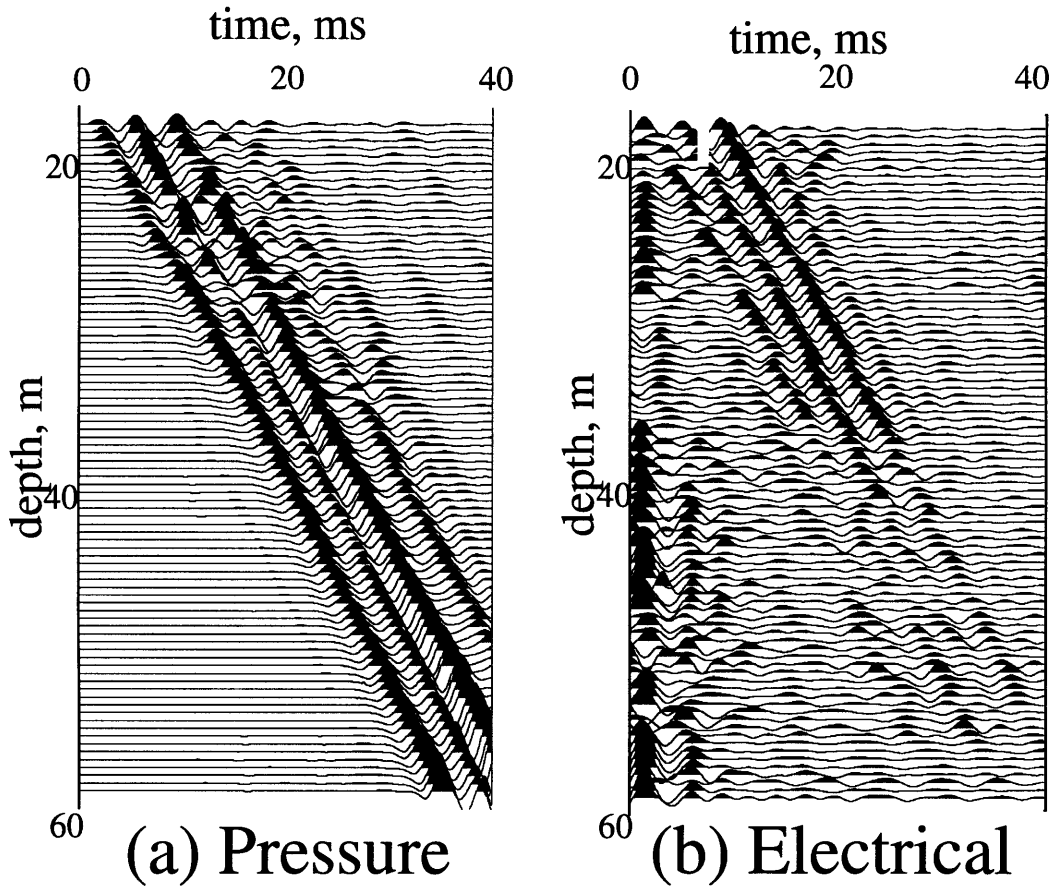

Figure 2-18: Pressure and electrical measurements in borehole T1. All the traces are plotted with no AGC. Each trace is individually scaled by its maximum amplitude. The electrical data shows two events. The first event is an electrical signal that arrives simultaneously at all depths at time zero. This event is an electromagnetic wave generated by striking the metal casing with a metal sledgehammer. The second event is an oscillating electrical field that moves along the borehole together with the Stoneley wave. This electrical field is induced by the Stoneley-wave-generated flow of pore fluid in the formation around the borehole.

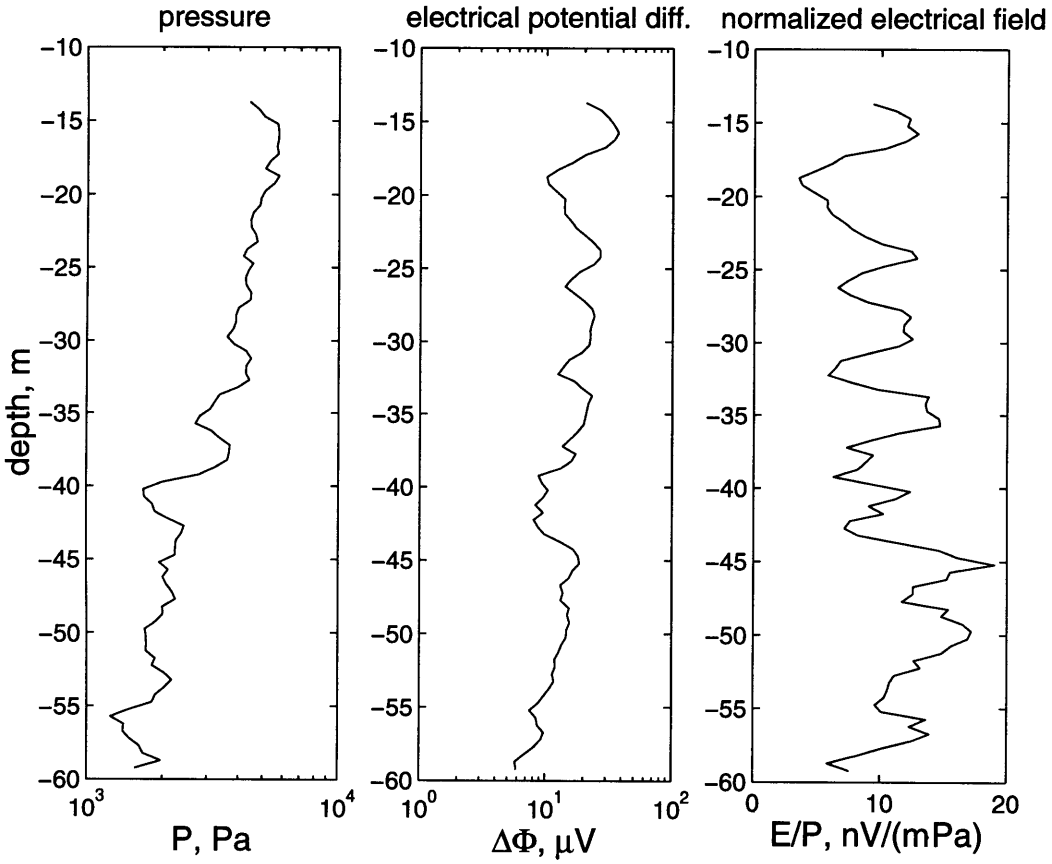

Figure 2-19: Amplitudes of pressure and electrical potential oscillations generated by the Stoneley wave in borehole T6 and the normalized amplitude of the Stoneley-wave-induced electrical field. This normalized amplitude is defined as the ratio of the amplitude of the electrical field oscillation to the amplitude of the pressure oscillation at the same depth.

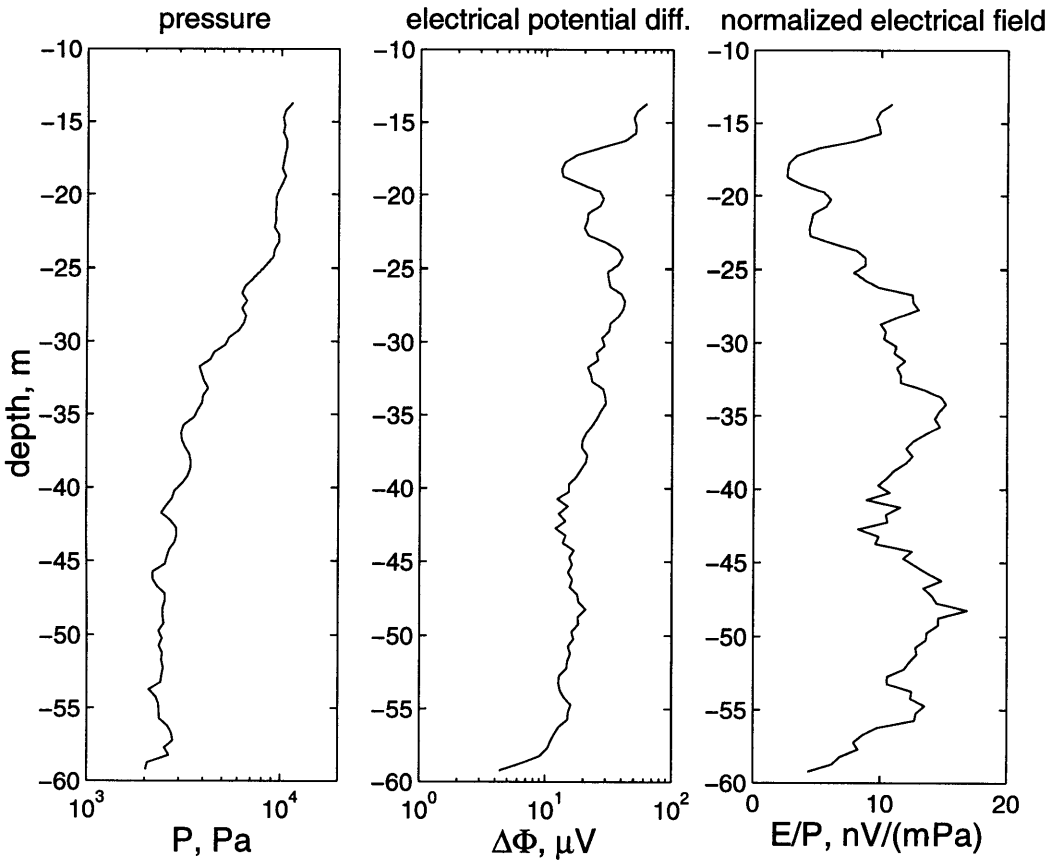

Figure 2-20: Amplitudes of pressure and electrical potential oscillations generated by the Stoneley wave in borehole T7 and the normalized amplitude of the Stoneley-wave-induced electrical field. This normalized amplitude is defined as the ratio of the amplitude of the electrical field oscillation to the amplitude of the pressure oscillation at the same depth.

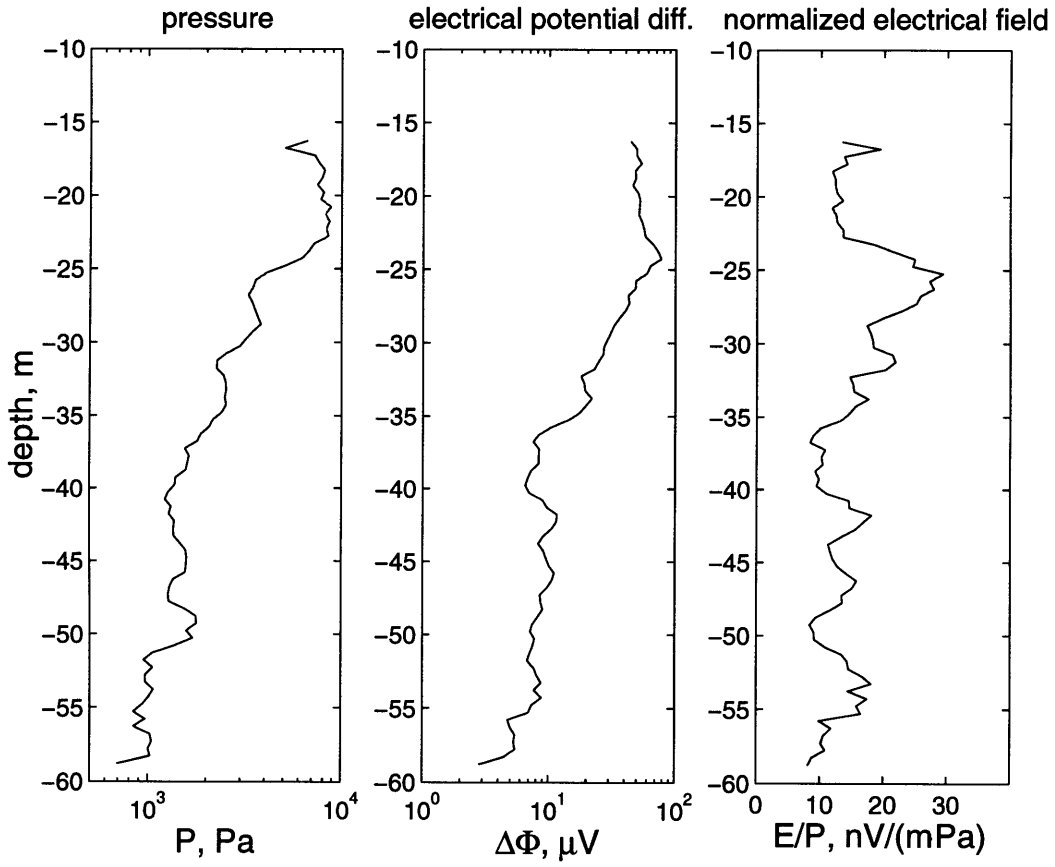

Figure 2-21: Amplitudes of pressure and electrical potential oscillations generated by the Stoneley wave in borehole T2 and the normalized amplitude of the Stoneley-wave-induced electrical field. This normalized amplitude is defined as the ratio of the amplitude of the electrical field oscillation to the amplitude of the pressure oscillation at the same depth.

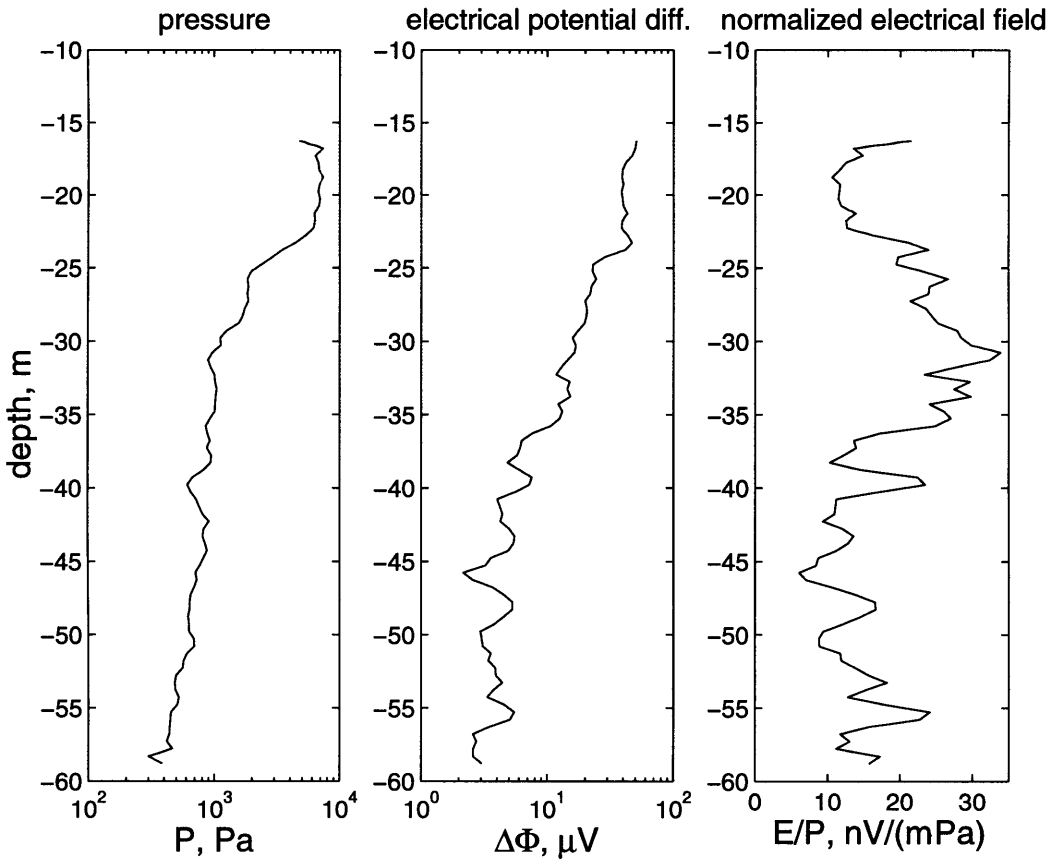

Figure 2-22: Amplitudes of pressure and electrical potential oscillations generated by the Stoneley wave in borehole T1 and the normalized amplitude of the Stoneley-wave-induced electrical field. This normalized amplitude is defined as the ratio of the amplitude of the electrical field oscillation to the amplitude of the pressure oscillation at the same depth.

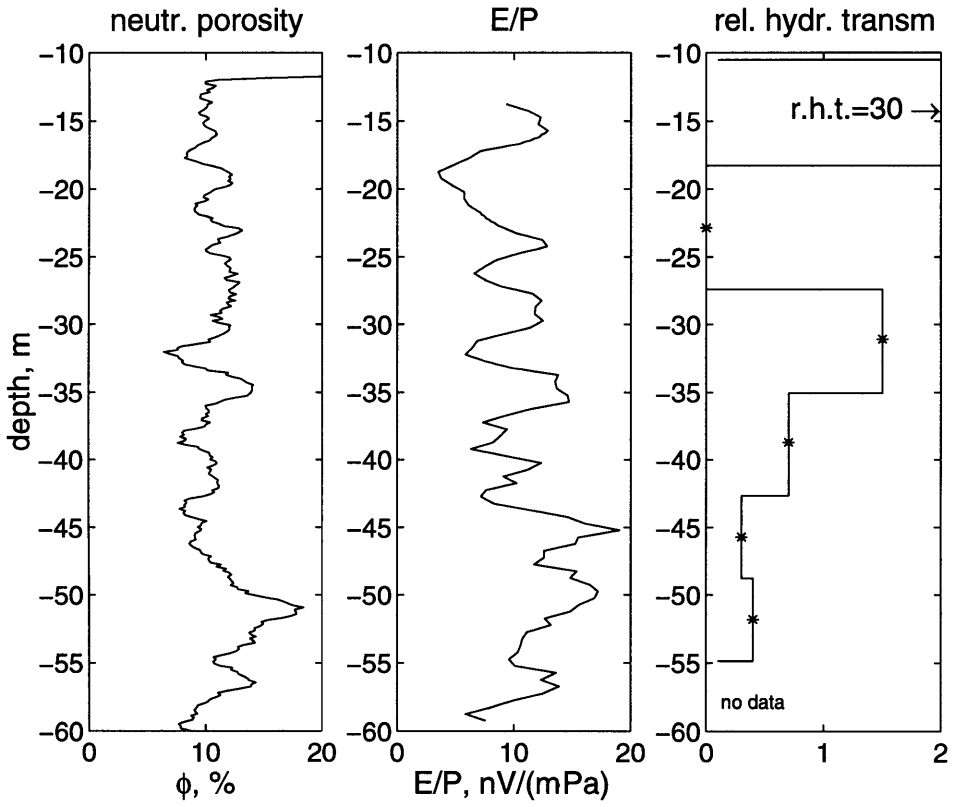

Figure 2-23: Comparison of the neutron porosity log, the normalized amplitude of the Stoneley-wave-induced electrical fields and the relative hydraulic transmissivity measurements in borehole T6. The normalized electroseismic amplitude correlates with the porosity log. At the same time, the normalized electroseismic amplitude does not correlate with the relative hydraulic transmissivity. The porosity log does not correlate with the relative hydraulic transmissivity.

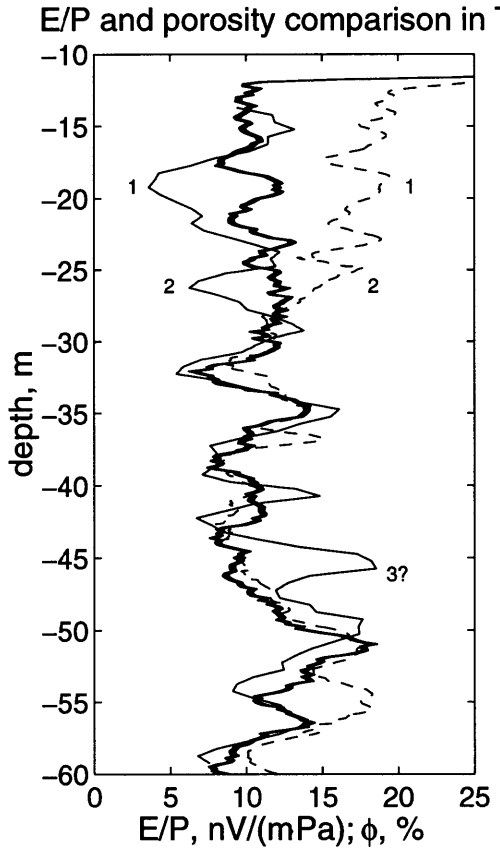

Figure 2-24: Direct comparison between the normalized amplitude of the Stoneley-wave-induced electrical field (the thin solid line), the neutron porosity log (the thick solid line) and the sonic porosity log (thin dashed line). The normalized electroseismic amplitude closely matches the neutron porosity log in the depth intervals from $27m$ to $44m$ and from $47m$ to $60m$. The normalized electroseismic amplitude and the neutron porosity have significant mismatches above the depth of $27m$ (1 and 2) and around the depth of $45m$ (3). Above the depth of $27m$, the sonic porosity log deviates from the neutron porosity log towards higher values. At the same time, the normalized electroseismic amplitude deviates from the neutron porosity log towards lower values. Thus, mismatches 1 and 2 can be attributed to a change in lithological composition of the formation.

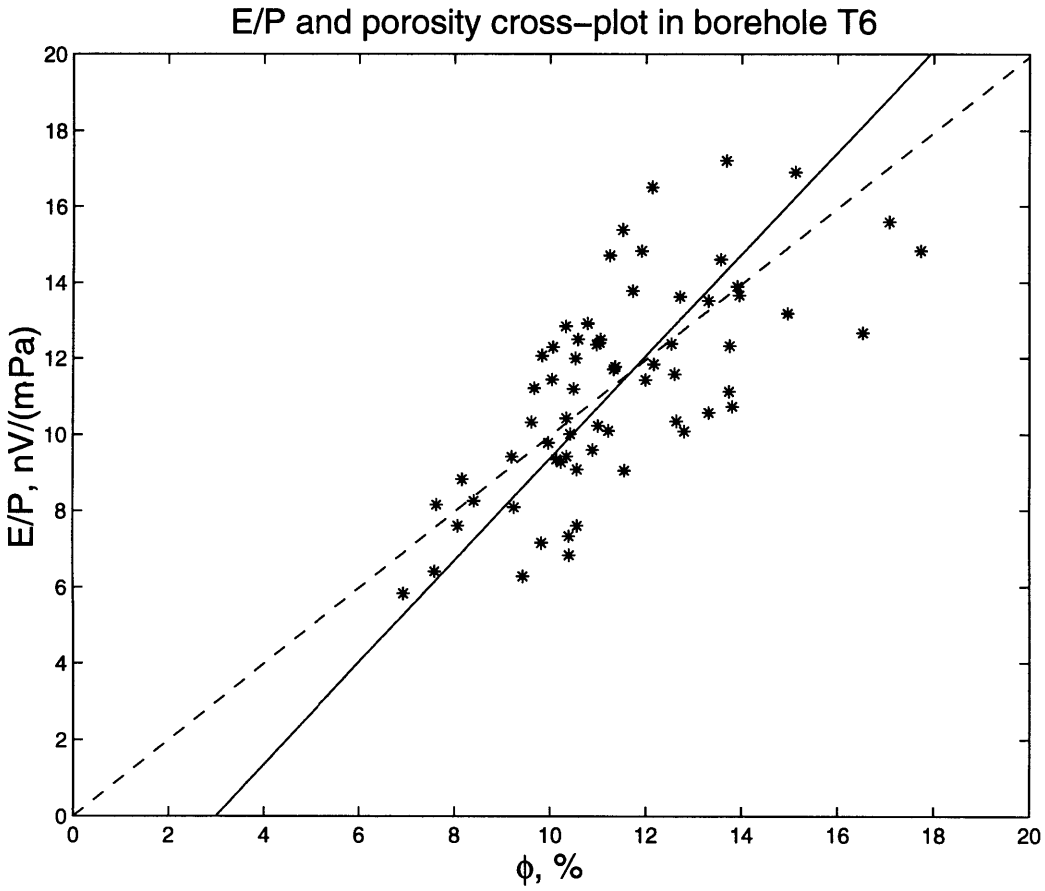

Figure 2-25: Cross-plot of the porosity and the normalized electroseismic amplitude in the depth intervals from $27m$ to $44m$ and from $47m$ to $60m$. The solid line is the best linear fit to the data. The correlation coefficient between the porosity and the normalized electroseismic amplitude is 0.69. The average deviation from the linear trend (dashed line) is $1.96\frac{nV}{m \cdot Pa}$.

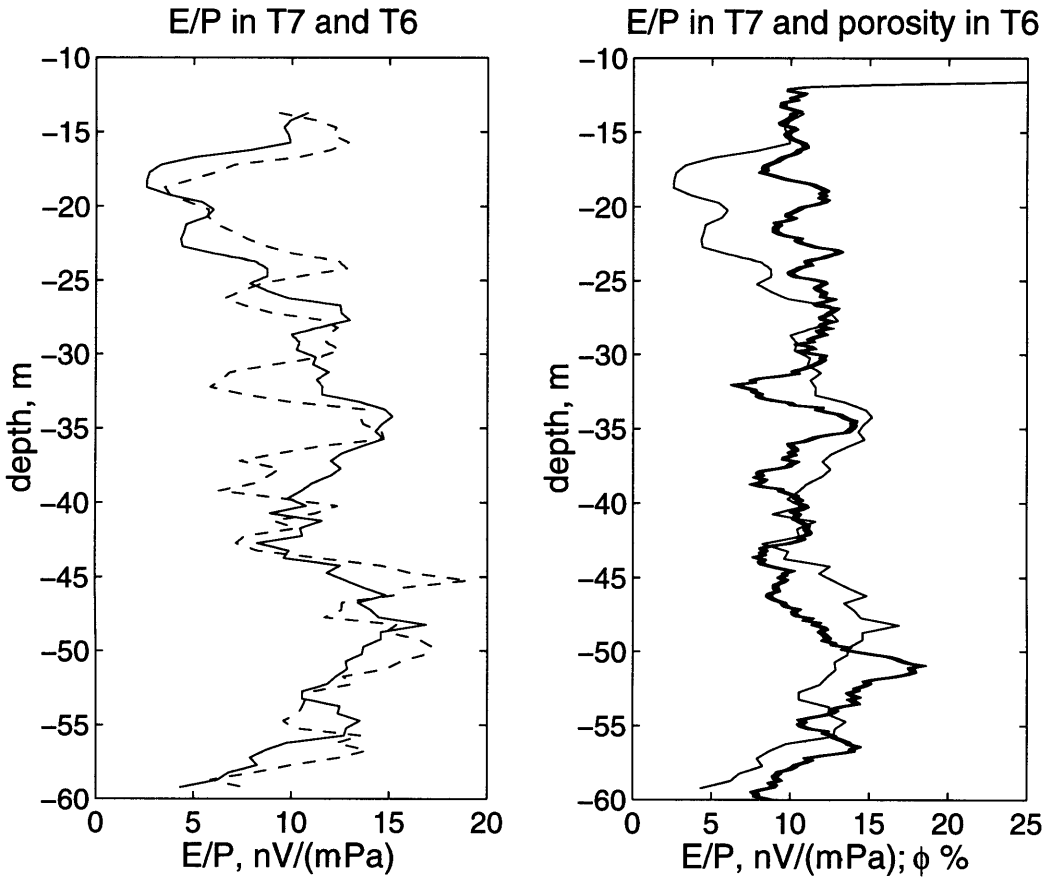

Figure 2-26: Comparison between the normalized electroseismic amplitudes in boreholes T7 (solid line) and T6 (dashed line) and comparison between the neutron porosity log in borehole T6 (thick solid line) and the normalized electroseismic amplitude in borehole T7 (thin solid line). The normalized electroseismic amplitudes in boreholes T6 and T7 agree in values and have similar variation with depth. Also the normalized electroseismic amplitude in borehole T7 agrees with the neutron porosity log below the depth of $27m$.

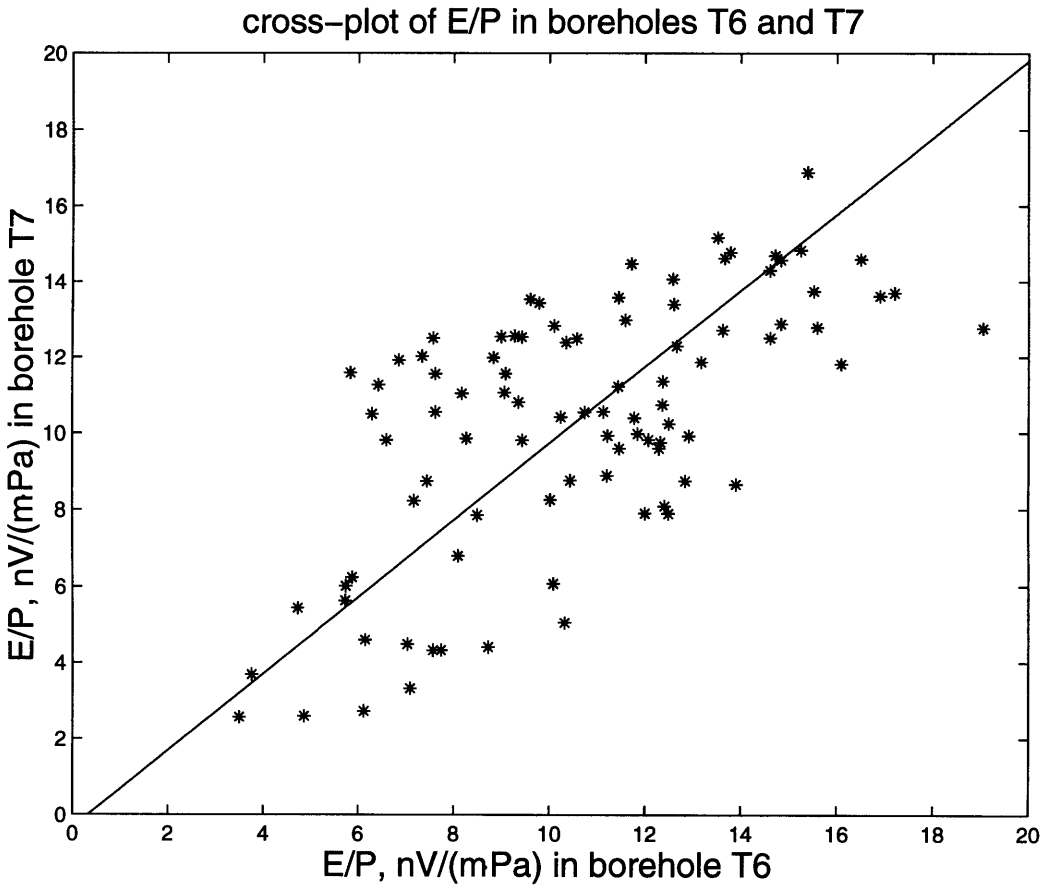

Figure 2-27: Cross-plot of the normalized electroseismic amplitude values in boreholes T6 and T7. The solid line is the best linear fit to the data. The average deviation from the linear trend is $2.7\frac{nV}{m \cdot Pa}$. The correlation coefficient between the E/P-versus-depth curves in boreholes T6 and T7 is 0.66.

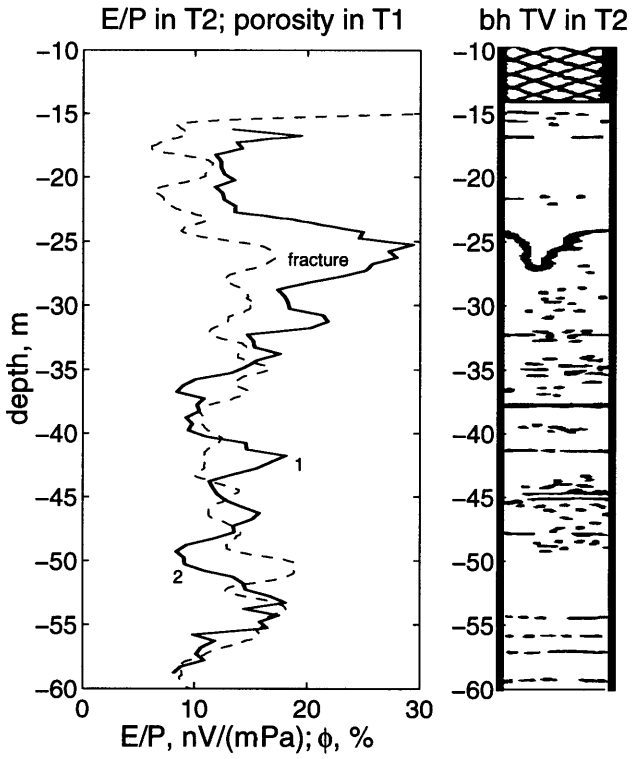

Figure 2-28: Comparison between the normalized amplitude of the Stoneley-wave-induced electrical field in borehole T2 (solid line) and the neutron porosity log in borehole T1 (dashed line). Above the depth of $23m$ and below the depth of $30m$, the normalized electroseismic amplitude correlates with the neutron porosity log. At the depth of $25m$, the Stoneley-wave-induced electrical field has an anomalously high amplitude of $30\frac{nV}{m \cdot Pa}$. This value is almost 3 times higher than the averaged value in boreholes T6 and T7. The borehole televiewer image in borehole T2 shows that this high amplitude anomaly is at the depth of the isolated fracture.

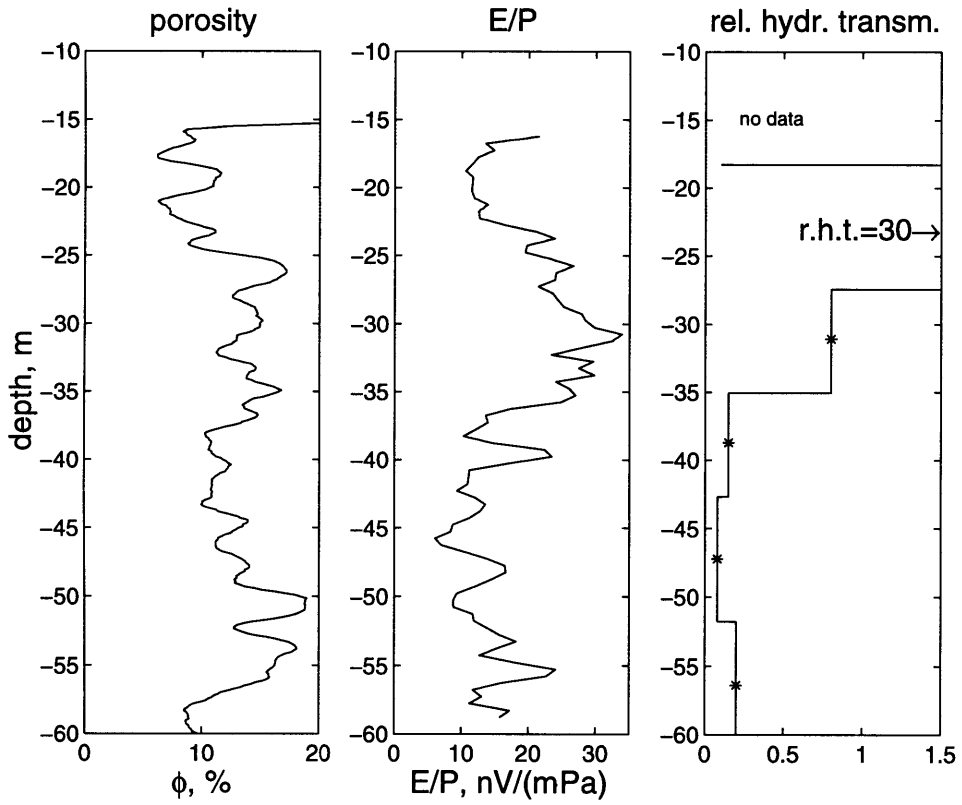

Figure 2-29: Comparison of the neutron porosity log, the normalized amplitude of the Stoneley-wave-induced electrical fields and the relative hydraulic transmissivity measurements in borehole T1. The normalized electroseismic amplitude does not correlate with the relative hydraulic transmissivity. There is a similarity between the general trends of the normalized electroseismic amplitude and the neutron porosity log. The porosity log does not correlate with the relative hydraulic transmissivity.

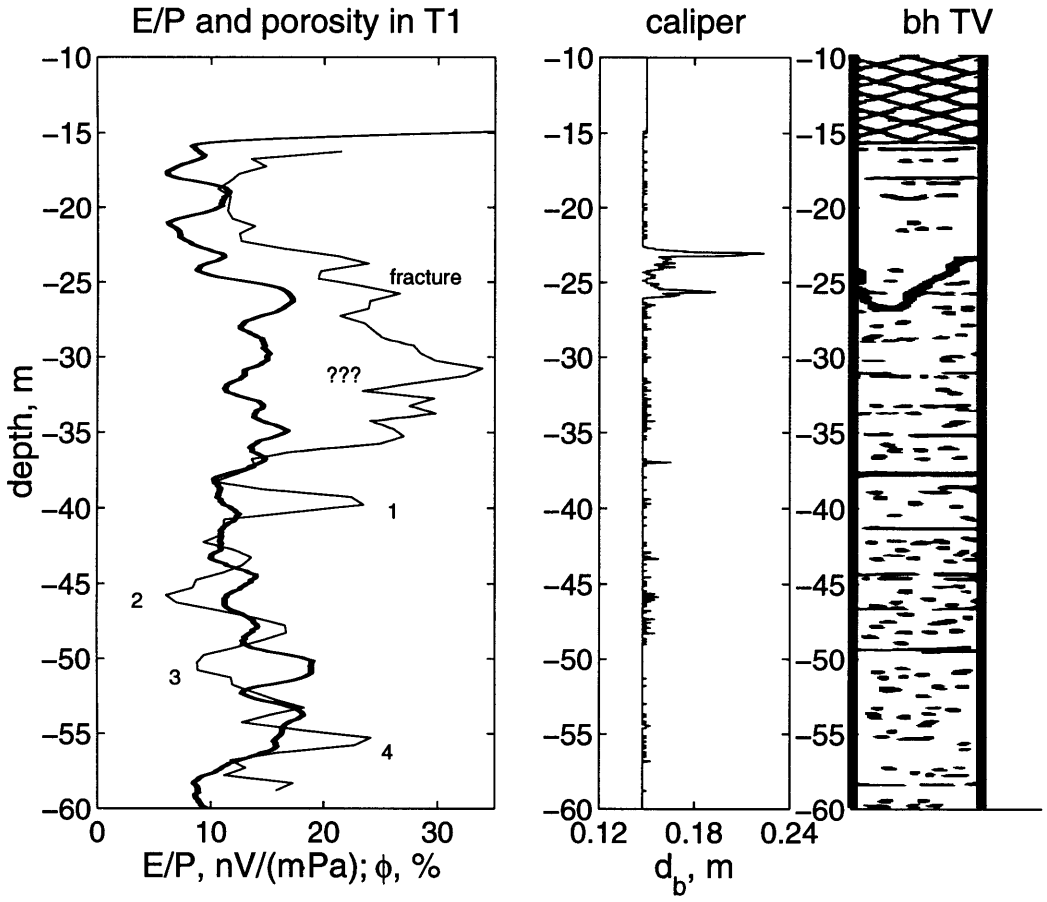

Figure 2-30: Comparison between the normalized electroseismic amplitude (thin solid line) and the neutron porosity log (thick solid line) in borehole T1. Below the depth of $41m$ and above the depth of $23m$ the values of the normalized electroseismic amplitudes in $\frac{nV}{m \cdot Pa}$ roughly agree with the values of the porosity log in percent. This result is consistent with the results of electroseismic measurements in boreholes T6, T7 and T2. However, there are several significant mismatches between the two curves. Further, the Stoneley-wave-induced electrical fields have anomalously high amplitudes around the depth of the near vertical fracture. These anomalously high amplitudes are similar to the ones observed in borehole T2. Finally, the Stoneley-wave-induced electrical fields have anomalously high amplitudes between the depths of $28m$ and $37m$. This anomaly is not observed in borehole T2.

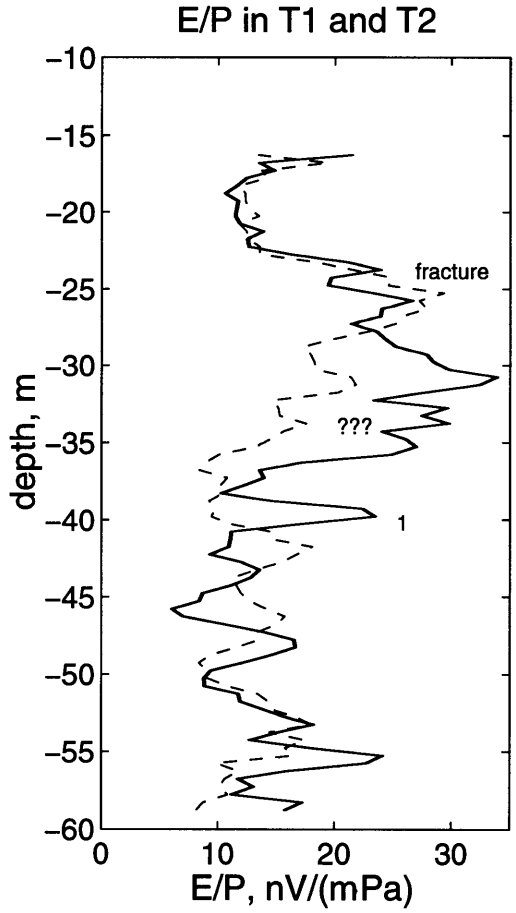

Figure 2-31: Comparison between the normalized electroseismic amplitudes measured in boreholes T1 (solid line) and T2 (dashed line). The normalized electroseismic amplitudes in both boreholes agree below the depth of $40m$ and above the depth of $23m$. Also, the normalized electroseismic amplitudes agree at the depth of the isolated fracture. In the depth interval between $28m$ and $32m$ there is a mismatch between the measurements in boreholes T1 and T2.

Chapter 3

Theoretical model for the Stoneley-wave-induced electrical field

In Chapter 2, we investigated experimentally electrical fields induced by borehole Stoneley waves. We presented field measurements of these electrical fields and demonstrated that they were induced by pore fluid flow in the formation around the borehole. The goal of this chapter is to determine what specific properties of a rock formation can be deduced from borehole electroseismic measurements. We develop a theoretical model for the Stoneley-wave-induced electrical fields. According to this theoretical model, the normalized amplitude of the Stoneley-wave-induced electrical field is proportional to the porosity and inversely proportional to the pore space tortuosity of a formation around a borehole. Moreover, the amplitude-versus-frequency behavior of this electrical field depends on the permeability of the formation.

3.1 Stoneley-wave-induced electrical field in a homogeneous, porous, permeable formation

In this section we develop a theoretical model for an electrical field induced by Stoneley-wave-generated fluid flow within a permeable formation. Using this model we obtain an analytical solution for the normalized amplitude of this electrical field. Our theoretical model is based on the Biot theory (Biot, 1962). The applicability of the Biot theory to the problem of Stoneley wave propagation along a borehole in a fractured formation was argued by Tang and Cheng (1993) and by Kostek *et al.* (1998).

3.1.1 Pressure distribution in the borehole and in the formation around the borehole created by the Stoneley wave

A Stoneley wave of angular frequency ω, propagating with a phase velocity $c_s(\omega)$ down a borehole in a homogeneous, permeable formation, induces oscillations of fluid pressure P_b in the borehole (Tang *et al.*, 1991):

$$P_b(r,z,t) = P_0 \frac{I_0\left(r\frac{\omega}{c_s}\right)}{I_0\left(R_b\frac{\omega}{c_s}\right)} \exp\left(-i\omega t + i\frac{\omega}{c_s}z\right). \tag{3.1}$$

Here, r and z are the cylindrical coordinates (z-axis is pointing down), t is time, R_b is the borehole radius, and P_0 is the scalar amplitude of the pressure oscillation. The Stoneley wave phase velocity $c_s(\omega)$ is, in general, a complex number, thus accommodating attenuation.

The pore pressure oscillation created in the formation by the Stoneley wave is

(Tang *et al.*, 1991)

$$P_f(r,z,t) = P_0 \frac{K_0\left(r\sqrt{-\frac{i\omega}{D}+\left[\frac{\omega}{c_s}\right]^2}\right)}{K_0\left(R_b\sqrt{-\frac{i\omega}{D}+\left[\frac{\omega}{c_s}\right]^2}\right)} \exp\left(-i\omega t + i\frac{\omega}{c_s}z\right). \tag{3.2}$$

Here, D is the pore fluid dynamic diffusivity defined by Tang *et al.* (1991). In Equations 3.1 and 3.2, I_0 and K_0 are the zero-order modified Bessel functions.

3.1.2 Streaming and conducting electrical currents induced by pore fluid flow in the formation

The pore pressure gradient, induced in the formation by the Stoneley wave, causes a flow of pore fluid. Since the pore fluid is electrically charged, the flow results in a streaming electrical current. The streaming electrical current creates a charge separation that induces an electrical field (Figure 2-1). In turn, this electrical field drives a conductive electrical current in the formation. Thus, the total electrical current density in the formation is the sum of the conductive current and streaming current densities:

$$\underline{j}_{total} = \underline{j}_{conductive} + \underline{j}_{streaming} = \sigma_r \underline{E} - L\nabla P_f. \tag{3.3}$$

Here, $\underline{E}$ is the electrical field vector, σ_r is the formation conductivity, and L is the streaming current coupling coefficient derived by Pride (1994):

$$L = -\frac{\phi}{\alpha_\infty}\frac{\zeta\epsilon_f}{\mu}\left(1 - \frac{i\omega}{\omega_c}\frac{4}{M^2}\right)^{-\frac{1}{2}}. \tag{3.4}$$

Here, ϕ is the porosity, α_∞ is the pore space tortuosity, ζ is the zeta-potential (determined by the electrochemical interaction between the pore fluid and the rock), ϵ_f is the pore fluid permittivity, μ is the pore fluid viscosity, and ω_c is the Biot critical frequency for the formation. The Biot theory defines ω_c as the frequency which separates

the viscosity-dominated flow regime from the inertia-dominated flow regime. Equation 3.4 states that for the viscosity-dominated flow regime ($\omega << \omega_c$) the coupling coefficient does not change with frequency and for the inertia-dominated flow regime ($\omega >> \omega_c$) the coupling coefficient decreases as $\omega^{-\frac{1}{2}}$. The Biot critical frequency for the formation is (Johnson *et al.*, 1987)

$$\omega_c = \frac{\phi\mu}{\alpha_\infty \rho_f k_0} \cdot \frac{2}{M}. \tag{3.5}$$

Here, k_0 is the formation permeability, ρ_f is the pore fluid density, and M is a pore-geometry-dependent dimensionless parameter that is close to 1 for most media (Johnson *et al.*, 1987).

3.1.3 The analytical solution for the amplitude of the electrical field induced by the Stoneley wave

The combination of Equations 3.2, 3.3 and 3.4 leads to an analytical solution for the ratio of the vertical component of the electrical field in the borehole, E_z, to the pressure oscillation in the borehole, P_b:

$$\frac{E_z}{P_b} = \left(\frac{i\omega}{c_s}\right)\left\{-\frac{\phi}{\alpha_\infty}\frac{\zeta\epsilon_f}{\sigma_r\mu}\left(1-\frac{i\omega}{\omega_c}\frac{4}{M^2}\right)^{-\frac{1}{2}}\right\}\left[1+\frac{\sigma_f}{\sigma_r}\frac{I_1\left(R_b\frac{\omega}{c_s}\right)}{I_0\left(R_b\frac{\omega}{c_s}\right)}\frac{K_0\left(R_b\frac{\omega}{c_s}\right)}{K_1\left(R_b\frac{\omega}{c_s}\right)}\right]^{-1}. \tag{3.6}$$

Here, σ_f is the borehole fluid conductivity. Details of the derivation of Equation 3.6 are given in Appendix B. Equation 3.6 describes the normalized amplitude and phase of the electrical field induced by the Stoneley-wave-generated fluid flow within a permeable formation.

3.1.4 Comparison of the amplitudes predicted by the theoretical model to the amplitudes measured in granite

To check the consistency of the theoretical model with the experimental results, we compare the amplitudes of the Stoneley-wave-induced electrical fields predicted by Equation 3.6 and the amplitudes measured in the field. It is possible to make this comparison for the granite section of the Hamilton well (upper $137m$) because all the parameters in Equation 3.6 (including the zeta-potential, ζ) are known for granite from independent field and laboratory measurements.

Table 3.1 shows the values for the parameters in Equation 3.6 that we use for the amplitude comparison in granite. The Stoneley wave angular frequency, ω, and velocity, c_s, are determined from the hydrophone measurements (Figure 2-5). In the experiment, as the Stoneley wave propagated down the borehole, its amplitude decreased mostly due to backscattering of the wave by fractures and washout zones. Thus, for the first-order analysis, we neglect the attenuation and consider c_s to be real-valued and equal to the apparent phase velocity of the Stoneley wave. The borehole diameter, R_b, is determined from the caliper log (Figure 2-3). The value of the borehole fluid conductivity, σ_f, corresponds to the salinity of $0.004mol/l$ of NaCl measured for a sample of the actual borehole fluid (water). The values of the fluid viscosity, μ, and permittivity, ϵ_f, are the values for water. For granite and water with salinity of $0.004mol/l$ of NaCl and conductivity of $0.022S/m$, the value of the zeta-potential, ζ, has been measured in laboratory experiments (Morgan *et al.*, 1989). In experiments with a natural fracture, Brown et al. (1998) found fracture tortuosity, α_∞, to be close to 1 due to channeling. Thus, in our calculations we assume the tortuosity of fractures, α_∞, to be 1.0. In addition to the parameters in Table 3.1, we substitute into Equation 3.6 the value of $0.012S/m$ for the rock conductivity, σ_r. This value is the average measured in the granite section (Figure 2-3). For the porosity,

ϕ, of fractured granite we substitute the value of 0.5% (Nur, 1969; Hadley, 1976; Toksöz *et al.*, 1976). Further, we assume that the Stoneley wave frequency in the experiment is less than the Biot critical frequency, ω_c, for the fractured formation. This assumption is equivalent to postulating that the permeability of the formation, k_0, was less than $10^{-11}m^2$ or $10Darcy$ (Equation 3.5).

Substitution of the values in Table 3.1 and the above values for rock conductivity and porosity into Equation 3.6 gives the value of the E/P ratio of $12nV/(m \cdot Pa)$. Figure 2-8 shows that the values of the E/P ratio observed in the granite section are between $5nV/(m \cdot Pa)$ and $20nV/(m \cdot Pa)$. Thus, the predictions of Equation 3.6 agree with the values for the normalized amplitude of the electrical field measured in the field. This result shows that the theoretical model is consistent with the results of the field experiments.

3.1.5 Consistency of the theoretical model with the field measurements in dolomite

We cannot make a direct comparison between the amplitudes predicted by the theoretical model and the amplitudes measured in the dolomite formation because the exact value of the zeta-potential for the dolomite is not available. Berlin and Khabakov (1961) demonstrated that in organic dolomite and fresh water, the values of the zeta-potential varied from $-0.6mV$ to $-4.45mV$ [1]. In organic dolomite and water with $0.01mol/l$ KCl, the values of the zeta-potential varied from $-2.9mV$ to $-12mV$ [2].

[1] In addition to these results, Berlin and Khabakov (1961) demonstrated that in the dolomite of the chemical origin, the zeta-potential is positive, and in the dolomite of sedimentary (organic) origin, the zeta-potential is negative.

[2] The fact that the zeta-potential measured in salted water was higher than that measured in fresh water and the significant spread of the zeta-potential values make us question the validity of the results of Berlin and Khabakov (1961). However, their data is the only data available for comparison.

Moreover, Berlin and Khabakov (1961) demonstrated that presence of clays or silica significantly changes the values of the zeta-potential in carbonate rocks.

Even though we cannot make a direct amplitude comparison, we can still check the consistency of the theoretical model with the field data in dolomite. Since we know the porosity values from neutron and sonic logs, we can use our theoretical model to derive the zeta-potential value for the dolomite at the Belvidere site. Equation 3.6 can be used to deduce the absolute value of the zeta-potential from the field data:

$$\zeta = \left|\frac{E_z}{P_b}\right| \frac{\alpha_\infty \sigma_r \mu}{\phi \epsilon_f} \frac{c_s}{\omega} \left(1 + \frac{\sigma_f}{\sigma_r} \frac{I_1\left(R_b \frac{\omega}{c_s}\right)}{I_0\left(R_b \frac{\omega}{c_s}\right)} \frac{K_0\left(R_b \frac{\omega}{c_s}\right)}{K_1\left(R_b \frac{\omega}{c_s}\right)}\right). \tag{3.7}$$

From independent field measurements we know the values for all the parameters in Equation 3.7 except for tortuosity, α_∞. These values are summarized in Table 3.2. The pore space tortuosity, α_∞, is usually assumed to vary between 3 and 10 (Haartsen, 1995). If we substitute the values from Table 3.2 into Equation 3.7 and assume the pore space tortuosity value of 3, then Equation 3.7 yields $|\zeta| = 0.75mV$. If we assume the pore space tortuosity value of 10, then Equation 3.7 yields $|\zeta| = 2.5mV$. These values of the zeta-potential agree with the results of the laboratory experiments of Berlin and Khabakov (1961). Therefore, the values of the normalized electroseismic amplitudes measured in dolomite agree with the values predicted by the theoretical model.

3.2 Determining porosity from the normalized amplitude of the Stoneley-wave-induced electrical fields at low frequencies

Equation 3.6 states that the normalized amplitude of the Stoneley-wave-induced electrical field is proportional to the porosity. This theoretical result is consistent with the field measurements in dolomite. A direct comparison between the normalized amplitude of the Stoneley-wave-induced electrical fields and the porosity logs in boreholes T6 and T7 demonstrated that the normalized electroseismic amplitude correlates with the porosity.

Using the theoretical model, we can derive an equation for determining porosity from borehole electroseismic measurements:

$$\phi = \left|\frac{E_z}{P_b}\right| \frac{\alpha_\infty \sigma_r \mu}{|\zeta|\epsilon_f} \frac{c_s}{\omega} \left(1 + \frac{\sigma_f}{\sigma_r} \frac{I_1\left(R_b \frac{\omega}{c_s}\right)}{I_0\left(R_b \frac{\omega}{c_s}\right)} \frac{K_0\left(R_b \frac{\omega}{c_s}\right)}{K_1\left(R_b \frac{\omega}{c_s}\right)}\right). \tag{3.8}$$

Here, we assume that the wave frequency, ω, in the experiment is less than the Biot critical frequency, ω_c, for the formation. Equation 3.8 states that porosity can be deduced from the electroseismic measurements provided that all the necessary parameters of the formation, including the zeta-potential, ζ, are known.

3.2.1 Deriving a porosity log for granite from the electroseismic field data

We can use Equation 3.8 to derive a porosity log for the granite section in the Hamilton well from electroseismic measurements. It is possible to derive the porosity log for this granite section because all the parameters in Equation 3.8 (including the

zeta-potential, ζ) are known for granite from independent field and laboratory measurements. Figure 3-1 illustrates this derivation. At each depth we substitute the E/P ratio (the first plot in Figure 3-1), the formation conductivity, σ_r (the second plot in Figure 3-1) and other parameters given in Table 3.1 into Equation 3.8 to obtain a porosity estimate at that depth. The third plot in Figure 3-1 shows the resulting porosity log for the granite section.

In the subsurface at Hamilton, the granite matrix has no porosity (GEOSS, 1984a,b). All the porosity of the granite formation is due to fractures. Thus, the porosity log in Figure 3-1 represents the value of the fracture porosity averaged over the Stoneley wavelength ($9.3m$ in the experiment). We do not have any other porosity measurement for granite to verify the porosity log. However, we can compare our porosity estimate to the fracture density log derived from the borehole video (the fourth plot in Figure 3-1). A comparison shows that the electroseismic porosity estimate correlates with the averaged fracture density (as does the normalized amplitude of the Stoneley-wave-induced electrical field).

The values for fracture porosity estimated using Equation 3.8 are reasonable for fractured granite (Nur, 1969; Hadley, 1976; Toksöz *et al.*, 1976). However, in order to be confident about the exact values of the porosity, it is necessary to know the exact values of the parameters like zeta-potential, ζ, and tortuosity, α_∞, for the formation of interest. For example, to derive the porosity log, we used the value for zeta-potential measured in a laboratory experiment (Morgan *et al.*, 1989) for granite and water with the salinity of the water in the borehole. It is possible that the salinity of fluid within fractures is different from the salinity of the borehole water. In this case, the zeta-potential value is different from the one assumed in our calculation. Nevertheless, Figure 3-1 suggests that our porosity estimate has the correct variation with depth, because it correlates with the fracture density log.

3.3 High amplitude anomaly at the isolated fracture in dolomite: the tortuosity effect

Equation 3.6 states that the normalized amplitude of the Stoneley-wave-induced electrical field is inversely proportional to the pore space tortuosity. This result can explain the anomalously high amplitude of the Stoneley-wave-induced electrical field at an isolated fracture in dolomite.

Prior to discussing the experimental results, we would like to explain briefly the physical meaning of pore space tortuosity. In this thesis we use the definition of pore space tortuosity that was given by Johnson *et al.* (1987) and that was later adopted by Pride (1994). Johnson *et al.* (1987) introduced tortuosity through the relationship between the acceleration of the pore fluid and the pressure gradient in the fluid at high frequencies or at zero fluid viscosity:

$$\alpha_\infty \rho_f \frac{\partial^2 \underline{U}_f}{\partial t^2} = -\nabla P. \tag{3.9}$$

Here, $\underline{U}_f$ is the averaged fluid displacement. Defined in this way, the tortuosity also enters the expression for the force that is exerted by the acceleration of the solid frame upon the fluid in the pores. The Biot equation that describes acceleration of the fluid can be rewritten as (Johnson *et al.*, 1987):

$$\phi \rho_f \frac{\partial^2 \underline{U}_f}{\partial t^2} = (\alpha_\infty - 1)\phi \rho_f \left(\frac{\partial^2 \underline{u}_s}{\partial t^2} - \frac{\partial^2 \underline{U}_f}{\partial t^2} \right) + (other forces). \tag{3.10}$$

Here, $\underline{u}_s$ is the averaged solid displacement.

If an added mass coefficient is defined as the ratio of the fluid volume that is accelerated with the solid in the absence of other forces on the fluid,

$$A = \frac{\frac{\partial^2 \underline{U}_f}{\partial t^2}}{\frac{\partial^2 \underline{u}_s}{\partial t^2}}, \tag{3.11}$$

then a straightforward manipulation of Equation 3.10 yields:

$$A = \frac{\alpha_\infty - 1}{\alpha_\infty}. \tag{3.12}$$

The added mass coefficient defined by Equation 3.11 has a simple physical meaning. Suppose a porous rock is saturated with an inviscous fluid. If the rock is moved, some of the inviscous fluid will move with it and some will stay in place. The added mass coefficient describes the fraction of the fluid that will move with the rock. Using this physical description, we can determine the limiting values of the added mass coefficient, A, and the pore space tortuosity, α_∞:

1. If pore space in the rock consists of plane-parallel fractures aligned in one direction, then it is possible to move the rock along this direction without disturbing the inviscous fluid in the fractures. In this situation, the added mass coefficient, A, is zero [3]. According to Equation 3.12, the pore space tortuosity for this case is $\alpha_\infty = 1$.

2. If the pore space in the rock consists of straight capillaries aligned in three mutually perpendicular directions, then the added mass coefficient, A, equals $\frac{2}{3}$ because the rock motion in any of these three directions will move along the fluid in the pipes that are perpendicular to the motion. This situation is the simpliest model for an isotropic rock. According to Equation 3.12, the pore space tortuosity for this case is $\alpha_\infty = 3$.

3. If the pore space in the rock is sealed, i.e., all the fluid moves along with the rock, then the added mass coefficient, A, is equal to 1. According to Equation 3.12, the pore space tortuosity, α_∞, is infinite.

The analysis presented above suggests that tortuosity of fractures can be close to

[3]... in this direction. This situation clearly demonstrates that the added mass coefficient is a tensor quantity. We are not going to discuss the added mass coefficient in more detail because its mathematical definition can be found in any rigorous monograph on hydrodynamics, such as the one by Landau and Lifshitz (1959).

1. This result is confirmed by laboratory measurements in a natural fracture (Brown *et al.*, 1998). Further, this analysis suggests that in an isotropic porous medium, the pore space tortuosity is at least 3. Moreover, it can be much higher than 3, if the pore space consists of large pores connected by thin throats (as is the case in vuggy dolomite). It is usually assumed in numerical modeling that in isotropic porous media the values of pore space tortuosity range from 3 to 10. Note that these values were used for non-fractured dolomite earlier in this Chapter.

Using the analysis presented above, we can explain the anomalously high amplitudes of the Stoneley-wave-induced electrical fields at the isolated fracture that intersected boreholes T1 and T2. According to the theoretical model, the normalized electroseismic amplitude is inversely proportional to the tortuosity, α_∞. Tortuosity of natural fractures are close to 1 (Brown *et al.*, 1998). In the non-fractured dolomite, the tortuosity is at least 3 and can be significantly higher. Thus, even though the fracture does not necessarily contribute to the total porosity, the normalized electroseismic amplitudes at the fracture are higher because its tortuosity is lower than in non-fractured dolomite.

3.4 Determining permeability from the amplitude-versus-frequency behavior of the Stoneley-wave-induced electrical potential

In this section we analyze the amplitude-versus-frequency dependence of the Stoneley-wave-induced electrical potential predicted by the theoretical model. We demonstrate that, according to Pride's (1994) model, permeability of the formation, k_0, can be determined from this amplitude-versus-frequency dependence.

Starting from this point in the thesis, it will be more convenient to work with the electrical potential, Φ_b, induced by the Stoneley wave in the borehole, rather than with the electrical field, E_z. This is purely a matter of choice, because the electrical potential, Φ_b, and the electrical field, E_z, are related to each other as $E_z = -\frac{\partial \Phi_b}{\partial z}$, or in the frequency domain, $E_z(\omega) = \Phi_b(\omega) \cdot \left(-\frac{i\omega}{c_s}\right)$.

According to the theoretical model, the ratio of the electrical potential oscillation, Φ_b, to the pressure oscillation in the borehole, P_b, is:

$$\frac{\Phi_b}{P_b}(\omega) = \left\{ \frac{\phi_{ic}}{\alpha_\infty} \frac{\zeta \epsilon_f}{\sigma_r \mu} \left(1 - \frac{i\omega}{\omega_c} \frac{4}{M^2}\right)^{-\frac{1}{2}} \right\} \cdot \left[1 + \frac{\sigma_f}{\sigma_r} \frac{I_1\left(R_b \frac{\omega}{c_s}\right)}{I_0\left(R_b \frac{\omega}{c_s}\right)} \frac{K_0\left(R_b \frac{\omega}{c_s}\right)}{K_1\left(R_b \frac{\omega}{c_s}\right)} \right]^{-1} . \quad (3.13)$$

The expression for the normalized amplitude of the Stoneley-wave-induced electrical potential (Equation 3.13) is a product of two terms. The first term (curly brackets) is the frequency-dependent electroseismic coupling coefficient for the rock formation. The second term (square brackets) can be viewed as a "correction for the geometry of the experiment." Below, we analyze these two terms separately. We show how, according to Pride's (1994) theory, permeability, k_0, can be determined from the amplitude-versus-frequency dependence of the electroseismic coupling coefficient. Further, we demonstrate how the the ratio of the fluid conductivity to the formation conductivity, $\frac{\sigma_f}{\sigma_r}$, modifies the amplitude-versus-frequency dependence of the Stoneley-wave-induced electrical potential.

3.4.1 Permeability dependence of the electroseismic coupling coefficient for the rock formation

Permeability enters Equation 3.13 through the amplitude-versus-frequency dependence of the electroseismic coupling coefficient for the rock formation (Pride, 1994). Specifically, permeability is related to the Biot critical frequency, ω_c (Equation 3.5).

Below, we show how permeability of the formation can be estimated from measurements of the Stoneley-wave-induced electrical potential.

The first term in Equation 3.13 is the electroseismic coupling coefficient for the rock formation, C_{elsm}:

$$C_{elsm} = \frac{\phi_{ic}}{\alpha_\infty} \frac{\zeta \epsilon_f}{\mu \sigma_r} \left(1 - \frac{i\omega}{\omega_c} \frac{4}{M^2}\right)^{-\frac{1}{2}}. \tag{3.14}$$

The electroseismic coupling coefficient, C_{elsm}, is the amplitude of an electrical potential oscillation created in an homogeneous medium by a pore pressure oscillation of a unit amplitude and frequency ω. This coefficient can be derived from Pride and Haartsen's (1996) solutions for plain longitudinal electroseismic waves. In the low frequency limit ($\omega << \omega_c$), the electroseismic coupling coefficient, C_{elsm}, is equal to the Helmholtz-Smoluchovski's coupling coefficient for DC streaming potential. The frequency dependence of the electroseismic coupling coefficient, C_{elsm}, is derived by Pride (1994).

The second term in Equation 3.13 can be viewed as a "correction for the geometry of the experiment." If the rock conductivity, σ_r, the borehole fluid conductivity, σ_f, the borehole radius, R_b, and the Stoneley wave velocity, $c_s(\omega)$, are known, then the second term can be calculated at each frequency. In turn, the electroseismic coupling coefficient as a function of frequency, $C_{elsm}(\omega)$, can be derived from the $\frac{\Phi_b}{P_b}(\omega)$ data:

$$C_{elsm}(\omega) = \left(\frac{\Phi_b}{P_b}(\omega)\right) \left[1 + \frac{\sigma_f}{\sigma_r} \frac{I_1\left(R_b \frac{\omega}{c_s}\right)}{I_0\left(R_b \frac{\omega}{c_s}\right)} \frac{K_0\left(R_b \frac{\omega}{c_s}\right)}{K_1\left(R_b \frac{\omega}{c_s}\right)}\right]. \tag{3.15}$$

Pride's (1994) theory suggests that permeability can be derived from the frequency dependence of the electroseismic coupling coefficient, $C_{elsm}(\omega)$. Equation 3.14 states that at frequencies below the Biot critical frequency ($\omega << \omega_c$), the coefficient C_{elsm} is constant, and above Biot critical frequency ($\omega >> \omega_c$), C_{elsm} decreases as $\omega^{-\frac{1}{2}}$. Figure 3-2 shows a plot of the electroseismic coupling coefficient, C_{elsm}, as a function

of frequency calculated using Equation 3.14. In this calculation we used the properties of the formation and the borehole fluid in the experiment (Table 3.1), a porosity value of 0.5%, a rock conductivity value of $0.012 S/m$ and a permeability value of $1.6 \cdot 10^{-12} m^2$ or $1.6 Darcy$. The Biot critical frequency for such a formation is $\omega_c = 2\pi \cdot 1000 Hz$ (Equation 3.5) [4]. Suppose the electroseismic experiments are made over a wide frequency range and Biot critical frequency, ω_c, is determined from the change of the amplitude-versus-frequency dependence of the Stoneley-wave-induced electrical potentials. Then, permeability, k_0, of the formation can be estimated from the Biot critical frequency, ω_c, using Equation 3.5:

$$k_0 = \frac{\phi_{ic} \mu}{\omega_c \alpha_\infty \rho_f} \cdot \frac{2}{M}. \tag{3.16}$$

The theoretical model's implication that permeability can be determined from the borehole electroseismic measurements is exciting. However, the practical significance of this result depends on the validity of the theoretical model, specifically on whether Pride's theory (1994) correctly describes the physics of streaming electrical currents and whether the Biot theory correctly describes seismic-wave-generated fluid flow in real rocks. The goal of the next chapter of this thesis is to compare the amplitude-versus-frequency dependence of the real electroseismic signals recorded in the field with the prediction of the theoretical model in order to test the model's validity, and to determine whether permeability indeed can be derived from borehole electroseismic measurements.

[4] Hereafter in this section we will make calculations for granite at the Hamilton site. In Chapter 4 we will investigate experimentally the amplitude-versus-frequency dependence of the Stoneley-wave-induced electrical fields in granite at the Hamilton site.

3.4.2 Modification of electrical potential amplitude by the borehole presence: $\frac{\sigma_f}{\sigma_r}$ effect

The second term (square brackets) in Equation 3.13 describes the modification of the amplitude of the Stoneley-wave-induced electrical potential by the borehole presence. We like to think of this term as a "correction for the geometry of the experiment" because it has a simple geometrical meaning that can be explained using the diagram in Figure 2-1.

Figure 2-1 shows the pressure gradient created by the Stoneley wave driving a flow of pore fluid in the formation. Since the fluid carries an excess electrical charge (positive in the experiment), this fluid flow results in an accumulation of a positive electrical charge in the zone of extension and of a negative electrical charge in the zone of compression. This electrical charge separation induces an electrical field in the formation and in the borehole. In turn, this electrical field drives a return conductive electrical current that balances the streaming electrical current. This conductive electrical current flows through the rock formation and through the borehole. The second term in Equation 3.13 describes how the return conductive electrical current is partitioned between the borehole and the formation. Specifically, the second term in the square brackets is the ratio of the conductances of the two return paths for the conductive electrical current: the return path through the borehole and the return path through the formation.

At very low frequencies, when the Stoneley wave length is much longer than the borehole radius, all the return conductive electrical current is flowing through the rock formation. At these frequencies the normalized amplitude of the Stoneley-wave-induced electrical potential $\frac{\Phi_b}{P_b}(\omega)$ is equal to the electroseismic coupling coefficient, C_{elsm} (i.e., the borehole presence is negligible). As the frequency increases, the return path through the borehole becomes more and more "attractive" for the

conductive electrical current because the Stoneley wavelength decreases and the area of the return path through the rock decreases as the wavelength squared. At these frequencies the amplitude of the Stoneley-wave-induced electrical potential decreases as ω^{-2}. Finally, when the Stoneley wavelength becomes less than the borehole radius, both streaming and conductive electrical currents flow in a very thin zone in the vicinity of the borehole wall, and the return conductive electrical current becomes partitioned between the formation and the borehole fluid according to the ratio of their conductivities.

Figure 3-3 shows synthetic amplitude-versus-frequency curves for the Stoneley-wave-induced electrical potential (Equation 3.13) calculated for different ratios of fluid conductivity to rock conductivity, $\frac{\sigma_f}{\sigma_r}$, and a fixed value of the zeta-potential, ζ (that in reality depends on the fluid conductivity σ_f). To calculate these curves we used the same values of all the other parameters in Equation 3.13, as we used to calculate the $C_{elsm}(\omega)$ curve in Figure 3-2, except for the formation permeability, k_0, for which we used the value of $1.6 \cdot 10^{-15} m^2$ or $1.6 mDarcy$. The Biot critical frequency for such a formation ($k_0 = 1.6 \cdot 10^{-15} m^2$, $\phi = 0.5\%$) is $\omega_c = 2\pi \cdot 1 MHz$ (Equation 3.5). It is much higher than the frequency range in Figure 3-3. Thus, in this frequency range the electroseismic coupling coefficient, $C_{elsm}(\omega)$, is constant. The synthetic curves in Figure 3-3 show that the higher the conductivity of the fluid, the lower the frequency at which the return conductive electrical current starts flowing through the borehole. Thus, the more conductive the borehole fluid, the less the amplitude of the Stoneley-wave-induced electrical potential.

3.5 Relationship between the amplitude of the Stoneley-wave-induced electrical field and the lithology

In the Hamilton experiment, the P-wave slowness and the fracture density logs in Figure 2-3 show that both the granite section (upper $137m$) and the diorite section ($177m$-$280m$) of the well have fractured zones and isolated large fractures. At the same time, Figure 2-8 shows that in the granite section the Stoneley-wave-induced electrical fields have normalized amplitudes of up to $20nV/(m \cdot Pa)$ while in the diorite section the normalized amplitude is around $3nV/(m \cdot Pa)$. This difference in the electroseismic signals' amplitudes can be explained by the difference in the electrochemical interaction of the pore fluid (water) with granite and diorite. The term in Equation 3.6 which describes this interaction is the zeta-potential. The exact definition of the zeta-potential is the electrical potential at the "hydrodynamic slipping plane," i.e., the closest plane to the rock surface on which fluid can move (Morgan *et al.*, 1989). The higher the absolute value of the zeta-potential, the more electrical charge can be moved by fluid flow. The value of the zeta-potential for granite and the borehole fluid (NaCl concentration of $0.004mol/l$) is $\zeta = -60mV$. The values for the zeta-potential of diorite are not available in the literature for comparison. However, we can hypothesize that since diorite does not contain quartz, while granite does, the absolute amplitude of the zeta-potential in diorite is lower than the zeta-potential in granite. Thus, even though the Stoneley wave induces pore fluid flow within fractures in diorite, this flow induces weaker electrical field than it does in granite.

In the Belvidere experiment, the normalized amplitude of the Stoneley-wave-induced electrical fields correlated with the porosity of the dolomite formation. However,

there were numerous mismatches between the porosity and the normalized electroseismic amplitudes (Figures 2-24, 2-30). Some of these discrepancies could be attributed to changes in lithological composition. An example of such discrepancy due to lithology is the zone above the depth of $25m$ in borehole T6. In this zone the normalized electroseismic amplitude deviates towards lower values from the neutron porosity log. At the same time, the sonic porosity log deviates towards higher values. Overall, the results of the borehole electroseismic experiments in dolomite demonstrated that interpretation of the electroseismic field data can be challenging in formations with varying lithological composition.

The fact that the electroseismic coupling is different in different lithologies is important for accessing the practical use of the electroseismic measurements. Examples described above demonstrate it is necessary to know the the zeta-potential, ζ, for the specific rock type, prior to extracting porosity or permeability information from electroseismic measurements. Laboratory experiments of Berlin and Khabakov (1961) demonstrated that presence of shales or silica in carbonate rocks can significantly change their zeta-potential. Moreover, for the same lithology, the zeta-potential depends on the type of the pore fluid. For example, a laboratory study of Mironov et al. (1993) shows that in sandstone saturated with a mixture of water and kerosene, the higher the fraction of kerosene in mixture, the lower the amplitude of the electroseismic signals. Thus, measurements of the zeta-potential for different rock types and for different pore fluids are necessary prior to using electroseismic measurements in practice.

3.6 Conclusion

In this Chapter we developed a Biot-theory-based model for the Stoneley-wave-induced electrical fields. The amplitudes of these electrical fields predicted by the theoretical model agreed with the amplitudes measured in the experiments. Using this theoretical model we were able to explain the main results of the borehole electroseismic experiments that were described in Chapter 1.

The theoretical model suggests that the normalized amplitude of the Stoneley-wave-induced electrical fields is proportional to the porosity of a formation around a borehole. In the dolomite experiment, the normalized amplitudes of the Stoneley-wave-induced electrical fields correlated with porosity logs. Thus, the theoretical model is consistent with the results of field experiments. Based on these results, we concluded that in the Hamilton experiment the normalized electroseismic amplitude was sensitive to fracture porosity averaged over the Stoneley wavelength. We used the theoretical model to derive a fracture porosity log for the granite section. This derivation yielded reasonable values for fracture porosity in granite, and the porosity log correlated with the fracture density log.

The theoretical model also predicts that the normalized amplitude of the Stoneley-wave-induced electrical field is inversely proportional to the pore space tortuosity. This result explains the anomalously high amplitudes of the Stoneley-wave-induced electrical fields at the isolated fracture that intersects boreholes T1 and T2. Fracture tortuosity is close to 1 (Brown *et al.*, 1998). At the same time, in an isotropic porous formation the tortuosity is at least 3. Moreover, in a formation with large pores connected with narrow throats, tortuosity can much higher. Thus, a Stoneley wave generates stronger electrical fields at a fracture than in an isotropic porous formation.

Further, the theoretical model predicted that the normalized amplitudes of the

Stoneley-wave-induced electrical fields are proportional to the zeta-potential. Therefore, the normalized electroseismic amplitudes are sensitive to lithology and the fluid type. This result can explain why in the Hamilton experiment we measured much higher normalized electroseismic amplitude in granite than in diorite. Also, this result can explain mismatches between the porosity logs and the normalized electroseismic amplitudes in dolomite.

Finally, the theoretical model predicts that the amplitude-versus-frequency dependence of the Stoneley-wave-induced electrical fields depends on the permeability. This prediction is quite exciting and in Chapter 4 we will present field measurements of this amplitude-versus-frequency dependence in the frequency range from $100Hz$ to $4kHz$. These measurements will allow us to test further the validity of the theoretical model described in this Chapter.

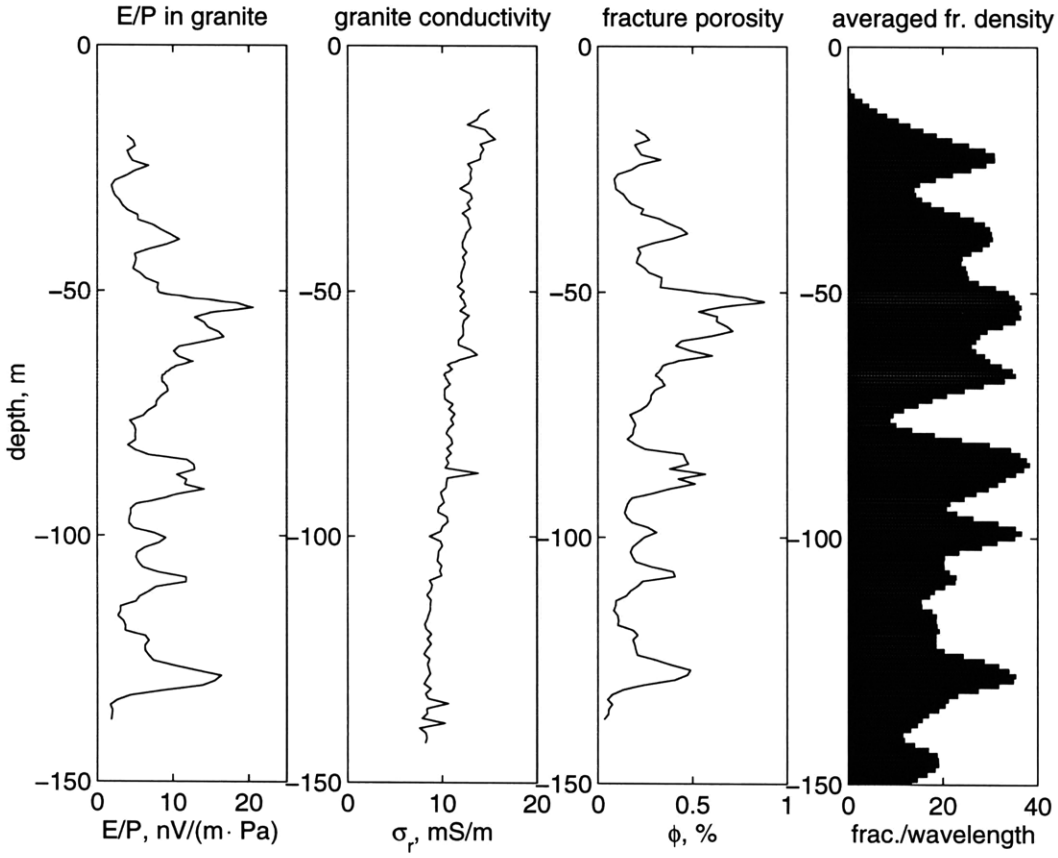

Figure 3-1: Derivation of a porosity log for the granite section from our electroseismic measurements. At each depth we substitute the E/P ratio (the first plot), the formation conductivity, σ_r (the second plot), and other parameters given in Table 3.1 into Equation 3.8 to obtain a porosity estimate at that depth (the third plot). This porosity log represents the value of the fracture porosity averaged over the Stoneley wavelength ($9.3m$ in our experiment). This porosity estimate correlates with the averaged fracture density in granite (the fourth plot).

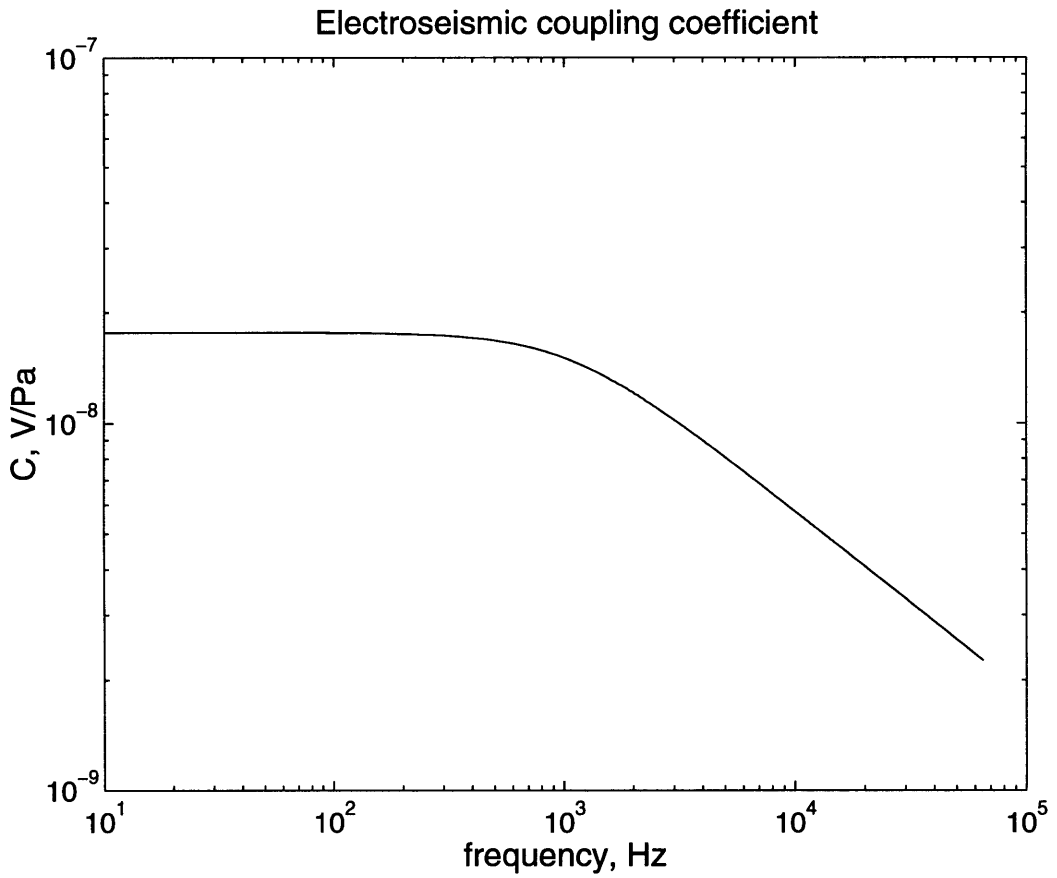

Figure 3-2: Electroseismic coupling coefficient C_{elsm} as a function of frequency calculated using Equation 3.14. In the calculation we used properties of the formation and the borehole fluid in the experiment (Table 3.1), a porosity value of 0.5%, a rock conductivity value of $0.012 S/m$ and a permeability value of $1.6 \cdot 10^{-12} m^2$ or $1.6 Darcy$. The Biot critical frequency for such a formation is $\omega_c = 2\pi \cdot 10^3 Hz$. Below the $10^3 Hz$ frequency the electroseismic coupling coefficient C_{elsm} is constant, and above $10^3 Hz$ it decreases as $\omega^{-\frac{1}{2}}$.

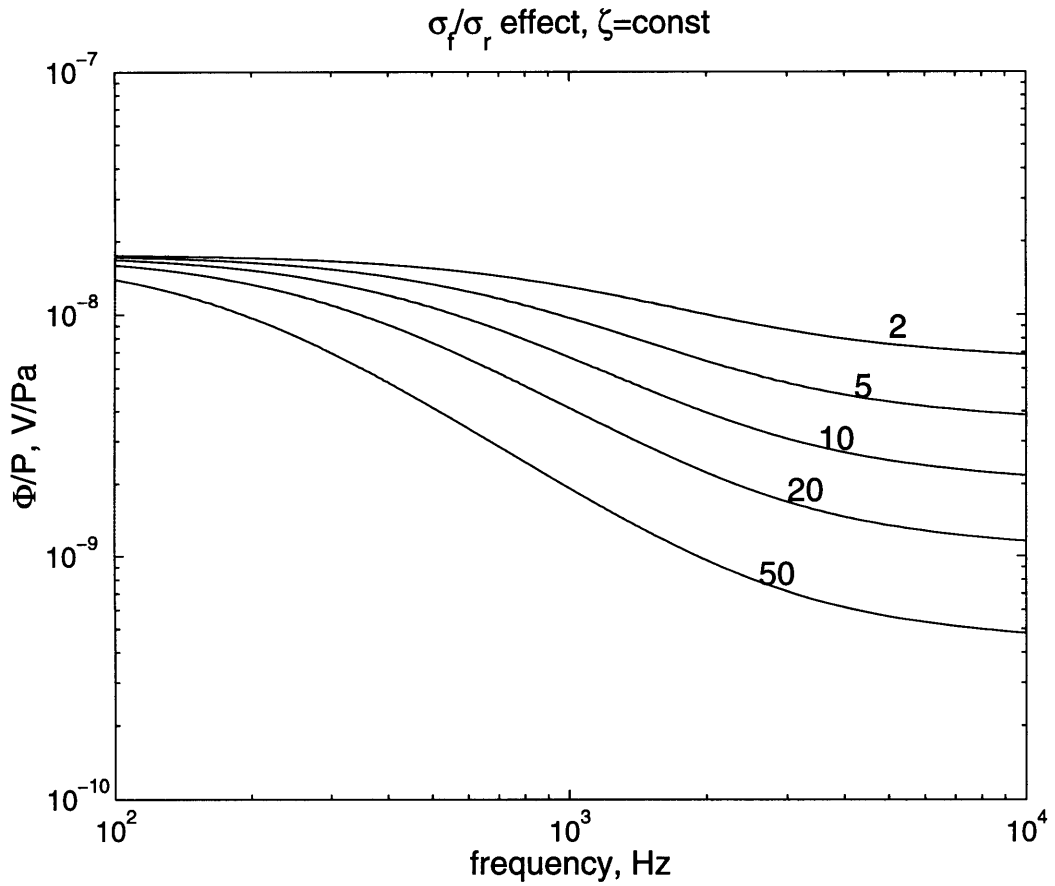

Figure 3-3: Synthetic amplitude-versus-frequency curves for the Stoneley-wave-induced electrical potential (Equation 3.13) calculated for different ratios of fluid conductivity to rock conductivity, $\frac{\sigma_f}{\sigma_r}$, and a fixed value of the zeta-potential $\zeta = -60mV$. In reality, the zeta-potential depends on the fluid conductivity, σ_f. The numbers labeling the curves are the $\frac{\sigma_f}{\sigma_r}$ values for which they are calculated.

Parameter	Value	Source
Stoneley wave frequency ω	$2\pi \cdot 150Hz$	Figure 2-5
Stoneley wave velocity c_s	$1400m/s$	Figure 2-5
borehole radius R_b	$0.15m$	Figure 2-3
fluid conductivity σ_f	$0.022S/m$	salinity of $0.004mol/l$ NaCl
fluid viscosity μ	$10^{-3}Pa \cdot s$	CRC (1978)
fluid permittivity ϵ_f	$7.1 \cdot 10^{-10}coul^2/(N \cdot m^2)$	CRC (1978)
fracture tortuosity α_∞	1	after Brown *et al.* (1998)
zeta potential ζ	$-60mV$	from Morgan *et al.* (1989)

Table 3.1: Parameters of the experiment used for amplitude comparison and for porosity estimation in granite.

Parameter	Value	Source
Stoneley wave frequency ω	$2\pi \cdot 200Hz$	Figure 2-18
Stoneley wave velocity c_s	$1400m/s$	Figure 2-18
borehole radius R_b	$0.076m$	Figure 2-14
fluid viscosity μ	$10^{-3}Pa \cdot s$	CRC (1978)
fluid permittivity ϵ_f	$7.1 \cdot 10^{-10}coul^2/(N \cdot m^2)$	CRC (1978)
formation conductivity σ_r	$2 \cdot 10^{-3}\frac{S}{m} = \frac{1}{500\Omega \cdot m}$	Figure 2-13
borehole fluid conductivity σ_f	$0.059\frac{S}{m} = \frac{1}{17\Omega \cdot m}$	fluid conductivity log
formation porosity ϕ	0.11 (i.e., 11%)	the average in Figure 2-24
norm. elsm ampl. $\frac{E}{P}$	$1.1 \cdot 10^{-8}\frac{V}{m \cdot Pa}$	the average in Figure 2-24

Table 3.2: Parameters of the experiment used for estimating the zeta-potential in dolomite.

Chapter 4

Electroseismic logging: broadband measurements of the Stoneley-wave-induced electrical potential

4.1 Introduction

The main goal of this thesis is to determine the practical value of electroseismic phenomena for geophysical exploration. In Chapter 2 we demonstrated that electrical fields induced by a borehole Stoneley wave can be measured in fractured igneous rocks and in sedimentary rocks (dolomite). Results of field experiments suggested that these electroseismic measurements can be used to identify permeable zones intersected by a borehole. In Chapter 3 we developed a theoretical model for the Stoneley-wave-induced electrical fields. This theoretical model suggests that porosity can be determined

from the normalized amplitudes of these electrical fields and that permeability can be determined from their amplitude-versus-frequency dependence.

Overall, the initial experimental results and the theoretical model's predictions are encouraging. However, a few problems need to be addressed before the borehole electroseismic measurements can be used in practice. The two most important problems are the following:

1. The measurement technique proposed in Chapter 2 has a depth limitation due to the use of a surface source and surface reference electrical dipoles. It is desirable to develop an electroseismic logging technique which uses a downhole source and downhole receivers for measuring the electrical fields induced by a borehole Stoneley wave.

2. The physical mechanism of the electroseismic phenomena observed in the experiments has to be established clearly in order to demonstrate which specific parameters of the formation can be determined from borehole electroseismic measurements. The theoretical model developed in Chapter 3 predicts that the porosity and the permeability of the formation can be deduced from the amplitude-versus-frequency dependence of the Stoneley-wave-induced electrical potentials. However, the field data presented in Chapter 2 has a narrow frequency content. Thus, we cannot make a direct comparison of the amplitude-versus-frequency dependence of the signals recorded in the experiments with the predictions of the theoretical model.

In this chapter we address the first problem and partially address the second. Specifically, we develop an experimental technique that allows logging-type measurements of the Stoneley-wave-induced electrical potentials. Using this technique, we measure these electrical potentials in the frequency range from $300Hz$ to $4000Hz$. Analysis of field data shows that the normalized amplitudes of the Stoneley-wave-induced electrical potential correlate with other geophysical measurements that indicate

the location of fractured zones.

To make a comparison between the field data and the theory, we combine the results of the experiments described in this chapter with the results of previous electroseismic experiments in the same borehole (Chapter 2) to obtain the amplitude-versus-frequency dependence of the Stoneley-wave-induced electrical potentials in the frequency interval from $100Hz$ to $4000Hz$. Comparison of this amplitude-versus-frequency dependence with the predictions of the Biot-theory-based theoretical model shows that the theory predicts correct values for the amplitude, but does not fully describe the variation of the amplitude with frequency.

4.2 Electroseismic logging technique

In this section we describe a measurement technique for recording the Stoneley-wave-induced electrical potential in a frequency range from several hundred hertz to several kilohertz. This measurement technique is suitable for electroseismic logging because both source and receivers are placed in the borehole.

4.2.1 Stoneley wave source

The first component of the measurement device is a Stoneley wave source. In the previous experiments (Chapter 2) we generated the Stoneley wave by striking a well head with a sledgehammer. This technique has three limitations:

1. Generating the Stoneley wave at the surface limits the depth of the investigation due to the reduction of the Stoneley wave amplitude by attenuation and backscattering as the wave propagates down a borehole.

2. A sledgehammer generates a narrow-band Stoneley wave ($70Hz$ to $300Hz$ in the experiments), and there is no way to control the frequency of the source.

3. Repeated striking with a sledgehammer damages well heads.

In the experiments described in this chapter we used a downhole piezoelectric source. This source was capable of generating Stoneley waves with frequencies from several hundred hertz up to several kilohertz. The source was a piezoelectric ring ($10cm$ in diameter, $1.5cm$ thick and $15cm$ long). To generate a Stoneley wave, we placed this piezoelectric ring in a borehole and sent a $2.5kV$ pulse to the ring from a high-power amplifier at the surface. The input to the amplifier was one period of a sinusoid. we varied the frequency of the sinusoidal input to control the frequency of the Stoneley wave generated by the source. In different experiments we used $2.5kHz$ and $5.0kHz$ sinusoids as the input to the amplifier.

4.2.2 Electrode configuration and the noise reduction processing

To record the electrical potentials induced by the Stoneley wave, we used a 4-electrode array (Figure 4-1). In addition to recording electroseismic signals, this array allowed to cancel the noise generated by the remote power lines and by telluric currents in the ground.

As we already discussed in Chapter 2, canceling the electrical noise created by remote power lines and by telluric currents is the major challenge in making electroseismic measurements. While the electroseismic signals detected in field experiments have amplitudes ranging from hundreds of nanovolts to tens of millivolts, the power-line-induced and telluric electrical currents generated signals with amplitudes up to

several millivolts. In previous surface experiments (Mikhailov *et al.*, 1997) and borehole experiments (Chapter 2), we demonstrated that the most effective way to reduce this noise in electrical data is remote referencing. In the field, while recording the electrical signals in the borehole, we simultaneously recorded the electrical noise on two mutually perpendicular electrical dipoles on the surface. During signal processing we subtracted the noise recorded on the surface from the measurements in the borehole.

In experiments we found that at kilohertz frequencies the power line and telluric noise varies significantly with depth. Therefore, it was not sensible to make reference measurements at the surface or at some depth far from the depth where the electroseismic signals are recorded. We were forced to make reference measurements in the immediate vicinity of the depth where the electroseismic signals were measured. Since the reference electrodes were placed in the immediate vicinity of the measurement electrodes, the reference electrodes also recorded electroseismic signals. In a way, there was no longer any difference between the "measurement" and "reference" electrodes. Thus, we called them all "measurement" electrodes and in this way came up with a 4-electrode measurement array.

Figure 4-1 shows a diagram of the 4-electrode measurement array. In the experiment the electrodes were separated by $0.5m$. In the field we recorded two signals: the potential difference between the electrodes a and b, and the potential difference between the electrodes c and d. The power line and telluric noise recorded by these electrode pairs was practically the same because the sources of the noise were very far from the electrodes. At the same time, the electroseismic signals recorded by the two electrode pairs, (ab) and (cd), were different because the Stoneley wave length was comparable with the distance between the electrodes.

During processing, we subtracted the (cd) signal from the (ab) signal. Therefore,

the resulting measurement obtained in field experiment was

$$A_{4el} = (\Phi_a - \Phi_b) - (\Phi_c - \Phi_d)\,. \tag{4.1}$$

If the Stoneley wave length is much larger than the distance between the electrodes, then this measurement A_{4el} is proportional to the second derivative of the electrical potential along the borehole axis.

4.3 Field experiment

In this section we demonstrate that by using the experimental technique described above, it is possible to make field measurements of the electrical potential induced by the borehole Stoneley wave. We first present the details of the experiment and then present field data. In the data we identify the electrical signals generated by the Stoneley wave.

4.3.1 Experimental site

We conducted field experiments in a well drilled through fractured igneous rock at a site in Hamilton, MA (same well as in Chapter 2). Measurements were made in the depth interval from $30m$ to $52m$, that was in granite. Figure 4-2 presents results of different geophysical measurements. These measurements demonstrate that the granite formation in this depth interval is highly fractured. The borehole caliper log shows enlargements of the borehole wall at depths where a drill bit encountered fractures in the hard rock. The P-wave slowness log has kicks (off scale) corresponding to fractured zones. The borehole video for the well shows numerous fractures intersecting the borehole throughout the entire depth of investigation. We derived a plot of fracture locations and "size" from the borehole video log. The "size" of

the fractures (as they appear in the video) are plotted on a "coffee-shop" scale, i.e., small/medium/large (1, 2 and 3 in Figure 4-2). The conductivity log shows relatively high conductivity values for igneous rock, again corresponding to highly fractured granite.

Analysis of the cuttings from the well GEOSS (1984a,b) demonstrates that in granite the rock matrix has no porosity. Thus, all the porosity and permeability of the granite formation are due to fractures. A pumping test in another well that is $12m$ away from the experimental well yielded a water flow rate of $300gal/min$ ($1.9 \cdot 10^{-2} m^3/s$) that was sustained for 26 days (Haley and Aldrich, Inc., 1990). The main flow conduit identified by the pumping test was the fractured zone between the depths of $55m$ and $61m$. The pumping test demonstrated that there is a flow communication between the two wells through horizontal fractures in the subsurface. Therefore, we can conclude that the fractures intersecting our experimental well are permeable.

In the depth interval of investigation the well was uncased. This allowed pressure communication between the borehole and the fractures. When the Stoneley wave propagated along the borehole, it induced a flow of fluid within the fractures. Thus, the borehole was suitable for electroseismic experiments.

4.3.2 Field experimental procedure

In experiments we recorded pressure oscillations and electrical signals generated by a borehole Stoneley wave. To measure pressure we used hydrophones with a sensitivity of $10mV/Pa$. To record the electrical signals we used the 4-electrode array described in the previous section.

During the experiment we placed the piezoelectric source at a fixed depth ($30m$

and $35m$ in different experiments) and moved the electrode array or the hydrophone array along the borehole to obtain measurements throughout a $16m$ depth interval at a $0.25m$ spacing between traces. In electrical experiments we obtained one electroseismic trace at a time (recording two signals $(\Phi_a - \Phi_b)$ and $(\Phi_c - \Phi_d)$ in the field, and later combining them to cancel the noise). In the hydrophone experiments we recorded three traces at a time using a three-hydrophone string. In our experiments the source was not moving, so this was not an actual logging experiment. Nevertheless, our measurement device can be moved as a whole along the borehole, thus allowing logging-type measurements.

To record the signals measured by the electrodes and by the hydrophones we used the same data acquisition system as in previous experiments (a dynamic range of $120dB$ and a crosstalk between channels of less than $-100dB$). The highest sampling rate of the data acquisition system was $16kHz$. At this sampling rate the system imposed a de-aliasing low-pass filter at half of the Nyquist frequency, i.e., the signals with frequencies above $4kHz$ were filtered out. Unfortunately, this feature of the data acquisition system limited electroseismic experiments to recording only signals with frequencies below $4kHz$.

In electrical experiments we stacked data 1000 times at each depth, and in the hydrophone experiments, 20 times at each depth in order to increase the signal-to-noise ratio. Overall, using a 4-electrode array and stacking the data allowed us to detect electroseismic signals in the field. The best signal-to-noise ratio in the electrical data was around 5.

4.3.3 Full-waveform electroseismic data

Figures 4-3 to 4-6 present the pressure and electrical data collected in the field. In each Figure the depth of the electrical trace is the depth of the top electrode in the 4-electrode array. The data in Figures 4-3 and 4-4 were collected with the source at the depth of $35m$ and the data in Figures 4-5 and 4-6 - with the source at the depth of $30m$. The data in Figures 4-3 and 4-5 were collected using a $2.5kHz$ sinusoid as an input to the high-power amplifier, and the data in Figures 4-4 and 4-6, with a $5.0kHz$ sinusoid as the input. The source time in Figures 4-3—4-6 is $10ms$. Three events can be identified in the electrical data in Figures 4-3—4-6.

1. The most visible event in the electrical data is the electromagnetic wave radiated by the piezoelectric source. This electromagnetic wave propagates with a velocity much higher than velocities of seismic waves, and arrives "simultaneously" at all depths at the time of the source ($10ms$).

2. Electrical data contain an electrical signal that propagates along the borehole with the Stoneley wave velocity and arrives at the electrodes simultaneously with the Stoneley wave (Event S-S). Event S-S is clearly visible in the data collected with the $2.5kHz$ source frequency (Figures 4-3 and 4-5). At the same time, Event S-S is barely visible in the data collected with the $5.0kHz$ source frequency (Figures 4-4 and 4-6). The poor quality of the signals measured with the $5.0kHz$ source is due to the fact that the data acquisition system had a built-in $4.0kHz$ low-pass filter. The barely visible traces of Event S-S in Figures 4-4 and 4-6 are all that was left in the data collected with a $5.0kHz$ source frequency after all the frequencies above $4.0kHz$ were cut out by the data acquisition system. Nevertheless, in experiments we recorded electroseismic signals in the frequency range from $300Hz$ to $4.0kHz$ (Figures 4-3 and 4-5). These electrical potentials induced by the Stoneley wave are the focus of this thesis.

3. Electrical data in Figures 4-3—4-6 contain an electrical signal that appears to "originate" at the time of the source ($10ms$) at some depth below the source. This signal has a Stoneley wave moveout. We label this signal "M-M" to emphasize its "mysterious" origin. Comparison of the electrical traces with the hydrophone traces shows that at the time when this signal is measured, there is no pressure wave propagating at the depth of the electrodes. We analyze this mysterious signal in Appendix C, and show that it was recorded by some kind of fault in the cable that connected the electrode array with the data acquisition at the surface. The analysis in Appendix C suggests that this fault is about $14m$ above the top electrode. Visual inspection of the cable did not indicate any fault. We chose not to cut the cable because it is expensive, and we would like to use it in future experiments.

Figure 4-7 presents the electrical data ($35m$ source depth, $2.5kHz$ source frequency) band-pass filtered in the interval from $300Hz$ to $1500Hz$. In these data, the mysterious Event M-M is not visible. Figure 4-8 presents the same electrical data band-pass filtered in the interval from $1500Hz$ to $4000Hz$. In these data Event M-M is very clear. Thus, the frequency of the mysterious signal is above $1500Hz$. We suggest that this signal's presence does not compromise the validity of our measurements at frequencies below $1500Hz$. However, this event may be an indication that the electroseismic data at frequencies above $1500Hz$ is corrupted by signals of non-electroseismic origin.

Overall, this section demonstrates that the experimental technique that we developed is suitable for measuring the electrical potential induced by a Stoneley wave at frequencies up to $4kHz$ (the maximum frequency that could be recorded by the data acquisition system).

4.4 Analysis of the Stoneley-wave-induced electrical potential

In this section combine the results of two different electroseismic experiments made in the same borehole. The first is the experiment made with the 4-electrode array, the piezoelectric source at the depth of $35m$, and a $2.5kHz$ frequency of the driving signal for the source (Figure 4-3). We analyze this dataset out of the four presented above because it had the best signal-to-noise ratio. In the other datasets the electroseismic signals are only slightly stronger than the noise. Also in this section we reanalyze results of an electroseismic experiments made in the same well using a 2-electrode array and a sledgehammer source (Chapter 2). Figure 4-9 presents the pressure and electrical data collected in the sledgehammer experiment in the depth interval from $36m$ to $52m$. In Figure 4-9 the direct Stoneley wave in the pressure data and the Stoneley-wave-induced electrical signals are labeled S-S.

First, we derive from the field data the normalized amplitude of the electrical potential induced by the Stoneley wave at different frequencies. Next we compare this normalized amplitude with the results of other geophysical measurements and show that the normalized amplitude of the Stoneley-wave-induced electrical potential correlates with the results of other geophysical measurements that indicate fractured zones.

4.4.1 Deriving the normalized amplitudes of the Stoneley-wave-induced electrical potential at different frequencies from the field data

We define the normalized amplitude of the Stoneley-wave-induced electrical potential as a ratio of the amplitude of the electrical potential oscillation at a certain depth to the amplitude of the pressure oscillation at the same depth. To derive this normalized amplitude at different frequencies from the field data, we used the following algorithm:

1. Apply a band-pass filter, centered around the frequency of interest, to the pressure and the electrical data.

2. Calculate from the band-pass-filtered data the rms amplitudes of pressure and electrical signals in the direct Stoneley wave (Event S-S) at the frequency of interest. Calculate these amplitudes for the main wavelets of Event S-S.

3. Convert the amplitudes of the electrical signals at the frequency of interest into the amplitude of the electrical potential oscillation, $\Phi(\omega)$, at this frequency. The formulas for this conversion are derived in Appendix D. To convert the amplitudes of the signals measured using the 4-electrode array into the amplitude of the electrical potential, divide the amplitude of the electrical signal, $A_{4el}(\omega)$, by the correction factor, $\frac{A_{4el}}{\Phi}(\omega)$ (Equation D.4), at the frequency of interest. To convert the amplitudes of the signals measured using a 2-electrode array, divide the amplitude of these electrical signals, $A_{2el}(\omega)$, by the correction factor $\frac{A_{2el}}{\Phi}(\omega)$ (Equation D.7) at the frequency of interest.

4. Divide the amplitude of the electrical potential oscillation, $\Phi(\omega)$, by the amplitude of the pressure oscillation at that frequency to obtain the normalized amplitude of the Stoneley-wave-induced electrical potential at the frequency of interest.

Table 4.1 presents the list of the frequencies for which we calculated the normalized amplitudes of the Stoneley-wave-induced electrical potential. Also, Table 4.1 presents the list of the band-pass filters applied to the data (Step 1 of the above algorithm) prior to calculating the rms amplitudes at the corresponding frequencies. We chose the frequency values, at which the amplitudes are calculated, such that they are equally spaced on the logarithmic scale. The band-pass filters are chosen such that they cover equal intervals on the logarithmic scale.

4.4.2 Comparing the amplitude of the Stoneley-wave-induced electrical potential with other geophysical measurements

Figure 4-10 presents a comparison of the normalized amplitudes of the Stoneley-wave-induced electrical potential to the results of other geophysical measurements. The P-wave log in Figure 4-10 has kicks off scale (more than $380\mu s/m$) in the depth intervals $45m-47m$ and $49m-53m$. This high P-wave slowness indicates that granite in these intervals has high fracture porosity. The electroseismic signals amplitudes in these depth intervals are higher than in the depth interval $47m - 49m$, where the P-wave slowness log indicates low fracture porosity.

Further, the plot of fracture locations derived from the borehole video (the third plot in Figure 4-10) shows a large fracture intersecting the borehole at the depth of $51m$. At this depth, the electroseismic signals have larger amplitudes than at other depths. This result, similar to the results of previous electroseismic experiments (Chapter 2), suggests that fractures can be identified using borehole electroseismic measurements.

4.5 Comparison of the field data and theory: amplitude-versus-frequency dependence of the Stoneley-wave-induced electrical potential

4.5.1 Synthetic amplitude-versus-frequency curves for the Stoneley-wave-induced electrical potential

In this section we analyze the synthetic amplitude-versus-frequency dependence of the Stoneley-wave-induced electrical potential, that are calculated using Equation 3.13 for the borehole and formation properties in the experiments. These properties are summarized in Table 4.2. The Stoneley wave velocity, c_s, is determined from the hydrophone measurements (Figure 4-3). The borehole diameter, R_b, is determined from the caliper log (Figure 4-10). The value of the borehole fluid conductivity, σ_f, corresponds to the salinity of $0.004 mol/l$ of NaCl measured for a sample of the actual borehole fluid (water). The values of the fluid viscosity, μ, and permittivity, ϵ_f, are the values for water. For the borehole fluid salinity in the experiments ($0.004 mol/l$ of NaCl, $\sigma_f = 0.022 S/m$), the value of the zeta-potential for granite has been measured laboratory experiments (Morgan *et al.*, 1989). In experiments with a natural fracture, Brown et al. (1998) found fracture tortuosity, α_∞, to be close to 1 due to channeling. Thus, in calculations we assume the tortuosity of fractures, α_∞, to be 1.0. The rock conductivity, σ_r, is measured in for borehole (Figure 4-2). For the porosity of fractured granite, ϕ, we assumed the value of 0.5% (Nur, 1969; Hadley, 1976; Toksöz *et al.*, 1976).

Figure 4-11 presents the synthetic amplitude-versus-frequency curves for the Stoneley-wave-induced electrical potential in the frequency interval from $100 Hz$ to $10 kHz$. The different curves in Figure 4-11 are calculated for permeability values ranging from

$10^{-14}m^2$ ($0.01Darcy$) up to $10^{-10}m^2$ ($100Darcy$). Figure 4-11 shows that for permeabilities less than $10^{-13}m^2$ ($0.1Darcy$) the Biot critical frequency, ω_c, is greater than the maximum frequency of the field experiments ($4000Hz$). Thus, according to the theoretical model, borehole electroseismic measurements are not sensitive to permeability values of less than $10^{-13}m^2$ ($0.1Darcy$). In the next section we will compare this synthetic curves to the real data in order to assess the possibility of determining permeability from the field measurements.

4.5.2 Comparison between the synthetic curves and the field data

In this section we present the amplitude-versus-frequency dependence of the Stoneley-wave-induced electrical potential measured in the field in the frequency range from $100Hz$ up to $4000Hz$. We compare the results of the field measurements with the synthetic amplitude-versus-frequency curves predicted by the theoretical model for the borehole fluid and formation properties in the experiment.

We compare the field data to the theoretical model in four depth intervals: $46.5m-47.5m$ (Figure 4-12), $47.5m-49.5m$ (Figure 4-13), $49.5m-50.5m$ (Figure 4-14) and $50.5m-51.5m$ (Figure 4-15). The first conclusion which can be drawn from Figures 4-12 to 4-15 is that the theory predicts the correct values for the normalized amplitudes of the electroseismic signals. Further analysis of Figures 4-12 to 4-15 shows that the amplitudes of the signals measured in the field have a more complicated frequency dependence than the one predicted by the theory. In the frequency range from $200Hz$ to $800Hz$, the normalized amplitudes of the Stoneley-wave-induced electrical potential have a steeper decrease with frequency than the $\omega^{-\frac{1}{2}}$ decrease predicted by the theory. Further, in Figures 4-12 to 4-14 the normalized amplitudes increase with frequency above $800Hz$.

In the depth interval around the large fracture ($50.5m - 51.5m$), the normalized amplitude of the Stoneley-wave-induced electrical potential roughly follow the trend predicted by the theory. However, the data has a similar "dip" at the $800Hz$ frequency and a slight increase above it. The synthetic curves in Figure 4-15 were calculated for the fracture porosity value of 1.2%. The normalized amplitudes measured in this depth interval fall between the synthetic curves corresponding to the permeability values of $1.25 \cdot 10^{-11} m^2 = 12.5 Darcy$ and $1.25 \cdot 10^{-10} m^2 = 125 Darcy$. These porosity and permeability estimates values cannot be compared with any other independent porosity and permeability measurements in this borehole. Thus we do not claim that they are correct. However, the fact that the amplitude-versus-frequency dependence of the electroseismic signals measured in the depth interval around the large fracture roughly agrees with the theoretical model suggests that the model of the Stoneley-wave-induced electrical potential may work for large fractures.

4.6 Discussion

The theoretical model predicted correct values for the amplitudes of the Stoneley-wave-induced electrical potentials that were measured in the field. Also, the Stoneley-wave-induced electrical potentials had a clear peak of the normalized amplitude at the depth of the large fracture Figure 4-10. However, the amplitude-versus-frequency dependence of the electroseismic signals measured in the experiments was more complex than the one predicted by the model. This disagreement between the field data and the theory can be attributed to one of the following five factors:

1. We made electroseismic measurements using a 4-electrode array. We derived the sensitivity function, $\frac{|A_{4el}|}{|\Phi_a|}(\omega)$, for the array, assuming that we made ideal four-point measurements (Appendix D). To deduce the amplitudes of the electrical potential

oscillation in the borehole from the 4-electrode measurements, we divided the amplitudes of the measured signals by the sensitivity function, $\frac{|A_{4el}|}{|\Phi_a|}(\omega)$. Figure D-2 shows that the sensitivity function, $\frac{|A_{4el}|}{|\Phi_a|}(\omega)$, has a peak around $800Hz$. It is possible that the "dip" in the amplitude-versus-frequency dependence of the electrical potential at the $800Hz$ frequency is caused by dividing the original signals' amplitudes by the high values of the sensitivity function around $800Hz$. The coincidence of the "dip" in the amplitude-versus-frequency of the electroseismic signals with the peak of the sensitivity function suggests that in our experiments we did not make ideal four-point measurements, as we assumed in the derivation of the sensitivity function.

2. The measurement technique was not perfect and could have corrupted the signals at high frequencies. For example, there is a high frequency "mysterious" event in the electrical data. Also, regardless of the depth in the borehole, all the amplitude-versus-frequency curves have a 'dip' around the $800Hz$ frequency. However, the latter fact cannot be attributed to the data acquisition system, cable or lead electrodes. In Appendix F, we show that the instrument response of our measuring devices is not responsible for the "dip" in the amplitude-versus-frequency dependence of the electroseismic signals measured in the field.

3. The theoretical model only accounts for the amplitude-versus-frequency dependence of the streaming electrical current and does not take into consideration other frequency-dependent phenomena in the field. For example, we assumed that the formation conductivity, σ_r, is independent of frequency. However, Olhoeft (1985) demonstrated that, due to electrochemical reactions, resistivity of real rocks can have a complicated non-linear frequency dependence. Our experiments were made in granite saturated with water. Lockner and Byerlee (1985) measured conductivity of water-saturated Westerly granite and demonstrated that it does not significantly change in frequency range from $1Hz$ to 10^4Hz. However, analysis of thin sections of granite from Hamilton demonstrated that microcracks in granite are sealed with

siderite, that is a Fe-reach carbonate (GEOSS, 1984b). Moreover, grains of Fe-Ti oxide were detected in some of the thin sections (GEOSS, 1984b). IP responses of these minerals need to be examined before frequency-dependent conductivity effects can be ruled out.

4. The theoretical model is based on Pride's (1994) theory for dynamic streaming electrical currents and on the Biot theory. Pride's (1994) model assumes that the thickness of the charged layer of fluid near the pore surface is much smaller than the pore size. This assumption may not always be valid in real rocks. However, the theoretical model should be valid for large fracture apertures. This fact can explain why we had better agreement between the theory and the measurements at the large fracture.

5. Finally, in the field there could be more than one possible mechanism for a Stoneley wave to induce an electrical potential. In Appendix A we ruled out several alternative physical mechanisms for these electroseismic signals. These ruled-out mechanisms were the action of the Stoneley wave on the electrodes, the streaming potentials due to the fluid motion along the borehole wall, and the piezoelectric effect. However, the electroseismic phenomena are very complex and there could be a number of other phenomena present in the experiment.

4.7 Conclusion

In this chapter we described an experimental technique that allows making broadband logging-type measurements of the Stoneley-wave-induced electrical potential. Using this experimental technique we made borehole electroseismic measurements in the frequency range from $300Hz$ to $4000Hz$. Analysis of the signals measured in the field showed that the normalized amplitude of the Stoneley-wave-induced electrical

potential has a peak at the depth of a large fracture.

From the field data we derived the normalized amplitudes of the Stoneley-wave-induced electrical potential at different frequencies. We compared the amplitude-versus-frequency dependence of the Stoneley-wave-induced electrical potentials recorded in the field with the predictions of the theoretical model. From this comparison we found that the theoretical model predicts the correct magnitudes for the electrical potentials induced by the Stoneley wave. Also, the amplitude-versus-frequency dependence of the electroseismic signals recorded at the depth of the large fracture roughly follows the trend predicted by the theory. However, the general amplitude-versus-frequency dependence of the electroseismic signals recorded in the field is more complicated that the one predicted by the theory. This can be attributed to (a) imperfection of the measurement devices; (b) failure of the theoretical model to correctly describe the phenomenon observed in the field; or (c) the presence of some other electroseismic phenomenon that we do not account for. Further measurements with a better data acquisition system and a better measurement tool are necessary to establish the complete physics of the electroseismic phenomenon that we observed in the field.

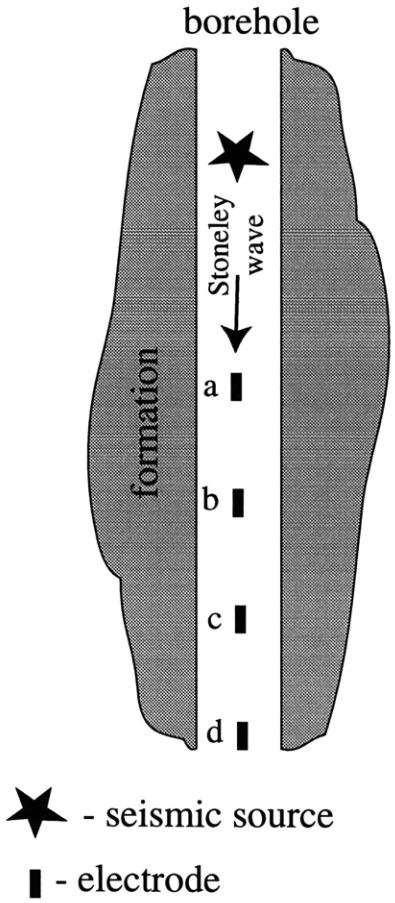

Figure 4-1: Diagram of the electroseismic logging experiment. A downhole seismic source generates a Stoneley wave propagating along the borehole. The Stoneley wave generates fluid flow within the formation, and this flow induces a streaming electrical potential. The 4-electrode array placed in the borehole detects the Stoneley-wave-induced electrical potential. The electrical signal measured by the array is: $A_{4el} = (\Phi_a - \Phi_b) - (\Phi_c - \Phi_d)$. If the Stoneley wavelength is much larger than the distance between the electrodes, then this signal, A_{4el}, is proportional to the second derivative of the Stoneley-wave-induced electrical potential along the borehole axis.

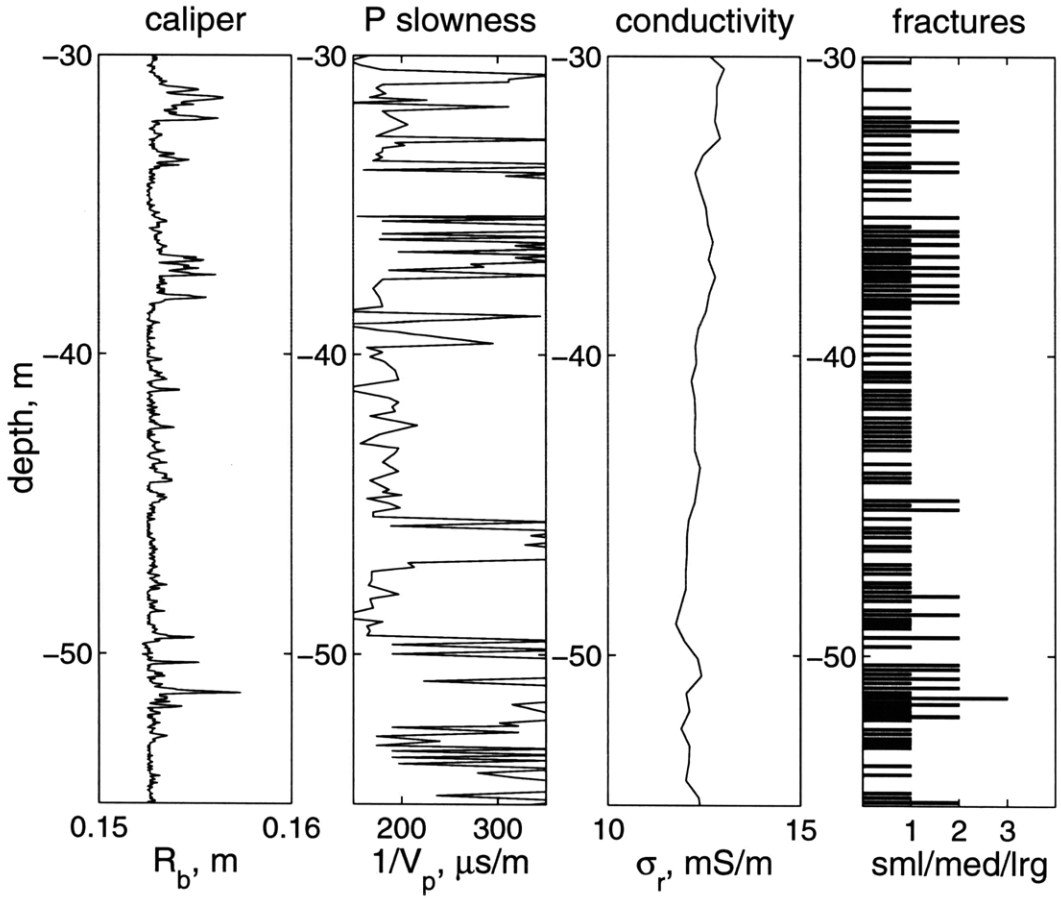

Figure 4-2: Results of different geophysical measurements in the depth interval from $30m$ to $52m$ demonstrating that the granite formation is highly fractured. The borehole caliper log shows enlargements of the borehole wall at depths where a drill bit encountered fractures in the hard rock. The P-wave slowness log has kicks off scale (above $380\mu s/m$) corresponding to fractured zones. The conductivity log shows relatively high conductivity values for igneous rock, again corresponding to highly fractured granite. The fracture location chart describes significant fractures detected by the borehole video. The size of the fractures is plotted on a "coffee shop" scale, i.e., small/medium/large.

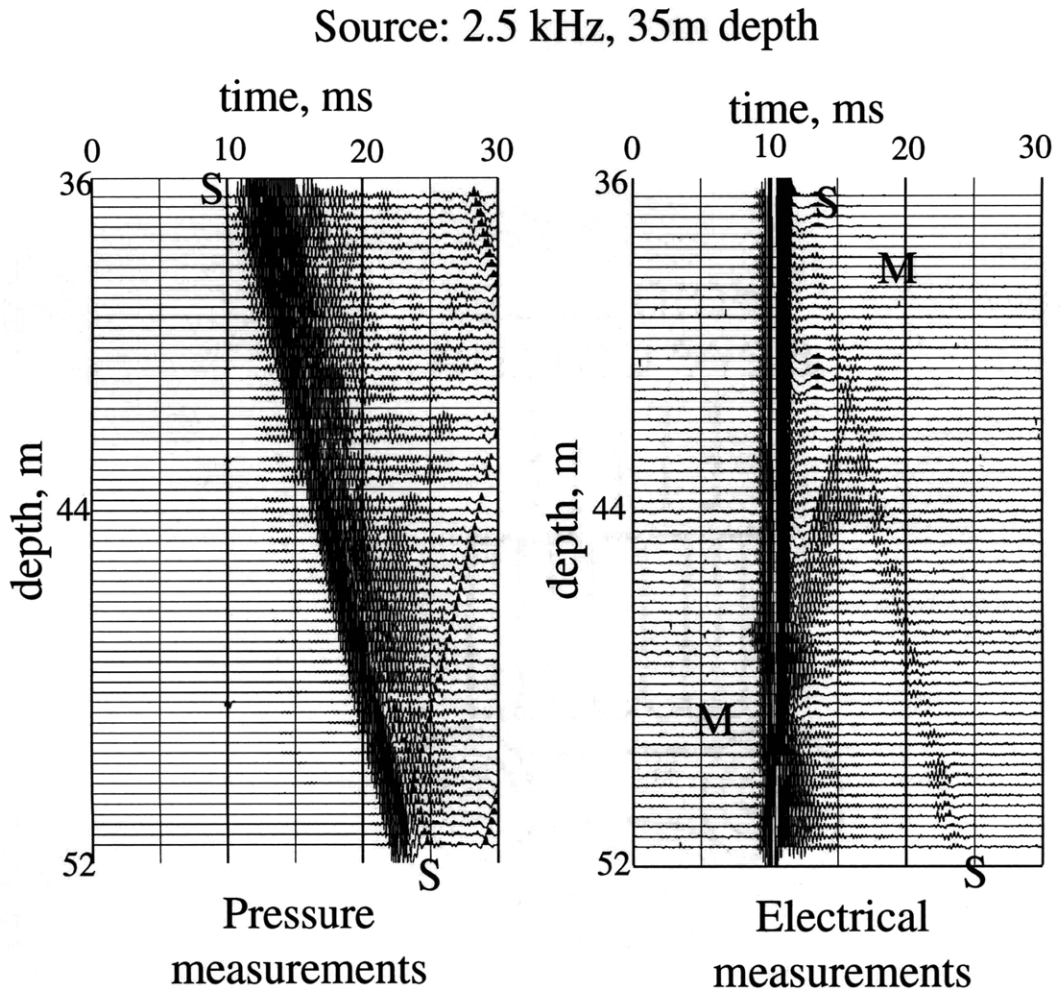

Figure 4-3: Pressure and electrical data collected in the field with the source at the depth of $35m$ and a $2.5kHz$ sinusoid as a driving signal for the source. The source time is $10ms$. The depth of the electrical trace is the depth of the top electrode in the 4-electrode array. In the pressure, data Event S-S is the direct Stoneley wave. In the electrical data, Event S-S is the electrical signal induced by the Stoneley wave, and Event M-M is the "mysterious" event caused by a fault in the cable.

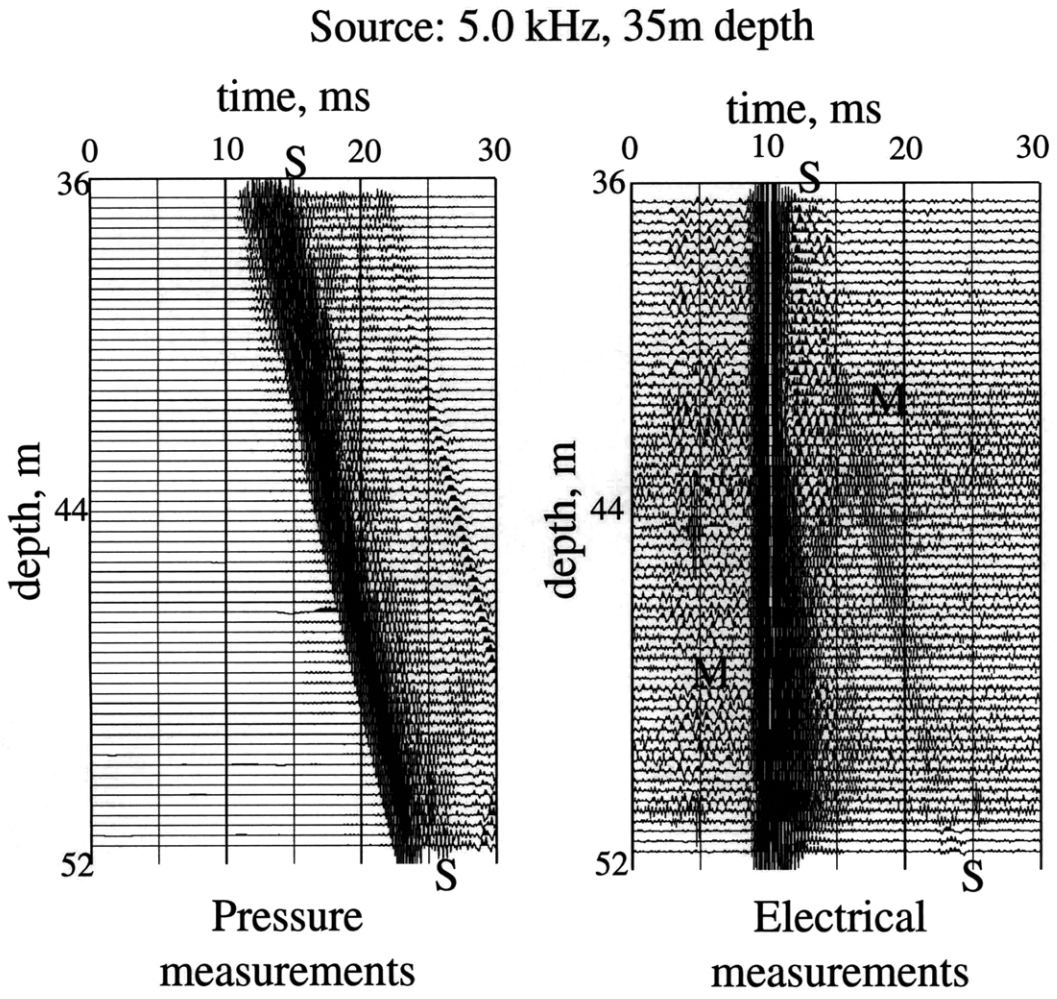

Figure 4-4: Pressure and electrical data collected in the field with the source at the depth of $35m$ and a $5.0kHz$ sinusoid as a driving signal for the source. The source time is $10ms$. The depth of the electrical trace is the depth of the top electrode in the 4-electrode array. In the pressure data, Event S-S is the direct Stoneley wave. In the electrical data, Event S-S is the electrical signal induced by the Stoneley wave, and Event M-M is the "mysterious" event caused by a fault in the cable.

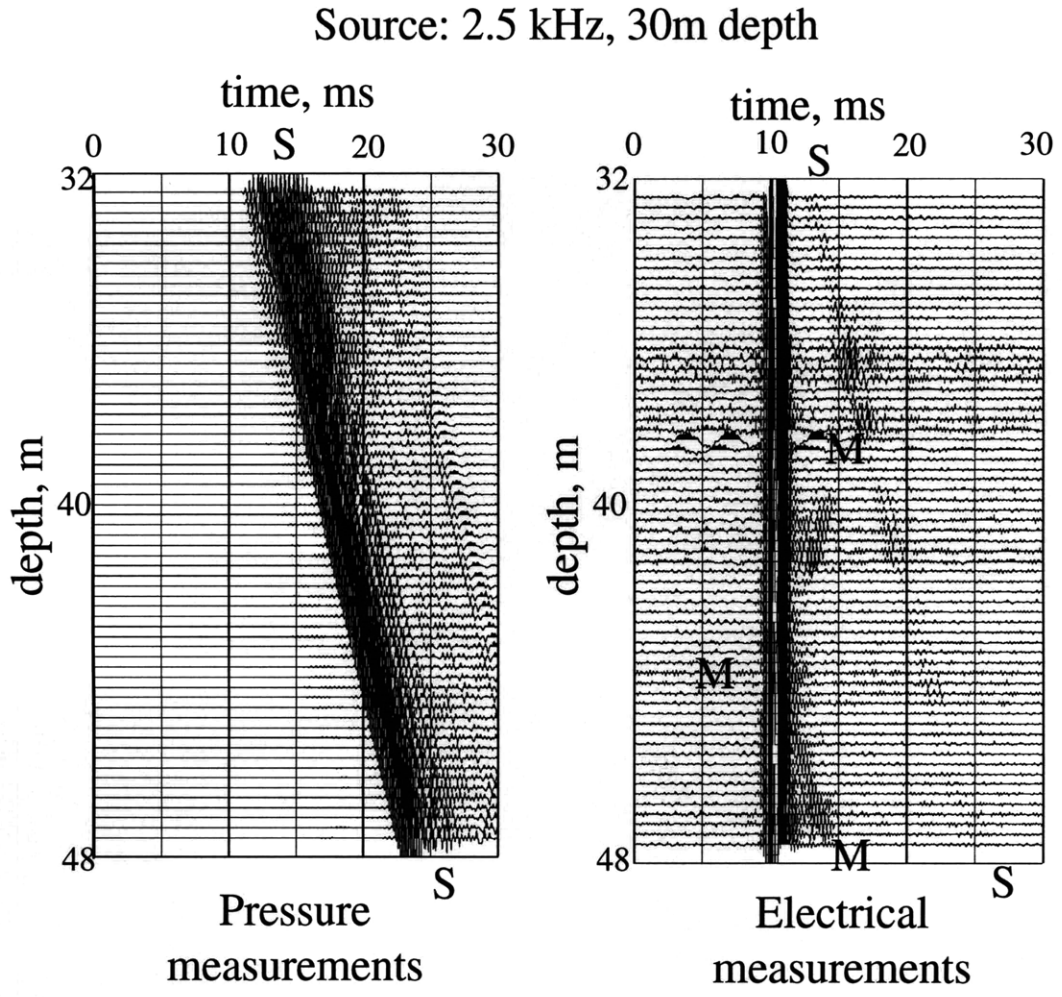

Figure 4-5: Pressure and electrical data collected in the field with the source at the depth of $30m$ and a $2.5kHz$ sinusoid as a driving signal for the source. The source time is $10ms$. The depth of the electrical trace is the depth of the top electrode in the 4-electrode array. In the pressure data, Event S-S is the direct Stoneley wave. In the electrical data, Event S-S is the electrical signal induced by the Stoneley wave, and Event M-M is the "mysterious" event caused by a fault in the cable.

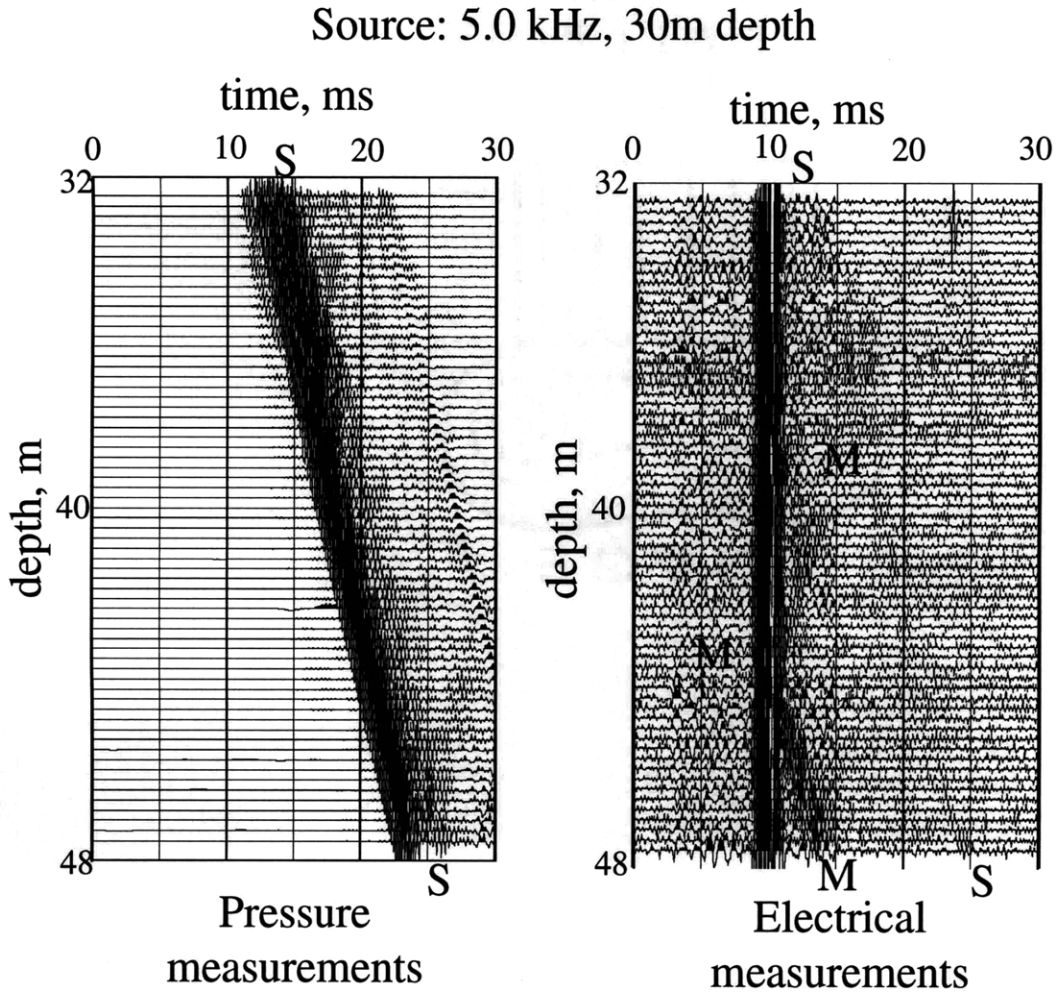

Figure 4-6: Pressure and electrical data collected in the field with the source at the depth of $30m$ and a $5.0kHz$ sinusoid as a driving signal for the source. The source time is $10ms$. The depth of the electrical trace is the depth of the top electrode in the 4-electrode array. In the pressure data, Event S-S is the direct Stoneley wave. In the electrical data, Event S-S is the electrical signal induced by the Stoneley wave, and Event M-M is the "mysterious" event caused by a fault in the cable.

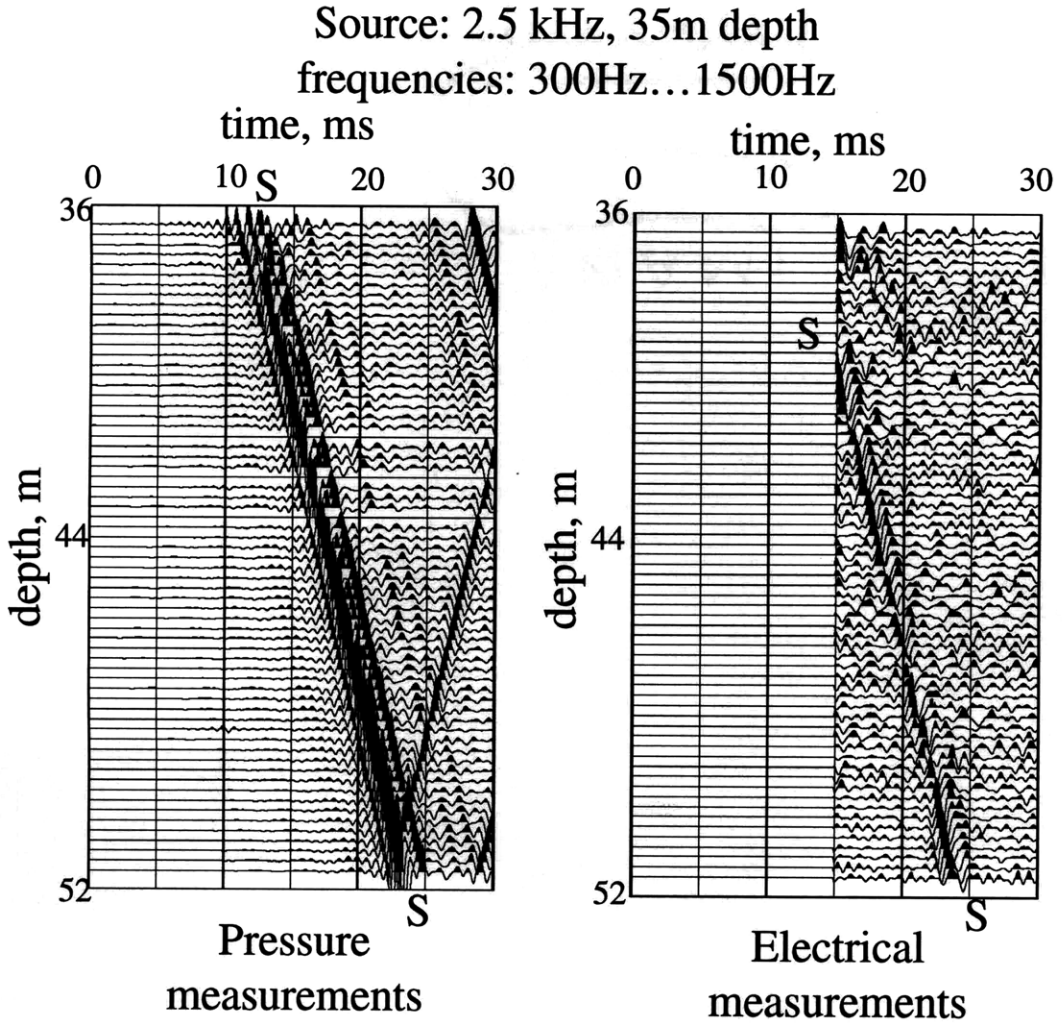

Figure 4-7: Pressure and electrical data collected in the field with the source at the depth of $35m$ and a $2.5kHz$ sinusoid as a driving signal for the source. These data are band-pass filtered in the frequency range from $300Hz$ to $1500Hz$. In the electrical data the signals before $15ms$ are muted prior to filtering in order to remove the electromagnetic wave radiated by the piezoelectric source. In the pressure data, Event S-S is the direct Stoneley wave. In the electrical data, Event S-S is the electrical signal induced by the Stoneley wave. Event M-M is not visible in these data.

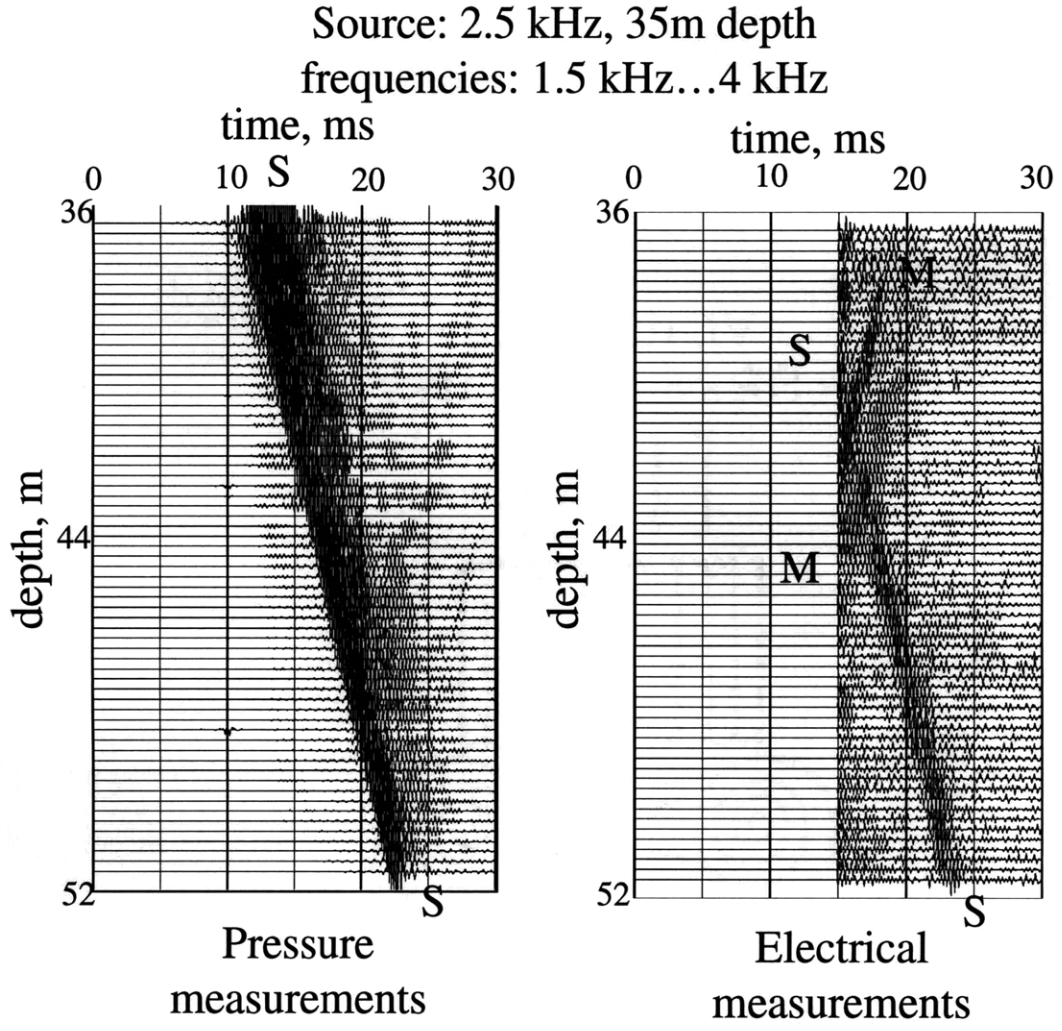

Figure 4-8: Pressure and electrical data collected in the field with the source at the depth of $35m$ and a $2.5kHz$ sinusoid as a driving signal for the source. These data are band-pass filtered in the frequency range from $1500Hz$ to $4000Hz$. In the electrical data the signals before $15ms$ are muted prior to filtering in order to remove the electromagnetic wave radiated by the piezoelectric source. In the pressure data, Event S-S is the direct Stoneley wave. In the electrical data, Event S-S is the electrical signal induced by the Stoneley wave. Event M-M is clearly visible in these data.

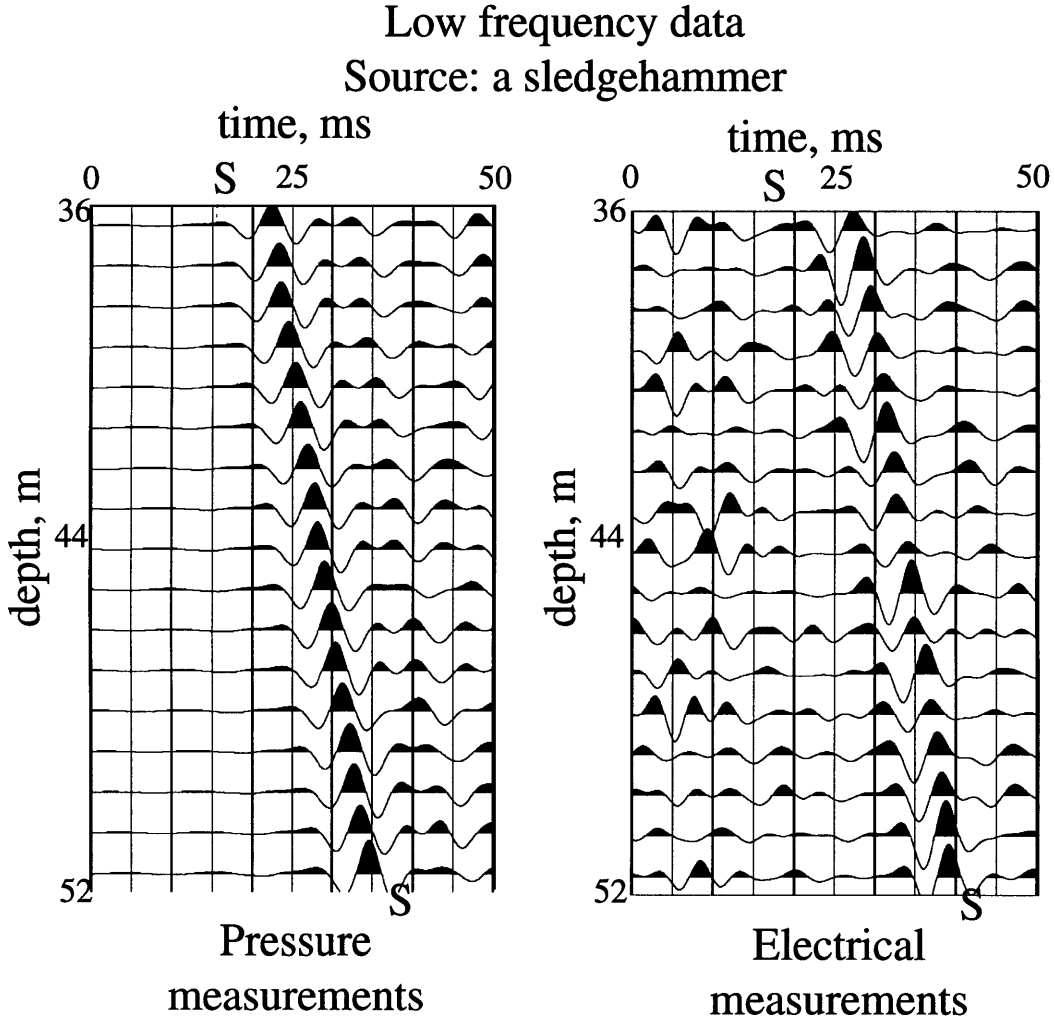

Figure 4-9: Pressure and electrical data collected in the previous experiments in the same borehole. The Stoneley wave was generated by striking the well head with a sledgehammer. The source time is $0ms$. The electrical fields were recorded using a 2-electrode array. The depth of the electrical trace is the depth of the top electrode in the 2-electrode array. In the pressure data, Event S-S is the direct Stoneley wave. In the electrical data, Event S-S is the electrical signal induced by the Stoneley wave.

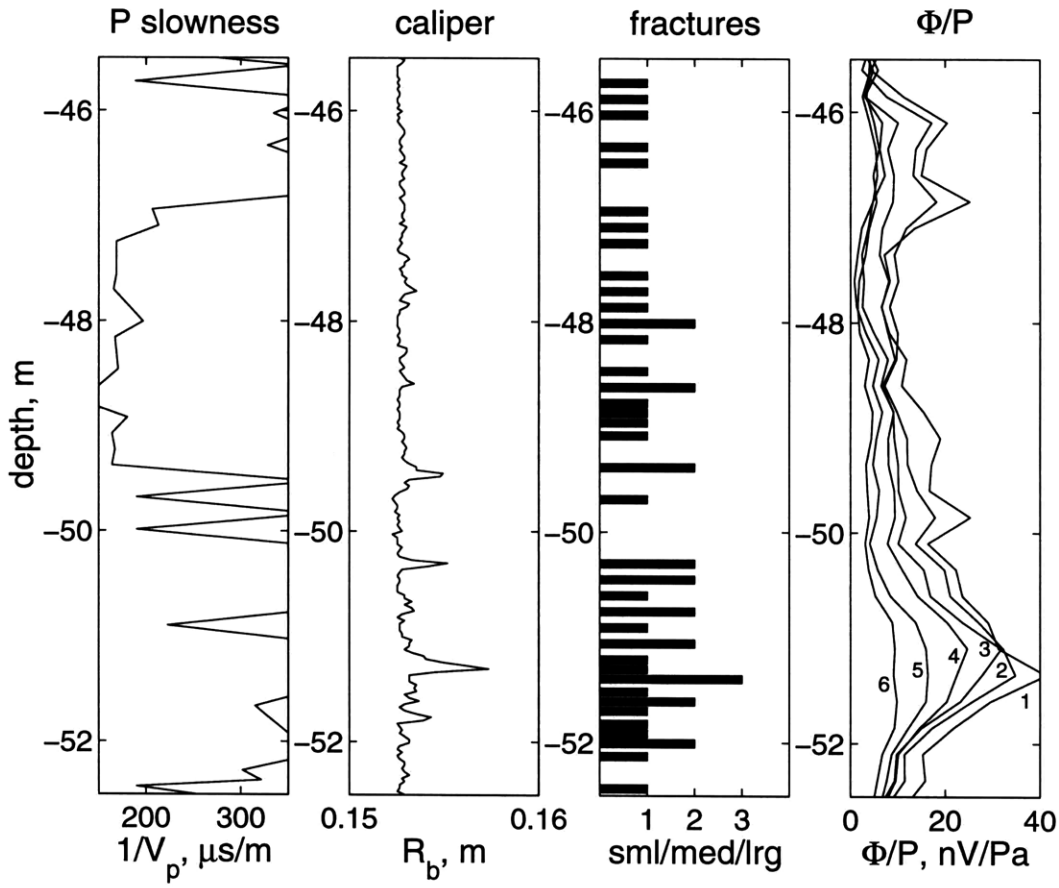

Figure 4-10: Comparison of the normalized amplitudes of the Stoneley-wave-induced electrical potential to the results of other geophysical measurements indicating fractures. In the plot of the normalized amplitudes of this electrical potential, curves 1–6 correspond to the frequency values $350Hz$, $410Hz$, $480Hz$, $560Hz$, $660Hz$ and $770Hz$, respectively. The P-wave log kicks off scale (more than $380\mu s/m$) in the depth intervals $45m - 47m$ and $49m - 53m$. This high P-wave slowness indicates that granite in these intervals has high fracture porosity. The electroseismic signals amplitudes in these depth intervals are higher than in the depth interval $47m - 49m$, where the P-wave slowness log indicates low fracture porosity. Further, the plot of fracture locations derived from the borehole video shows a large fracture at the depth of $51m$. At this depth the electroseismic signals' amplitudes have a strong peak. These correlations suggest that fractures can be identified using borehole electroseismic measurements.

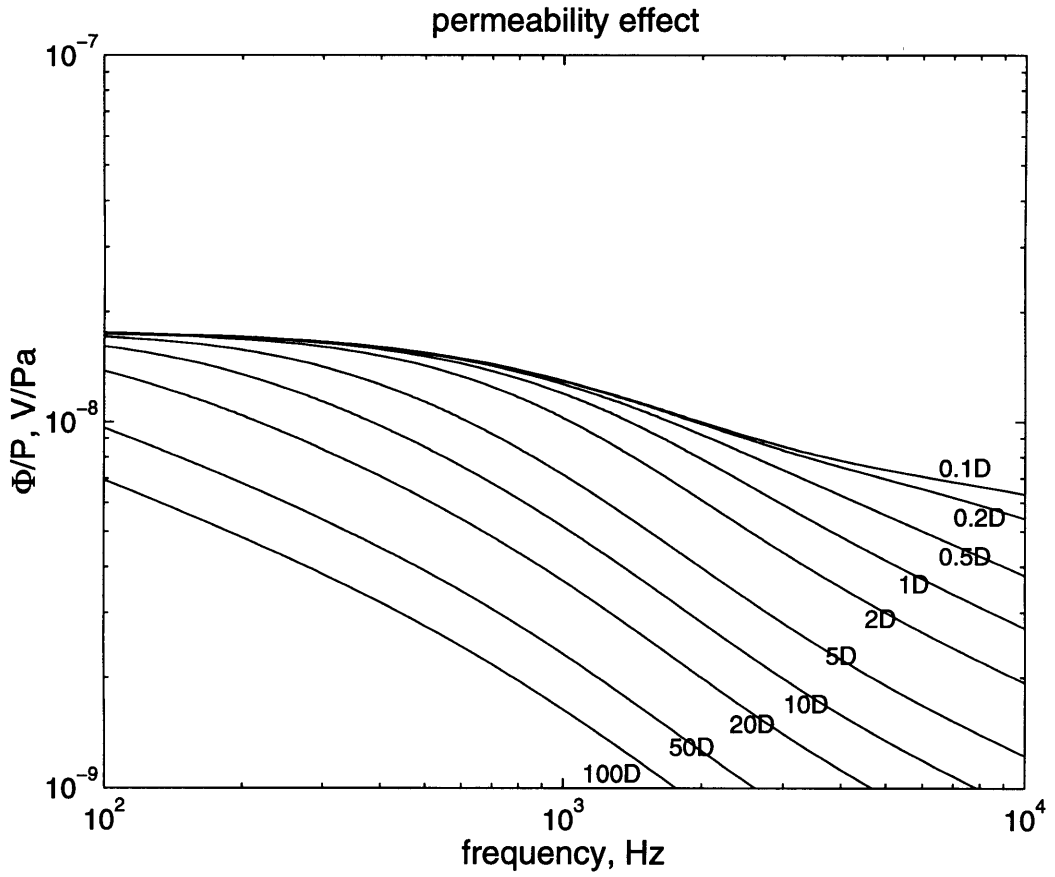

Figure 4-11: Synthetic amplitude-versus-frequency curves for the Stoneley-wave-induced electrical potential for the formation and borehole fluid properties in the experiments and different permeabilities. The different curves are calculated for permeability values ranging from $1.0^{-14}m^2$ ($0.01Darcy$) to $10^{-10}m^2$ ($100Darcy$). The numbers labeling the curves are the values of permeability (in $Darcy$) for which the curves are calculated. Equation 3.5 predicts that for permeabilities less than $10^{-13}m^2$ ($0.1Darcy$), the Biot critical frequency, ω_c, is greater than the maximum frequency of the field experiments ($4000Hz$). Thus, according to the theory, we cannot use borehole electroseismic measurements at frequencies less than $4000Hz$ to deduce permeability values of less than $10^{-13}m^2$ ($0.1Darcy$).

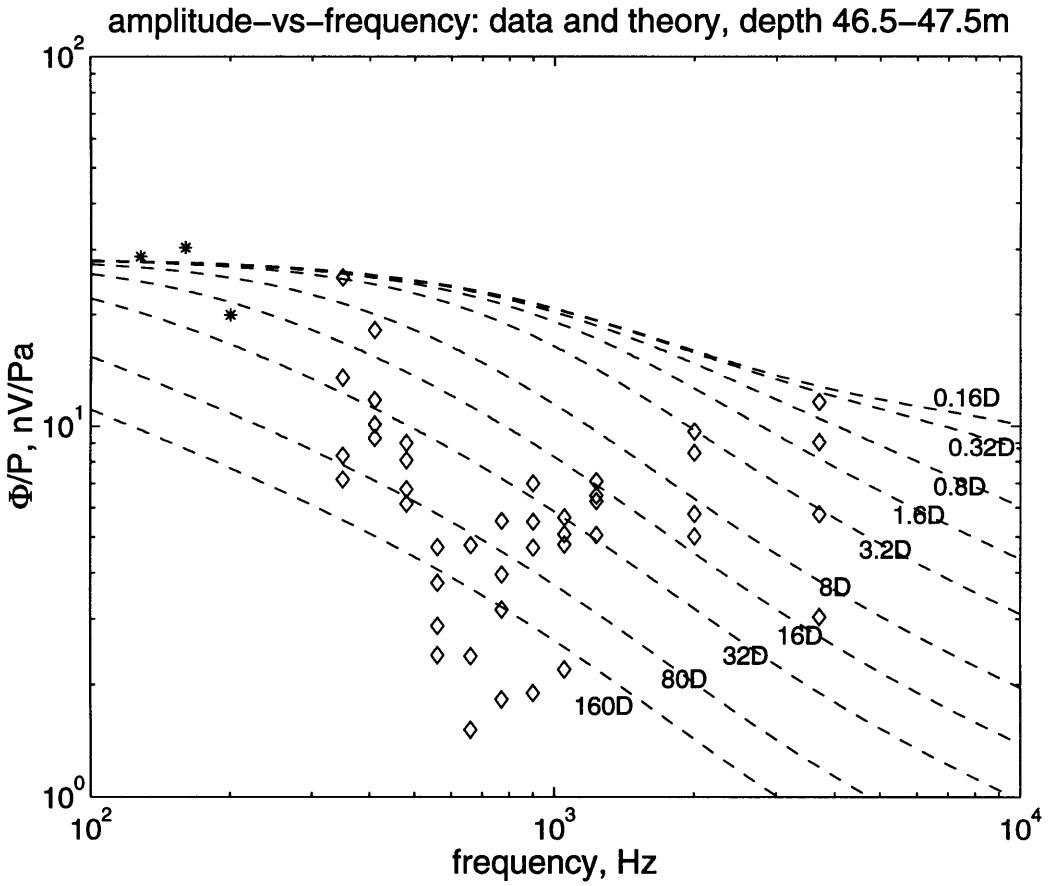

Figure 4-12: Comparison of the amplitude-versus-frequency dependence of the Stoneley-wave-induced electrical potentials measured in the depth interval from $46.5m$ to $47.5m$ with the predictions of the theoretical model. The synthetic curves are calculated for the formation and borehole fluid properties summarized in Table 4.2, porosity of 0.8% and various permeability values. The theory predicts the correct values for the normalized amplitudes of the electroseismic signals, however the normalized amplitudes of the signals measured in the field have a more complex frequency dependence than the one predicted by the theory. In the frequency range from $200Hz$ to $800Hz$, the normalized amplitudes of the Stoneley-wave-induced electrical potential have a steeper decrease with frequency than the $\omega^{-\frac{1}{2}}$ decrease predicted by the theory. Further, the normalized amplitudes increase with frequency above $800Hz$.

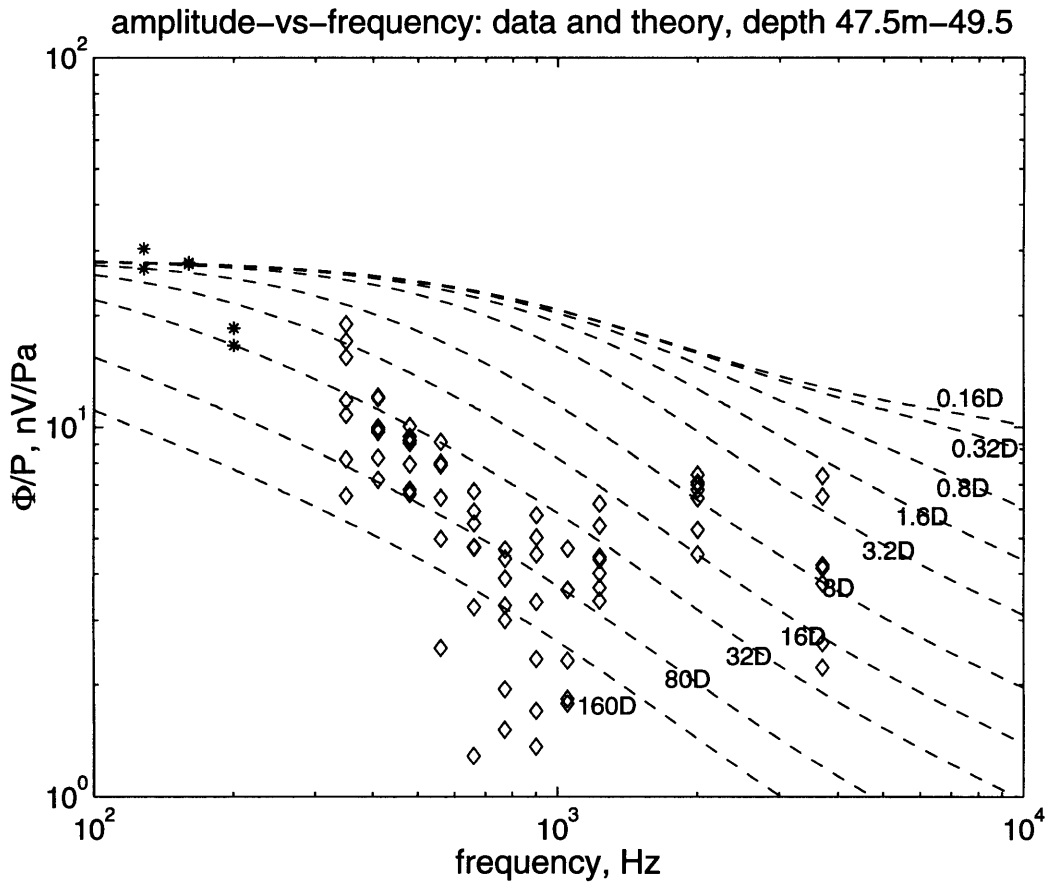

Figure 4-13: Comparison of the amplitude-versus-frequency dependence of the Stoneley-wave-induced electrical potentials measured in the depth interval from $47.5m$ to $49.5m$ with the predictions of the theoretical model. The synthetic curves are calculated for the formation and borehole fluid properties summarized in Table 4.2, porosity of 0.8% and various permeability values. The theory predicts the correct values for the normalized amplitudes of the electroseismic signals, however the normalized amplitudes of the signals measured in the field have a more complex frequency dependence than the one predicted by the theory. In the frequency range from $200Hz$ to $800Hz$, the normalized amplitudes of the Stoneley-wave-induced electrical potential have a steeper decrease with frequency than the $\omega^{-\frac{1}{2}}$ decrease predicted by the theory. Further, the normalized amplitudes increase with frequency above $800Hz$.

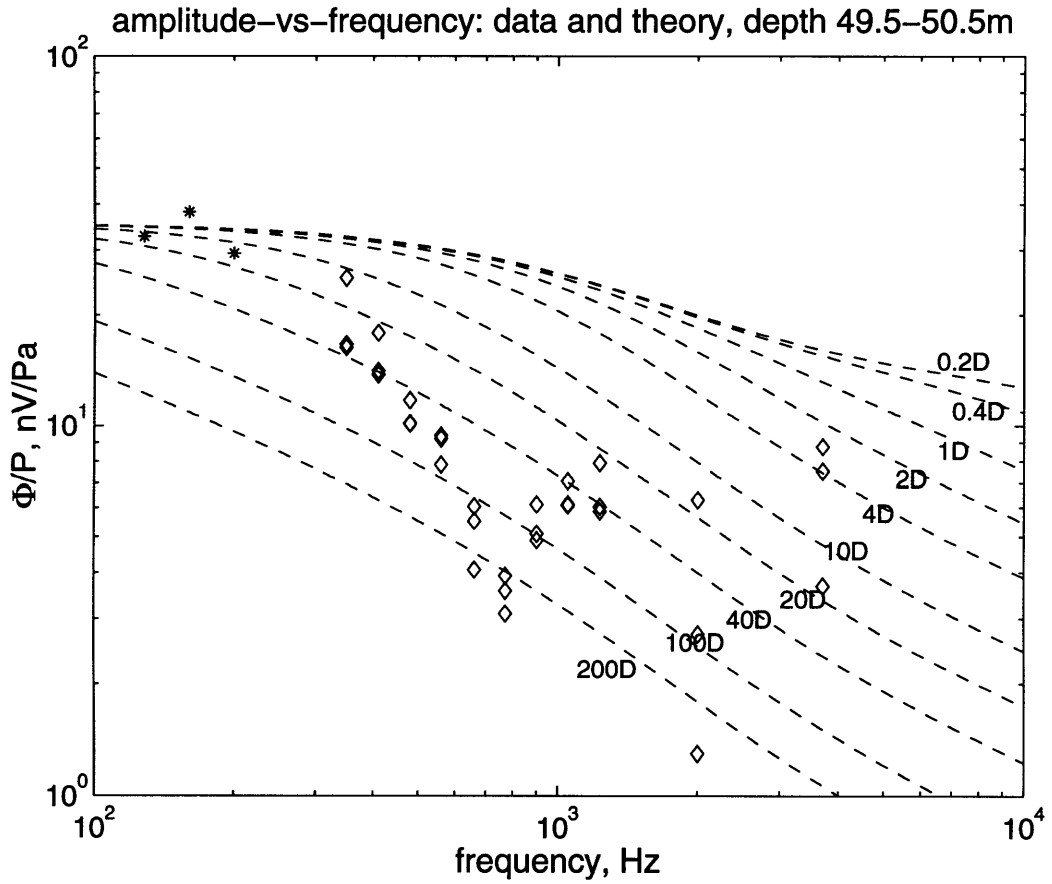

Figure 4-14: Comparison of the amplitude-versus-frequency dependence of the Stoneley-wave-induced electrical potentials measured in the depth interval from $49.5m$ to $50.5m$ with the predictions of the theoretical model. The synthetic curves are calculated for the formation and borehole fluid properties summarized in Table 4.2, porosity of 1.0% and various permeability values. The theory predicts the correct values for the normalized amplitudes of the electroseismic signals, however the normalized amplitudes of the signals measured in the field have a more complex frequency dependence than the one predicted by the theory. In the frequency range from $200Hz$ to $800Hz$, the normalized amplitudes of the Stoneley-wave-induced electrical potential have a steeper decrease with frequency than the $\omega^{-\frac{1}{2}}$ decrease predicted by the theory. Further, the normalized amplitudes increase with frequency above $800Hz$.

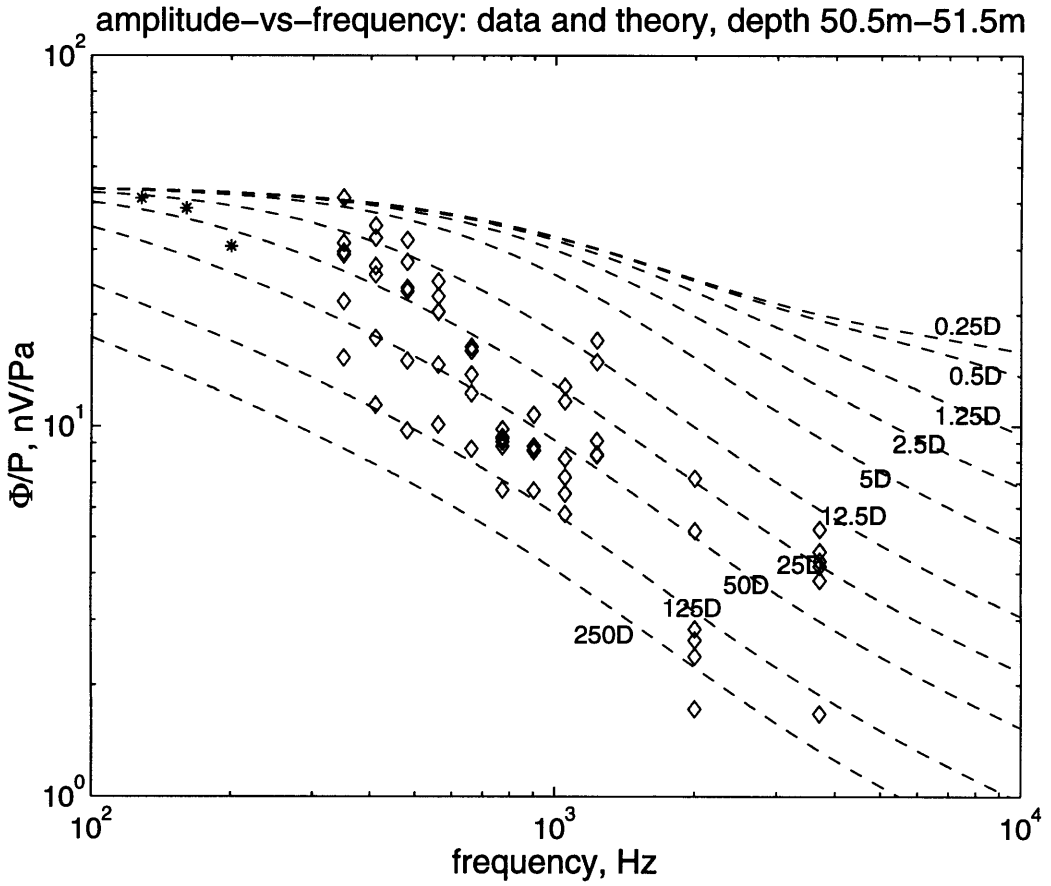

Figure 4-15: Comparison of the amplitude-versus-frequency dependence of the Stoneley-wave-induced electrical potentials measured in the depth interval from $50.5m$ to $51.5m$ (around the large fracture) with the predictions of the theoretical model. The synthetic curves are calculated for the formation and borehole fluid properties summarized in Table 4.2, porosity of 1.2% and various permeability values. The normalized amplitudes of the signals measured in the field seem to follow roughly the amplitude-versus-frequency trend predicted by the theory. However, this amplitude-versus-frequency trend corresponds permeability values between $1.25 \cdot 10^{-11} m^2$ ($12.5 Darcy$) and $1.25 \cdot 10^{-10} m^2$ ($125 Darcy$). These permeability values are enormous, so we cannot claim that the data agrees with the theory.

Frequency	Band-pass filter	Experiment
$128Hz$	$102Hz - 154Hz$	previous paper (2-electrode array)
$160Hz$	$128Hz - 192Hz$	
$200Hz$	$160Hz - 240Hz$	
$350Hz$	$300Hz - 410Hz$	this paper (4-electrode array)
$410Hz$	$350Hz - 480Hz$	
$480Hz$	$410Hz - 560Hz$	
$560Hz$	$480Hz - 660Hz$	
$660Hz$	$560Hz - 770Hz$	
$770Hz$	$660Hz - 900Hz$	
$900Hz$	$770Hz - 1050Hz$	
$1050Hz$	$900Hz - 1230Hz$	
$1230Hz$	$1050Hz - 1440Hz$	
$2000Hz$	$1700Hz - 2300Hz$	signal at this frequency may be corrupted
$3700Hz$	$3300Hz - 4000Hz$	signal at this frequency may be corrupted

Table 4.1: Frequencies at which the normalized amplitudes of the Stoneley-wave-induced electrical potentials were calculated from the field data, and the band-pass filters used in these calculations.

Parameter	Value
Stoneley wave velocity c_s	$1400m/s$
borehole radius R_b	$0.15m$
fluid conductivity σ_f	$0.022S/m$
fluid viscosity μ	$10^{-3}Pa \cdot s$
fluid permittivity ϵ_f	$7.1 \cdot 10^{-10}coul^2/(N \cdot m^2)$
rock conductivity σ_r	$0.015S/m$
fracture tortuosity α_∞	1
zeta potential ζ	$-60mV$

Table 4.2: Parameters of the rock formation and the borehole fluid used for calculating the synthetic amplitude-versus-frequency dependence for the Stoneley-wave-induced electrical potentials.

Chapter 5

Conclusions

In this thesis we investigated the electrical fields induced by borehole Stoneley waves. We developed an experimental procedure and a noise-reduction processing that allows measurements of this electroseismic phenomenon. Using this procedure, we made borehole electroseismic measurements in fractured igneous rocks and in sedimentary rocks. In the full-waveform electroseismic data, we identified the Stoneley-wave-induced electrical fields. Analysis of these electrical fields showed that they were induced by the Stoneley-wave-generated fluid flow in a formation around a borehole.

From the field data we derive a parameter that describes local electroseismic coupling at each depth. This parameter is the normalized amplitude of the Stoneley-wave-induced electrical field. We defined this normalized amplitude as a ratio of the amplitude of the electrical field oscillation at a certain depth to the amplitude of the pressure oscillation at this depth. Analysis of the experimental results demonstrated that:

1. In granite, the normalized amplitudes of Stoneley-wave-induced electrical fields correlate with the fracture density log.

2. In dolomite, the normalized amplitudes of the Stoneley-wave-induced electrical fields correlate with the porosity of the formation.

3. In dolomite, the Stoneley-wave-induced electrical field have anomalously high amplitudes at the isolated fracture that intersects boreholes T1 and T2.

4. In all experiments, the normalized amplitudes of the Stoneley-wave-induced electrical fields are sensitive to lithology.

To understand what specific information about permeable zones can be derived from borehole electroseismic measurements, we developed a Biot-theory-based model for the Stoneley-wave-induced electrical fields. The amplitudes of these electrical fields predicted by the theoretical model agreed with the amplitudes measured in field experiments in granite and dolomite.

According to the theoretical model, the normalized amplitude of the Stoneley-wave-induced electrical fields is proportional to the porosity of a formation around a borehole. In the dolomite experiment, the normalized amplitudes of the Stoneley-wave-induced electrical fields correlated with porosity logs. Thus, the theoretical model is consistent with the results of field experiments. Based on this result, we concluded that in the Hamilton experiment the normalized electroseismic amplitude was sensitive to the fracture porosity averaged over the Stoneley wave length. We used the theoretical model to derive a fracture porosity log for the granite section. This derivation yielded reasonable values for fracture porosity in granite, and the porosity log correlated with the fracture density log.

The theoretical model also predicts that the normalized amplitude of the Stoneley-wave-induced electrical field is inversely proportional to the pore space tortuosity. This result explains the anomalously high amplitudes of the Stoneley-wave-induced electrical fields at the isolated fracture that intersects boreholes T1 and T2. Fracture

tortuosity is close to 1 (Brown *et al.*, 1998). At the same time, in an isotropic porous formation the tortuosity is at least 3. Moreover, in a formation with large pores connected with narrow throats, tortuosity can be much higher. Thus, a Stoneley wave generates stronger electrical fields at a fracture than in an isotropic porous formation.

Further, the theoretical model predicted that the normalized amplitudes of the Stoneley-wave-induced electrical fields are sensitive to lithology and the fluid type through the zeta-potential. This result can explain why in the Hamilton experiment we measured much higher normalized electroseismic amplitude in granite than in diorite.

Finally, the theoretical model predicts that the amplitude-versus-frequency dependence of the Stoneley-wave-induced electrical fields depends on the permeability. To test this prediction of the theoretical model, we developed an experimental technique for broadband logging-type measurements of the Stoneley-wave-induced electrical potential. Using this experimental technique we made borehole electroseismic measurements in the frequency range from $300Hz$ to $4000Hz$. The normalized amplitude of the Stoneley-wave-induced electrical potential identified a large fracture intersected by the borehole.

From the field data we derived the normalized amplitudes of the Stoneley-wave-induced electrical potential at different frequencies. We compared the amplitude-versus-frequency dependence of the Stoneley-wave-induced electrical potentials recorded in the field with the predictions of the theoretical model. From this comparison we found that the theoretical model predicts the correct amplitudes for the electrical potentials induced by the Stoneley wave. Also, the amplitude-versus-frequency dependence of the electroseismic signals recorded at the depth of the large fracture roughly follows the trend predicted by the theory. However, the general amplitu-

de-versus-frequency dependence of the electroseismic signals recorded in the field is more complicated than that predicted by the theory. This can be attributed to (a) imperfection of the measurement devices; (b) failure of the theoretical model to correctly describe the phenomenon observed in the field; or (c) the presence of some other electroseismic phenomenon that we do not account for. Further measurements with a better data acquisition system and a better measurement tool are necessary to establish the complete physics of the electroseismic phenomenon that we observed in the field.

5.1 Suggestions for future work

This thesis is a first step towards understanding borehole electroseismic phenomena. Naturally, it leaves many question unanswered and provides a lot of room for improvement. Below is a list of questions that need to be investigated in more detail:

1. In our experiments we attempted to measure the amplitude-versus-frequency dependence of the Stoneley-wave-induced electrical fields. It is necessary to make better measurements in order to determine whether permeability can indeed be deduced from the amplitude-versus-frequency behavior of the electroseismic signals.

2. In this thesis we interpreted our experimental results based on the model that was derived for a homogeneous medium. Prior to use electroseismic phenomena in practice, it is necessary to develop theoretical models for borehole electroseismic phenomena in heterogeneous media and in fractured (anisotropic) media. Also, to determine how borehole electroseismic measurements can be used to characterize fractures, it is necessary to develop a theoretical model for electroseismic phenomena caused by a Stoneley wave at an isolated fracture.

3. Electroseismic measurements in fractured igneous rocks and in sedimentary rocks show that a Stoneley wave generates electromagnetic radiation at fractures. This phenomenon has not been investigated in this thesis. However, it may provide a new way for detecting and characterizing fractures intersected by a borehole. Moreover, measurements of the electromagnetic radiation generated by seismic waves may be used to detect interfaces and fractures that are at some distance from a borehole.

4. Theoretical studies (Pride and Haartsen, 1996; Haartsen and Pride, 1997) show that seismic waves generate magnetic fields. We believe that it is necessary to make field measurements of magnetic fields induced by seismic waves and to determine what information about the subsurface can be deduced from these measurements. The additional motivation for investigating magnetoseismic phenomena is that the signal-to-noise ratio in magnetoseismic experiments may be better than in the electroseismic experiments.

Bibliography

Antsyferov, M. S. (1958). Laboratory simulation of the seismo-electric effect of the second kind. *Dokl. Akad. Nauk SSSR*, **121**(5), 825.

Antsyferov, M. S. (1966). *The electroseismic effect in rocks*, pages 131–134. New-York Consultants Bureau.

Armbruster, H., Brauns, J., Mazur, W., and Merkler, G.-P. (1989). *Effects of leaks in dams and trials to detect leakages by geophysical means*, pages 133–144. Springer-Verlag.

Berlin, T. S. and Khabakov, A. V. (1961). Difference in the electrokinetic potentials of carbonate sedimentary rocks of different origin and composition. *Geochemistry*, **3**, 217–230.

Bernabe, Y. (1998). Streaming potential in heterogeneous networks. *submitted to J. Geoph. Res.*

Biot, M. A. (1941). General theory of three-dimensional consolidation. *J. Applied Phys.*, **12**, 155–164.

Biot, M. A. (1956a). Theory of propagation of elastic waves in a fluid-saturated porous solid. I. Low-frequency range. *J. Acoust. Soc. Am.*, **28**, 168–178.

Biot, M. A. (1956b). Theory of propagation of elastic waves in a fluid-saturated porous solid. II. High-frequency range. *J. Acoust. Soc. Am.*, **28**, 179–191.

Biot, M. A. (1962). Mechanics of deformation and acoustic propagation in porous media. *J. Applied Phys.*, **33**, 1482–1498.

Biot, M. A. and Willis, D. G. (1957). The elastic coefficients of the theory of consolidation. *J. Applied Mech.*, **24**, 594–601.

Bockris, J. and Reddy, A. K. N. (1970). *Modern electrochemistry*. Plenum Press.

Bourbie, T., Coussy, O., and Zinsner, B. (1987). *Acoustics of porous media*. Gulf Publishing Co., Houston.

Broding, R. A., Buchanan, S. D., and Hearn, D. P. (1963). Field experiments on the electroseismic effect. *IEEE Trans. Geosci. Electronics*, **GE-1**(1), 23–31.

Brown, S., Caprihan, A., and Hardy, R. (1998). Experimental observation of fluid flow channels in a single fracture. *J. Geoph. Res.*, **103**, 5125–5132.

Butler, K. E. and Russell, R. D. (1993). Subtraction of powerline harmonics from geophysical records. *Geophysics*, **58**(6), 989–903.

Butler, K. E., Russell, R. D., Kepic, A. W., and Maxwell, M. (1994). Mapping of a stratigraphic boundary by its seismoelectric response. In *Proceedings, SAGEEP*, pages 689–699.

Butler, K. E., Russell, R. D., Kepic, A. W., and Maxwell, M. (1996). Measurement of the seismoelectric response from a shallow boundary. *Geophysics*, **61**, 1769–1778.

Chandler, R. (1981). Transient streaming potential measurements on fluid-saturated porous strructures: An experimental verification of biot's slow wave in the quasi-static limit. *J. Acoust. Soc. Am.*, **70**(1), 116–121.

Chandler, R. N. (1984a). System for permeability logging by measuring streaming potential. *Canadian Patent 1,178,658*.

Chandler, R. N. (1984b). System for permeability logging by measuring streaming potentials. *U. S. Patent 4,427,944*.

Chernyak, G. Y. (1975). Direct and inverse seismoelectric effect in sedimentary rocks under sinusoidal excitation. *Izv. Acad. Sci. USSR, Physics of the Solid Earth*, **7**, 117–121.

Chernyak, G. Y. (1976). The physical nature of the seismoelectric effect in rocks. *Izv. Acad. Sci. USSR, Physics of the Solid Earth*, **2**, 108–112.

Chien-San, C. and Zangirov, R. S. (1965). On the seismoelectric effect of the second kind in dispersed soils. *Izv. Acad. Sci. USSR, Physics of the Solid Earth*, **3**, 76–79.

CRC (1978). *CRC handbook of chemistry and physics*. CRC Press.

Davis, S. N. and DeWeist, R. J. M. (1966). *Hydrogeology*. John Wiley and Sons, Inc.

Desbrandes, R. (1985). *Encyclopedia of well logging*. Gulf Publishing Company.

Dobos, D. (1975). *A handbook for electrochemists in industry and universities*. Elseiver.

Doll, H.-G. (1947). Method and apparatus for investigating earth formations traversed by boreholes. *U. S. Patent 2,433,746*.

Doll, H.-G. (1949). Well logging equipment. *U. S. Patent 2,475,354*.

Doll, H.-G. (1951). Well logging method and apparatus utilizing periodically variable spontaneous potentials. *U. S. Patent 2,550,005*.

Doll, H.-G. (1957). Methods for logging the formations traversed by a borehole. *U. S. Patent 2,814,017*.

Duckworth, H. E. (1960). *Electricity and Magnetism*. Holt, Rinehart and Winston, New York.

Frenkel, J. (1944). On the theory of seismic and seismoelectric phenomena in a moist soil. *Journal of Physics (Soviet)*, **8**(4), 230–241.

Gaskarov, I. V. and Parkhomenko, E. I. (1974). The seismoelectric effect in rocks and the preconditions for its application in geological prospecting work. *Izv. Acad. Sci. USSR, Physics of the Solid Earth*, **1**, 110–115.

GEOSS (1984a). *Description of the cuttings and cores from the B-series holes in Totten Property, South Hamilton, Massachusetts.* Geophysical Services of Salem.

GEOSS (1984b). *Description of the cuttings from well 2 in Totten Property, South Hamilton, Massachusetts.* Geophysical Services of Salem.

Gurevich, B. and Lopatnikov, S. L. (1995). Velocity and attenuation of elastic waves in finely layered porous rocks. *Geoph. J. Int.*, **121**, 933–947.

Haartsen, M. W. (1995). *Coupled electromagnetic and acoustic wavefield modeling in poro-elastic media and its applications in geophysical exploration.* Ph.D. thesis, Massachusetts Institute of Technology.

Haartsen, M. W. and Pride, S. R. (1997). Electroseismic waves from point sources in layered media. *J. Geoph. Res.*, **102**, 24,745–24,769.

Haartsen, M. W., Zhu, Z., and Toksöz, M. N. (1995). Seismoelectric experimental data and modeling in porous layer models at ultrasonic frequencies. In *Expanded Abstracts, 65th Ann. Internat. Mtg.*, pages 26–29. Soc. Expl. Geophys.

Haartsen, M. W., Dong, W., and Toksöz, M. N. (1998). Dynamic streaming currents from seismic point sources in homogeneous poroelastic media. *Geoph. J. Int.*, **132**, 256–274.

Hadley, K. (1976). Comparison of calculated and observed crack densities and seismic velocities in Westerly granite. *J. Geoph. Res.*, **81**(20), 3484–3494.

Haley and Aldrich, Inc. (1990). *Report on Hydrogeological Evaluation of a Bedrock Well System in Hamilton, Massachusetts*. Haley and Aldrich, Inc.

Hashimoto, T. and Tanaka, Y. (1995). A large self-potential anomaly on Unzen volcano, Shimabara peninsula, Kyushu island, Japan. *Geoph. Res. Lett.*, **22**(3), 191–194.

Hilchie, D. W. (1978). *Applied openhole log interpretation (for geologists and petroleum engineers)*. Douglas W. Hilchie, Inc.

Ivanov, A. G. (1939). Effect of electrization of earth layers by elastic waves passing through them (in russian). *Doklady Akademii Nauk SSSR*, **24**(1), 41–43.

Ivanov, A. G. (1940). The electroseismic effect of the second kind. *Izvestiya Akademii Nauk SSSR, Ser. Geogr. Geofiz.*, **5**, 699–727.

Ivanov, A. G. (1961). Method of geophysical investigations of rocks which are perforated by boreholes. *Russian Patent 140,502*.

Johnson, D. L., Koplik, J., and Dashen, R. (1987). Theory of dynamic permeability and tortuosity in fluid-saturated porous media. *J. Fluid Mech.*, **176**, 379–400.

Jouniaux, L. and Pozzi, J.-P. (1995). Permeability dependence of streaming potentials in rocks for various fluid conductivities. *Geoph. Res. Lett.*, **22**(4), 485–488.

Kostek, S., Johnson, D. L., Winkler, K. W., and Hornby, B. E. (1998). The interaction of tube waves with borehole fractures, Part ii: Analytical models. *Geophysics*, **63**, 809–815.

Kuster, G. T. and Toksöz, M. N. (1974). Velocity and attenuation of seismic waves in two-phase media: Part I. Theoretical formulations. *Geophysics*, **39**, 587–606.

Landau, L. D. and Lifshitz, E. M. (1959). *Fluid Mechanics*. Pergamon Press.

Li, S. X., Pengra, D. B., and Wong, P.-Z. (1995). Onsager's reciprocal relationship and the hydraulic permeability of porous media. *Phys. Rew. B*, **51**(6), 5748–5751.

Lockner, D. A. and Byerlee, J. D. (1985). Complex resistivity measurements of confined rocks. *J. Geophys. Res.*, **90**, 7837–7847.

Martner, S. T. and Sparks, N. R. (1959). The electroseismic effect. *Geophysics*, **24**(2), 297–308.

Migunov, N. I. and Kokorev, A. A. (1977). Dynamic properties of the seismoelectric effect of water-saturated rocks. *Izv. Acad. Sci. USSR, Physics of the Solid Earth*, **13**(6), 443–446.

Migunov, N. I., Kokorev, A. A., and Miller, V. V. (1993). Change of the seismoelectric effect of rocks subjected to neutron radiation. *Dokl. Akad. Nauk SSSR*, **332**(6), 780–782.

Migunov, N. I., Kokorev, A. A., and Miller, V. V. (1995). Change in the seismoelectric effect in gamma-irradiated rocks. *Dokl. Akad. Nauk SSSR*, **345**(5), 678–681.

Mikhailov, O. V., Haartsen, M. W., and Toksöz, M. N. (1997). Electroseismic investigation of the shallow subsurface: field measurements and numerical modeling. *Geophysics*, **62**, 97–105.

Mironov, S. A., Parkhomenko, E. I., and Chernyak, G. Y. (1993). Seismoelectric effects of rocks saturated with gas or liquid hydrocarbons. *Izv. Acad. Sci. USSR, Physics of the Solid Earth*, **11**, 70–76.

Mizutani, H., Ishido, T., Yokokura, T., and Ohnishi, S. (1976). Electrokinetic phenomena associated with earthquakes. *Geophys. Res. Lett.*, **3**, 365–368.

Morgan, F. D. (1989). *Fundamentals of streaming potentials in geophysics: laboratory methods*, pages 133–144. Springer-Verlag.

Morgan, F. D., Williams, E. R., and Madden, T. R. (1989). Streaming potential properties of Westerly granite with applications. *J. Geoph. Res.*, **94**, 12449–12461.

Neev, J. and Yeatts, F. R. (1989). Electrokinetic effects in fluid-saturated poroelastic media. *Phys. Rev. B*, **40**, 9135–9141.

Neyshtadt, N. M. and Osipov, L. N. (1959). Experimental studies of the electroseismic *e*-effect (in russian). *Trans. VITR*, **12**, 57–75.

Nur, A. M. (1969). *Effect of stress and fluid inclusions on wave propagation in rocks.* Ph.D. thesis, Massachusetts Institute of Technology.

O'Connel, R. and Budiansky, B. (1977). Viscoelastic properties of fluid-saturated cracked solids. *J. Geoph. Res.*, **82**(36), 5719–5735.

Olhoeft, G. R. (1985). Low-frequency electrical properties. *Geophysics*, **50**(12), 2492–2503.

Packard, R. G. (1953). Streaming potentials across glass capilaries for sinusoidal pressure. *J. Chem. Physics*, **21**(2), 303–307.

Paillet, F. L. (1997). Borehole geophysics used to characterize vertical fractures and their connections to bedding plane aquifers in dolomite. In *Proceedings, SAGEEP*, pages 195–203.

Paillet, F. L., Hess, A. E., and Williams, J. H. (1998). A wireline packer for hydraulic reconnaissance in open boreholes. *Unpublished report*, **1**, 1–43.

Parkhomenko, E. I. and Gaskarov, I. V. (1971). Borehole and laboratory studies of the seismoelectric effect of the second kind in rocks. *Izv. Akad Nauk SSSR, Physics of the Solid Earth*, **9**, 88–92.

Parkhomenko, E. I. and Topchian, H. D. (1994). Influence of a highly conductive component on the magnitude of the seismoelectric effect. *Izv. Acad. Sci. USSR, Physics of the Solid Earth*, **7**, 156–161.

Parkhomenko, E. I. and Tsze-San, C. (1964). A study of the influence of moisture on the magnitude of the seismoelectric effect in sedimentary rocks by a laboratory method. *Izv. Akad. Nauk SSSR, Geophys. Ser.*, **2**, 206–212.

Parkhomenko, E. I., Gaskarov, I. V., and Marmorshteyn, L. M. (1975). Relationship between the magnitude of the seismoelectric effect in sandstones and their permeability. *Dokl. Akad. Nauk SSSR*, **223**(5), 1110–1111.

Parkhomenko, E. I., Tonoian, T. V., and Topchian, H. D. (1986). The relationship between the magnitude of the seimsoelectric effect in rocks and temperature (in russian). *Izv. Akad. Nauk Armyanskoi SSR, Nauki o Zemle*, **39**(4), 48–53.

Pengra, D. B., Shi, L., Li, S. X., and Wong, P.-Z. (1995). Experimental study of electrokinetics in porous media. In *MRS Conference proceedings, vol. 366*, pages 201–206. Material Research Society.

Plona, T. J. (1980). Observations of a second bulk compressional wave in a porous medium at ultrasonic frequencies. *Appl. Phys. Lett.*, **36**, 259–261.

Pride, S. R. (1994). Governing equations for the coupled electromagnetics and acoustics of porous media. *Phys. Rev. B*, **50**, 15678–15696.

Pride, S. R. and Haartsen, M. W. (1996). Electroseismic wave properties. *J. Acoust. Soc. Am.*, **100**, 1301–1315.

Reppert, P. M. and Morgan, F. D. (1998). Laboratory study of frequency-dependent streaming potentials. (submitted). In *68th Ann. Internat. Mtg.* Soc. Expl. Geophys.

Russel, R. D., Butler, K. E., Kepic, A. W., and Maxwell, M. (1997). Seismoelectric exploration. *The Leading Edge*, **16**, 1611–1615.

Schlumberger (1972). *Log Interpretation*. Schlumberger Ltd.

Schmitt, D. P. (1986). Full wave synthetic acoustic logs in saturated porous media. Part I. A review of biot theory. *ERL Consortium Report*, **1986**(5), 1–69.

Semmelink, A. (1971). Apparatus for well logging measuring and comparing potentials caused by sonic excitation. *U. S. Patent 3,599,085*.

Simonyan, S. S. (1985). A study of the character of the seismoelectric effect depending on the state of stress of a fluid saturated porous rock. *Izv. Akad. Nauk Armyanskoi SSR, Nauki o Zemle*, **38**(2), 75–78.

Simonyan, S. S. (1987). Relationship between the magnitude of the seismoelectric effect and uniaxial stress of samples saturated with nacl solutions (in russian). *Izv. Akad. Nauk Armyanskoi SSR, Nauki o Zemle*, **40**(3), 56–59.

Skokan, C. K. and Chi, D. (1990). Use of the seismo-electric effect in engineering problems. In *Proceedings, 1990 SAGEEP Annual Meeting*, pages 341–347.

Sprunt, E. S., Mercer, T. B., and Djabbarah, N. F. (1994). Streaming potential from multiphese flow. *Geophysics*, **59**, 707–711.

Tang, X. and Cheng, C. H. (1993). Borehole Stoneley wave propagation across permeable structures. *Geophysical Prospecting*, **41**, 165–187.

Tang, X., Cheng, C. H., and Toksöz, M. N. (1991). Dynamic permeability and borehole Stoneley waves: A simplified Biot-Rosenbaum model. *J. Acoust. Soc. Am.*, **90**(3), 1632–1646.

Thompson, A. H. (1990). Electroseismic prospecting by detection of an electromagnetic signal produced by dipolar movement. *U. S. Patent 4,904,942*.

Thompson, A. H. and Gist, G. A. (1993). Geophysical applications of electrokinetic conversion. *The Leading Edge*, **12**, 1169–1173.

Toksöz, M. N., Cheng, C. H., and Timur, A. (1976). Velocities of seismic waves in porous rocks. *Geophysics*, **41**, 621–645.

Tome, R. F. (1975). *Studies on the seismoelectric effect*. Master's thesis, University of Toronto.

Winkler, K. W., Liu, H., and Johnson, D. L. (1989). Permeability and borehole Stoneley waves: Comparison between experiment and theory. *Geophysics*, **54**, 66–75.

Wolfe, P. J., Yu, J., and Gershnzon, N. (1996). Seismoelectric studies in an outwash plain. In *Proceedings, SAGEEP*, pages 21–30.

Wong, P.-Z. (1995). Determination of permeability of porous media by streaming potential and electro-osmotic coefficients. *U.S. Patent 5,417,104*.

Wurmstich, B. and Morgan, F. D. (1994). Modeling of streaming potential responses caused by oil well pumping. *Geophysics*, **59**(1), 45–56.

Zablocki, C. J. and Keller, G. V. (1961). Some observations of the seismic-electric effect. *U.S. Geolog. Survey Profess. Paper*, **Paper 424-D**, D296–D299.

Zhu, Z. and Toksöz, M. N. (1996). Experimental studies of electrokinetic conversion in fluid-saturated porous medium. In *Expanded Abstracts, 66th Ann. Internat. Mtg.*, pages 1699–1702. Soc. Expl. Geophys.

Zhu, Z. and Toksöz, M. N. (1997). Experimental studies of electrokinetic conversions in fluid-saturated borehole models. In *Expanded Abstracts, 67th Ann. Internat. Mtg.*, pages 334–337. Soc. Expl. Geophys.

Zhu, Z. and Toksöz, M. N. (1998). Seismoelectric measurements in a fractured borehole model. In *Expanded Abstracts, 68th Ann. Internat. Mtg.* Soc. Expl. Geophys.

Zhu, Z., Cheng, C., and Toksöz, M. N. (1994). Electroseismic conversion in a fluid saturated porous rock sample. In *Expanded Abstracts, 64th Ann. Internat. Mtg.*, pages 26–29. Soc. Expl. Geophys.

Appendix A

Analysis of the electrical signals generated by the Stoneley wave's action on the electrodes or on the borehole wall

We argue that the Stoneley-wave-induced electrical fields measured in our experiments were generated by fluid flow within fractures. To support this argument, we demonstrate that these electrical fields could not have been generated within the borehole. Specifically, we show that the action of the Stoneley wave on the electrodes and the streaming potentials due to the fluid motion along the borehole wall generate electrical fields with amplitudes that are several orders of magnitude smaller than those measured in our experiments (Figure 2-8).

A.1 Electrical signals due to the electrode motion induced by the Stoneley wave

When a Stoneley wave propagates past the electrodes, it causes the electrodes to move. In the borehole there is a DC electrical field associated with the spontaneous potential (SP). When the electrodes move in this external electrical field, their electrical potential changes, and therefore the data acquisition system records an electrical signal caused by this electrode motion. To estimate the amplitude of the electrical signal caused by the electrode motion, we assume the worst case scenario, that the electrodes move together with the fluid. For the central frequency in the experiment $f_c = 150Hz$, the Stoneley wave velocity $c_s = 1400m/s$, the Stoneley wave pressure amplitude $P_0 = 1000Pa$ (Figure 2-8), and the bulk modulus of water, $K_f = 2.2 \cdot 10^9 Pa$, the fluid displacement, u_z, caused by the Stoneley wave is less than

$$u_z < \frac{c_s}{f_c} \cdot \frac{2P_0}{K_f} = 8.5 \cdot 10^{-6} m. \tag{A.1}$$

The external DC electrical field, E_{ext}, in the experiments was less than $10mV/m$. The change of the electrode's potential, Φ, due to its motion in this electrical field is less than:

$$(\Delta\Phi)_{motion} = u_z \cdot E_{ext} < 8.5 \cdot 10^{-8} V = 0.085\mu V \tag{A.2}$$

At the same time, the Stoneley-wave-induced electrical signals recorded in field experiments have amplitudes around $10\mu V$, which is two orders of magnitude larger. We therefore conclude that the electroseismic phenomena observed in the experiments were not caused by electrode motion.

A.2 Streaming potentials due to the fluid motion along the borehole wall

Similar to pore surfaces, the rock surface of the borehole adsorbs negative electrical ions from the borehole fluid (water), leaving an excess positive electrical charge in the borehole fluid. This electrical charge is concentrated in a thin layer along the surface of the borehole. When a Stoneley wave propagates along the borehole, it moves the fluid along the borehole wall, thus creating a streaming electrical current. The analysis below shows that the electrical field induced by the fluid motion along the borehole wall is several orders of magnitude smaller than the Stoneley-wave-induced electrical field measured in the experiments.

Packard (1953) obtained an analytical solution for the streaming potential in capillaries under sinusoidal pressure. In our notation (defined in Chapter 3) Packard's solution can be written as:

$$\Phi = P_b \cdot \frac{\zeta \epsilon_f}{4\pi\sigma_f \mu} \left(\frac{2}{\gamma R_b} \right) \frac{J_1(\gamma R_b)}{J_0(\gamma R_b)}. \tag{A.3}$$

In Equation A.3, J_0 and J_1 are the zero and first-order Bessel functions, and

$$\gamma = \left(\frac{i\rho_f \omega}{\mu} \right)^{\frac{1}{2}}. \tag{A.4}$$

The borehole Stoneley wave in the experiment can be viewed as a sinusoidal pressure disturbance propagating in a capillary (the borehole). Thus, we can directly apply Packard's solution to estimate the amplitude of the streaming electrical potential induced by the fluid motion along the borehole wall. An equation for the electrical field along the borehole can be derived from Equation A.3 by spatial differentiation of the electrical potential along the borehole axis ($\underline{E} = -\nabla\Phi$). Using Equation 3.1 for

the spatial and time dependence of the fluid pressure P_b in the borehole, we obtain:

$$\frac{E_z}{P_b} = \frac{\zeta \epsilon_f}{4\pi \sigma_f \mu} \left(\frac{2}{\gamma R_b} \right) \frac{J_1(\gamma R_b)}{J_0(\gamma R_b)} \left(-\frac{i\omega}{c_s} \right). \tag{A.5}$$

For the granite section of the well we know the values for all the parameters in Equations A.4 and A.5, including the zeta-potential (Table 3.1). Substitution of these values in Equations A.4 and A.5 gives the value for the E/P ratio of $4.5 \cdot 10^{-11} V/(m \cdot Pa) = 4.5 \cdot 10^{-2} nV/(m \cdot Pa)$. This value is two orders of magnitude smaller than the normalized amplitudes of the Stoneley-wave-induced electrical fields measured in the granite section of the well (Figure 2-8). Therefore, the electrical fields measured in field experiments were not generated by the streaming potentials caused by fluid motion along the borehole wall.

A.3 Streaming potentials due to the fluid motion along the surface of the electrodes

When a Stoneley wave propagates past the electrodes, it generates fluid motion along the surface of the electrodes. Similar to the surface of the rock, the hydro-oxidized surface of lead electrodes adsorbs ions of a certain polarity from water, leaving an excess of ions of the opposite polarity in the water in the vicinity of the electrode surfaces. For lead in water Dobos (1975) provides a value for the zeta-potential of $\zeta_{lead} = 18mV$, without specifying the salinity or conductivity of the water in which it was measured. Note that the positive sign of the zeta-potential suggests that the surface of lead in water adsorbs positive ions. We can use this value of the zeta-potential to obtain a rough estimate of the streaming potential created by fluid motion along the surface of lead electrodes.

At the frequency of the Stoneley wave in the experiment, $f_c = 150Hz$, the thick-

ness of the viscous boundary layer in water,

$$\delta = \sqrt{\frac{\mu}{\rho_f 2\pi f_c}} = 3.3 \cdot 10^{-5} m, \tag{A.6}$$

is much less than the radius of the electrodes, $R_{el} = 0.01m$, and the radius of the borehole, $R_b = 0.15m$. Therefore, the Stoneley-wave-generated fluid flow along the electrode surface is similar to the geometry of the fluid flow along the borehole wall. Thus, we can use a slightly modified Equation A.5 to estimate the normalized amplitude of the electrical field induced by the streaming electrical current along the electrode surface. To estimate this normalized amplitude, we (a) use the value of the zeta-potential for lead in water in Equation A.5, and (b) multiply Equation A.5 by $\frac{R_{el}}{R_b}$ to account for the difference in the total surface area of the electrodes and the borehole. The resulting estimate of the normalized amplitude induced by the streaming electrical current along the electrode surface is $\frac{E}{P} = 9.0 \cdot 10^{-13} V/(m \cdot Pa) = 9.0 \cdot 10^{-4} nV/(m \cdot Pa)$. This value is four orders of magnitude smaller than the normalized amplitudes of the Stoneley-wave-induced electrical fields measured in the experiment (Figure 2-8). Therefore, the electrical fields measured in the experiments were not generated by the streaming potentials caused by the fluid motion along the electrodes.

Appendix B

Solution for the amplitude and phase of the Stoneley-wave-induced electrical field

We start the theoretical analysis with Maxwell's equations. A comparison of the relative magnitude of the terms in the equations shows that, at the frequencies and spatial scales of the experiments, the terms containing differentiation with respect to time can be neglected. Thus, Maxwell's equations reduce to the quasi-electrostatic equations for a conductive medium:

$$\nabla \cdot \underline{j} = 0 \tag{B.1}$$

$$\nabla \times \underline{E} = 0. \tag{B.2}$$

Field data shows that, at the sensitivity level of the measurements, electromagnetic waves were detected only in rare instances. At the same time, the electrical fields locally induced by a Stoneley wave were very clear in the field data. Therefore, the field data support the validity of neglecting the "radiative" terms (i.e., the terms

containing differentiation with respect to time) in Maxwell's equations.

Equation B.2 allows introduction of the electrical potential:

$$\underline{E} = -\nabla\Phi. \tag{B.3}$$

In the fluid filling the borehole, the electrical current density is determined by the fluid conductivity:

$$\underline{j} = \underline{j}_{conductive} = \sigma_f \underline{E}. \tag{B.4}$$

In the formation around the borehole, the electrical current density is the sum of the conductive and streaming current densities:

$$\underline{j} = \underline{j}_{conductive} + \underline{j}_{streaming} = \sigma_r \underline{E} - L\nabla P_f. \tag{B.5}$$

A combination of Equations B.3, B.4 and B.1 gives an equation for the electrical potential in the borehole:

$$\sigma_f \nabla^2 \Phi = 0. \tag{B.6}$$

Similarly, a combination of Equations B.3, B.5 and B.1 gives an equation for the electrical potential in the formation:

$$\sigma_r \nabla^2 \Phi = -L\nabla P_f. \tag{B.7}$$

An axisymmetric solution for Equations B.6 and B.7 that is finite at $r = 0$ and $r = \infty$ is

$$\Phi = A \frac{I_0\left(r\frac{\omega}{c_s}\right)}{I_0\left(R_b\frac{\omega}{c_s}\right)} \exp\left(-i\omega t + i\frac{\omega}{c_s}z\right), \qquad r < R_b \tag{B.8}$$

$$\Phi = -\frac{L}{\sigma_r}P_f + B\frac{K_0\left(r\frac{\omega}{c_s}\right)}{K_0\left(R_b\frac{\omega}{c_s}\right)} \exp\left(-i\omega t + i\frac{\omega}{c_s}z\right), \qquad r > R_b, \tag{B.9}$$

where pressure, P, is given by Equation 3.2, and coefficients A and B are to be determined from boundary conditions. Here I_0 and K_0 are the zero-order modified Bessel functions.

At the borehole wall, the electrical potential and the normal electrical current have to be continuous. These boundary conditions provide two equations for the coefficients A and B:

$$A = -\frac{L}{\sigma_r} P_0 + B, \tag{B.10}$$

$$-\sigma_f A \frac{\frac{\omega}{c_s} I_1\left(R_b \frac{\omega}{c_s}\right)}{I_0\left(R_b \frac{\omega}{c_s}\right)} = \sigma_r B \frac{\frac{\omega}{c_s} K_1\left(R_b \frac{\omega}{c_s}\right)}{K_0\left(R_b \frac{\omega}{c_s}\right)}. \tag{B.11}$$

Solving Equations B.10 and B.11 gives:

$$A = -\frac{LP_0}{\sigma_r + \sigma_f \frac{I_1\left(R_b \frac{\omega}{c_s}\right)}{I_0\left(R_b \frac{\omega}{c_s}\right)} \frac{K_0\left(R_b \frac{\omega}{c_s}\right)}{K_1\left(R_b \frac{\omega}{c_s}\right)}}, \tag{B.12}$$

$$B = \frac{LP_0}{\sigma_r} - \frac{LP_0}{\sigma_r + \sigma_f \frac{I_1\left(R_b \frac{\omega}{c_s}\right)}{I_0\left(R_b \frac{\omega}{c_s}\right)} \frac{K_0\left(R_b \frac{\omega}{c_s}\right)}{K_1\left(R_b \frac{\omega}{c_s}\right)}}. \tag{B.13}$$

Equations B.8 and B.9 together with B.12 and B.13 give the full solution for the electrical potential in and around the borehole. The vertical component of the electrical field can be obtained according to Equation B.3 by differentiating the expression for the electrical potential with respect to z:

$$E_z = \frac{-LP_0\left(-i\frac{\omega}{c_s}\right)}{\sigma_r + \sigma_f \frac{I_1\left(R_b \frac{\omega}{c_s}\right)}{I_0\left(R_b \frac{\omega}{c_s}\right)} \frac{K_0\left(R_b \frac{\omega}{c_s}\right)}{K_1\left(R_b \frac{\omega}{c_s}\right)}} \frac{I_0\left(r\frac{\omega}{c_s}\right)}{I_0\left(R_b \frac{\omega}{c_s}\right)} \exp\left(-i\omega t + i\frac{\omega}{c_s} z\right). \tag{B.14}$$

Finally, dividing Equation B.14 by Equation 3.1 gives the ratio of the electrical field to pressure in the borehole:

$$\frac{E_z}{P_b} = \frac{L\left(i\frac{\omega}{c_s}\right)}{\sigma_r + \sigma_f \frac{I_1\left(R_b \frac{\omega}{c_s}\right)}{I_0\left(R_b \frac{\omega}{c_s}\right)} \frac{K_0\left(R_b \frac{\omega}{c_s}\right)}{K_1\left(R_b \frac{\omega}{c_s}\right)}}. \tag{B.15}$$

This equation is a solution for a general streaming current coupling coefficient L. If L is expressed in terms of the rock properties (Equation 3.4), then the solution for the amplitude and phase of the Stoneley-wave-induced electrical field is complete.

Appendix C

Analysis of the mysterious electrical signal M-M

Electrical data in Figures 4-3—4-6 show an electrical signal M-M that appears to be "generated" at some depth in the borehole at the time of the source ($10ms$). This signal has a Stoneley wave moveout. Below, we analyze the origin of this mysterious signal.

The hydrophone data show that at the time when the signal was recorded, no wave was propagating past the electrode array. Therefore, we conclude that this signal was not recorded by the 4-electrode array.

Figure C-1 shows the two electrical datasets collected with sources at the depths of $30m$ and $35m$. We plotted these data next to each other, such that the traces measured at the same depths in the borehole match. Comparison shows that the mysterious Event M-M appears to be "generated" at different depths in the two datasets. Therefore, we conclude that this event does not correspond to any physical event taking place at some depth in the borehole.

Figure C-2 shows the same electrical datasets plotted next to each other, such that the traces recorded at the same offset from the source match. Comparison shows that the mysterious Event M-M appear to originate at the $14m$ offset from the source in both experiments. Based on this result we argue that this mysterious Event M-M was recorded by some fault in the cable that connected the electrode array with the data acquisition at the surface. This fault is $14m$ above the top electrode of the array. When the top electrode of the array is $14m$ below the source, the fault in the cable is at the source depth, thus event M-M is recorded at the source time ($10ms$). When the fault in the cable is below or above the source, the Stoneley wave propagating from the source acted on the fault and somehow generated an electrical signal in the cable. Thus, event M-M appears to have a Stoneley wave moveout.

Figure 4-7 presents the electrical data ($35m$ source depth, $2.5kHz$ source frequency) band-pass filtered in the interval from $300Hz$ to $1500Hz$. In these data the mysterious Event M-M is not visible. Figure 4-8 presents the same electrical data band-pass filtered in the interval from $1500Hz$ to $4000Hz$. In these data Event M-M is very clear. We suggest that the presence of event M-M does not compromise the validity of the measurements at frequencies below $1500Hz$. However, it makes us question whether the signals recorded at frequencies above $1500Hz$ were only partially due to the fluid flow generated in the formation by the Stoneley wave.

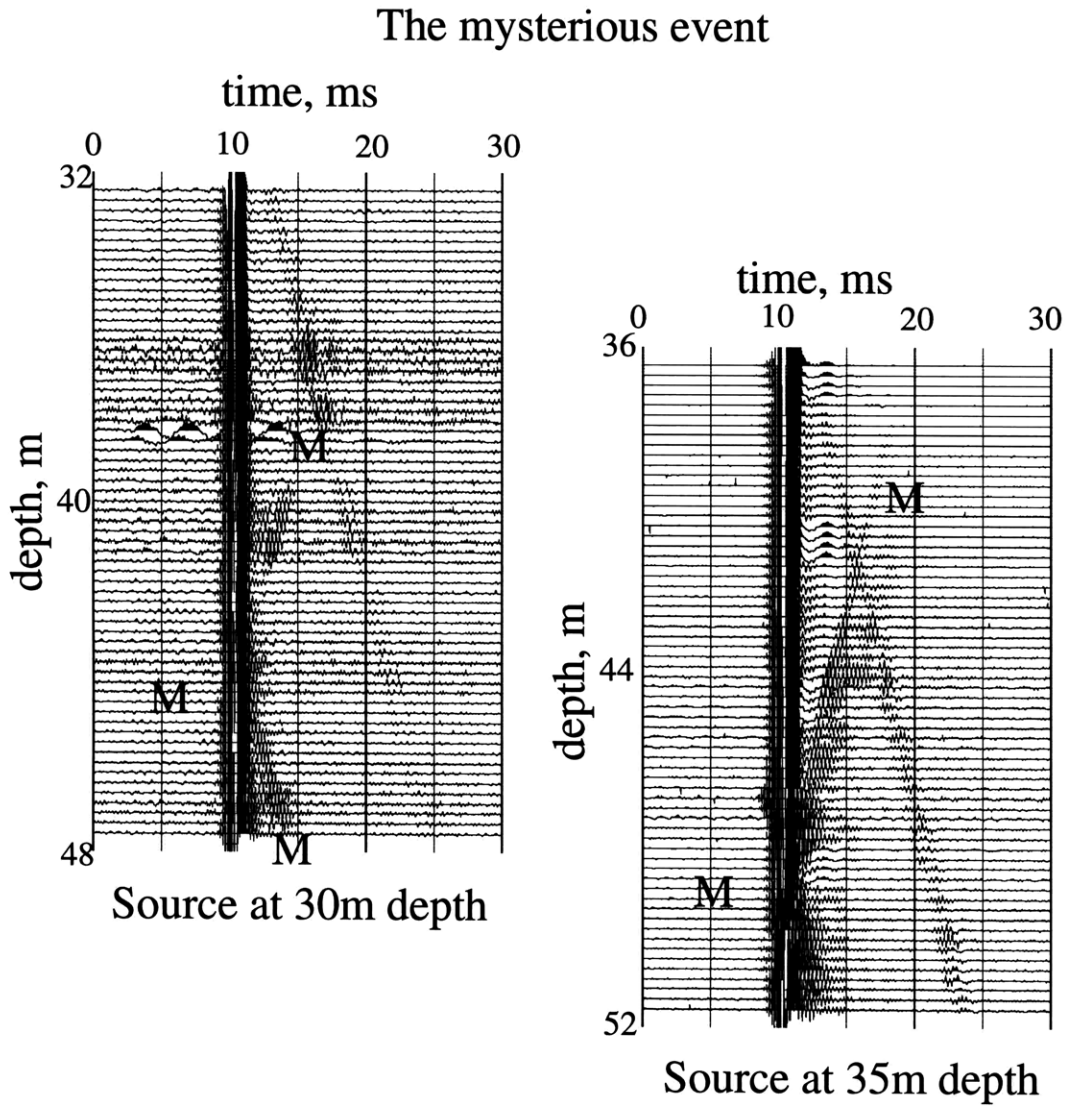

Figure C-1: Two electrical datasets (sources at the depths of $30m$ and $35m$) plotted such that the traces measured at the same depths in the borehole match. Comparison shows that the mysterious event M-M appears to be "generated" at different depths in the two datasets. Therefore, we conclude that this event does not correspond to any physical event taking place at some depth in the borehole.

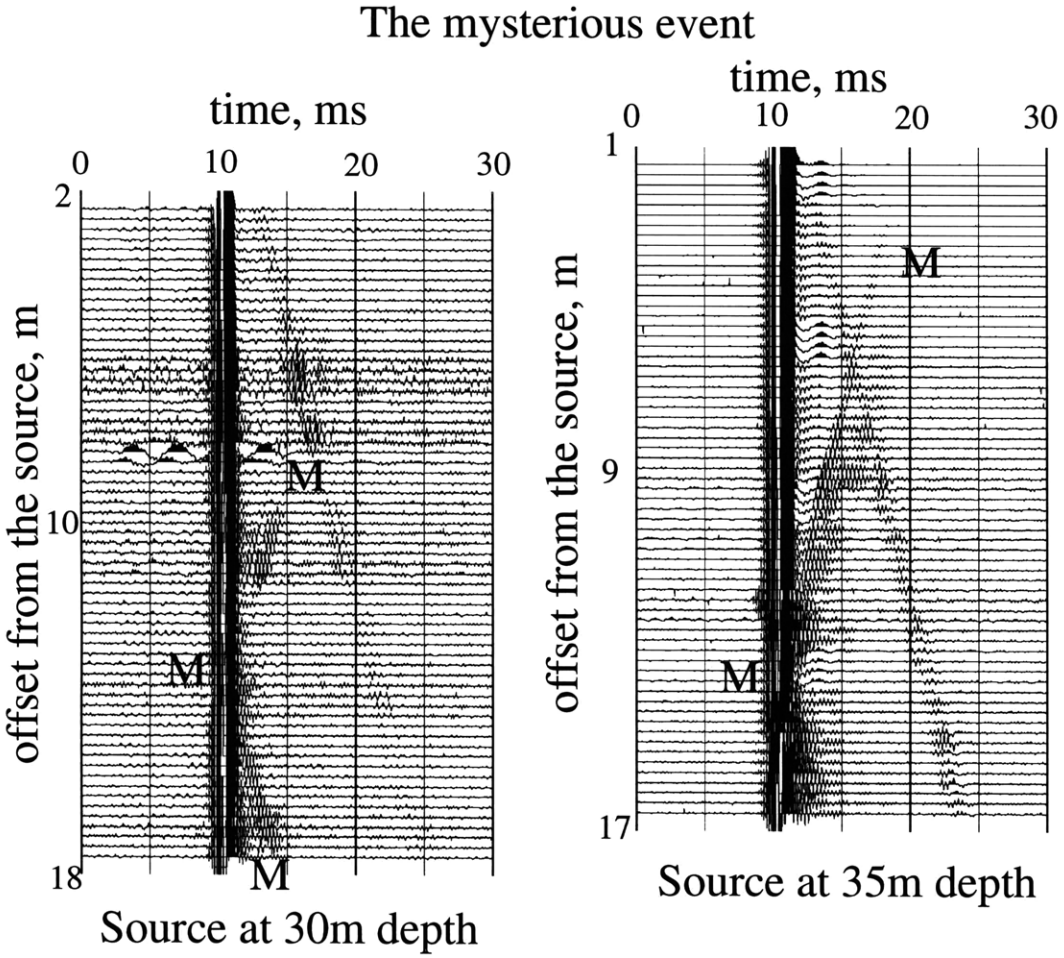

Figure C-2: Two electrical datasets (sources at the depths of $30m$ and $35m$) plotted such that the traces recorded at the same offset from the source match. Comparison shows that the mysterious Event M-M appears to originate at the $14m$ offset from the source in both experiments. Therefore, we conclude that this signal was generated by a fault in the cable that is $14m$ above the top electrode of the array.

Appendix D

Sensitivity functions of the 4 and 2-electrode measurements

D.1 Relationships between the amplitude of the electrical potential oscillation and the amplitudes of the signals measured using the 4-electrode array

The electrical signals presented in Figure 4-3 are measured using the 4-electrode array (Figure D-1). These signals are combinations of the electrical potential measured at 4 points in the borehole (Equation 4.1):

$$A_{4el} = (\Phi_a - \Phi_b) - (\Phi_c - \Phi_d)\,. \tag{D.1}$$

As we mentioned before, if the Stoneley wavelength is much larger than the distance between the electrodes, then the signal A_{4el} is proportional to the second derivative

of the electrical potential along the borehole axis.

To derive the relationship between the amplitude of the Stoneley-wave-induced electrical potential at some frequency ω to the amplitude of the measured signal at this frequency, $A_{4el}(\omega)$, we substitute a expression for the electrical potential induced by a Stoneley wave (Equation 3.13, simplified assuming that the Stoneley wave length is greater than the borehole radius R_b):

$$\Phi_b(z,t) = \Phi_0 \exp\left(-i\omega t + i\frac{\omega}{c_s}z\right) \tag{D.2}$$

into Equation D.1.

If we denote the distance between the electrodes as l, then the ratio of the signal A_{4el} measured by the 4-electrode array to the electrical potential at the first electrode Φ_a is:

$$\frac{A_{4el}}{\Phi_a}(\omega) = -4\sin\left(\frac{\omega}{c_s}l\right)\sin\left(\frac{\omega}{2c_s}l\right)\exp\left(i\frac{\omega}{c_s}l\right)\exp\left(i\frac{\omega}{2c_s}l\right), \tag{D.3}$$

and the amplitude ratio of the signal A_{4el} to the potential Φ_a at the electrode a is:

$$\frac{|A_{4el}|}{|\Phi_a|}(\omega) = 4\left|\sin\left(\frac{\omega}{c_s}l\right)\sin\left(\frac{\omega}{2c_s}l\right)\right|. \tag{D.4}$$

Equation D.4 shows that when the Stoneley wave length is twice the distance between the electrode l, the 4-electrode array records zero signal because the signal on the electrode a cancels the signal on the electrode c, and the signal on the electrode b cancels the signal on the electrode d. Similarly, when the Stoneley wave length is equal to the distance between the electrodes, then the 4-electrode array measures a zero signal because the signal on the electrode a cancels the signal on the electrode b, and the signal on the electrode c cancels the signal on the electrode d. Figure D-2 presents the sensitivity function $\frac{|A_{4el}|}{|\Phi_a|}(\omega)$ of the 4-electrode measurement with a $0.5m$ spacing between the electrodes. Zeros of the sensitivity function $\frac{|A_{4el}|}{|\Phi_a|}(\omega)$ correspond to the frequencies at which the distance between the electrodes is a multiple of half of a Stoneley wavelength.

D.2 Relationships between the amplitude of the electrical potential oscillation and the amplitudes of the signals measured using the 2-electrode arrays

The electrical data in Figure 4-9 was measured using a 2-electrode array (Figure D-1). This measurement was a potential difference between two electrodes:

$$A_{2el} = \Phi_a - \Phi_b. \tag{D.5}$$

If the Stoneley wave length is much longer than the distance between the electrodes, then this measurement, A_{2el}, is proportional to the first derivative of the electrical potential along the borehole axis, i.e., to the vertical component of the electrical field.

For the 2-electrode measurement technique, the ratio of the recorded signal to the electrical potential at the electrode a can be obtained by substituting Equation D.2 into Equation D.5. The resulting expression is:

$$\frac{A_{2el}}{\Phi_a}(\omega) = -2i \sin\left(\frac{\omega}{2c_s}l\right) \exp\left(i\frac{\omega}{2c_s}l\right), \tag{D.6}$$

and the amplitude ratio of the signal A_{2el} to the potential Φ_a at the electrode a is:

$$\frac{|A_{2el}|}{|\Phi_a|}(\omega) = 2\left|\sin\left(\frac{\omega}{2c_s}l\right)\right|. \tag{D.7}$$

As in the case with the 4-electrode measurement, the 2-electrode measurement records zero signal when the Stoneley wave length is equal to the distance between the electrodes because the signal on the electrode a cancels the signal on the electrode b. Figure D-3 shows the plot of the sensitivity function $\frac{|A_{2el}|}{|\Phi_a|}(\omega)$ of the 2-electrode measurement with a $0.5m$ spacing between electrodes. Zeros of the sensitivity function $\frac{|A_{2el}|}{|\Phi_a|}(\omega)$ correspond to the frequencies at which the distance between the electrodes is a multiple of a Stoneley wavelength.

Using Equations D.4 and D.7 we can calculate the amplitude of the electrical potential oscillation from the amplitudes of the signals measured in the field.

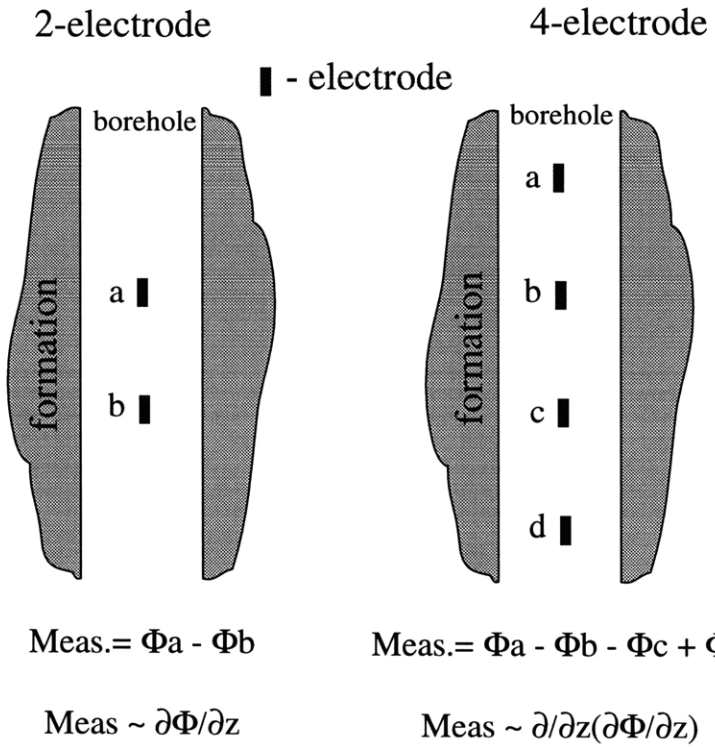

Figure D-1: Diagrams of the 2-electrode and 4-electrode measurements. If the Stoneley wave length is much larger than the distance between the electrodes, then the signal recorded by the 2-electrode array is proportional to the first derivative of the electrical potential in the borehole, and the signal recorded by the 4-electrode array is proportional to the second derivative of the electrical potential in the borehole.

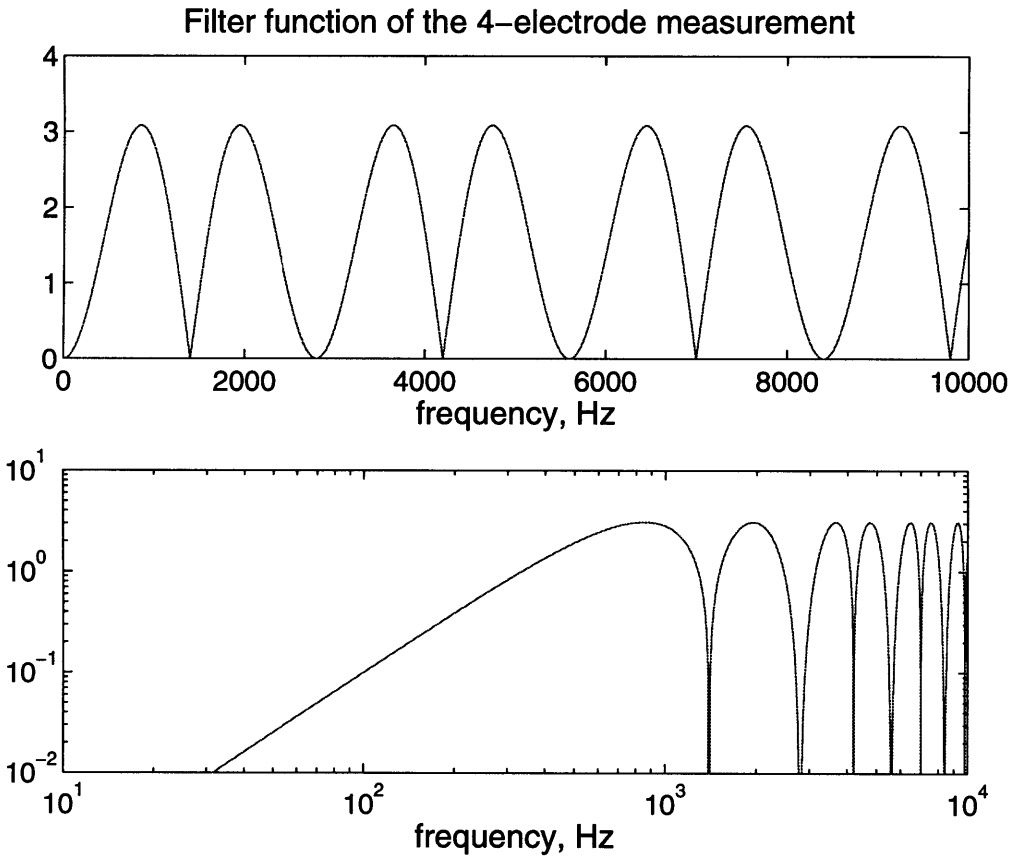

Figure D-2: The sensitivity function $\frac{|A_{4el}|}{|\Phi_a|}(\omega)$ of the 4-electrode measurement with a $0.5m$ spacing between the electrodes. Zeros of the sensitivity function $\frac{|A_{4el}|}{|\Phi_a|}(\omega)$ correspond to the frequencies at which the distance between the electrodes is a multiple of half of a Stoneley wavelength.

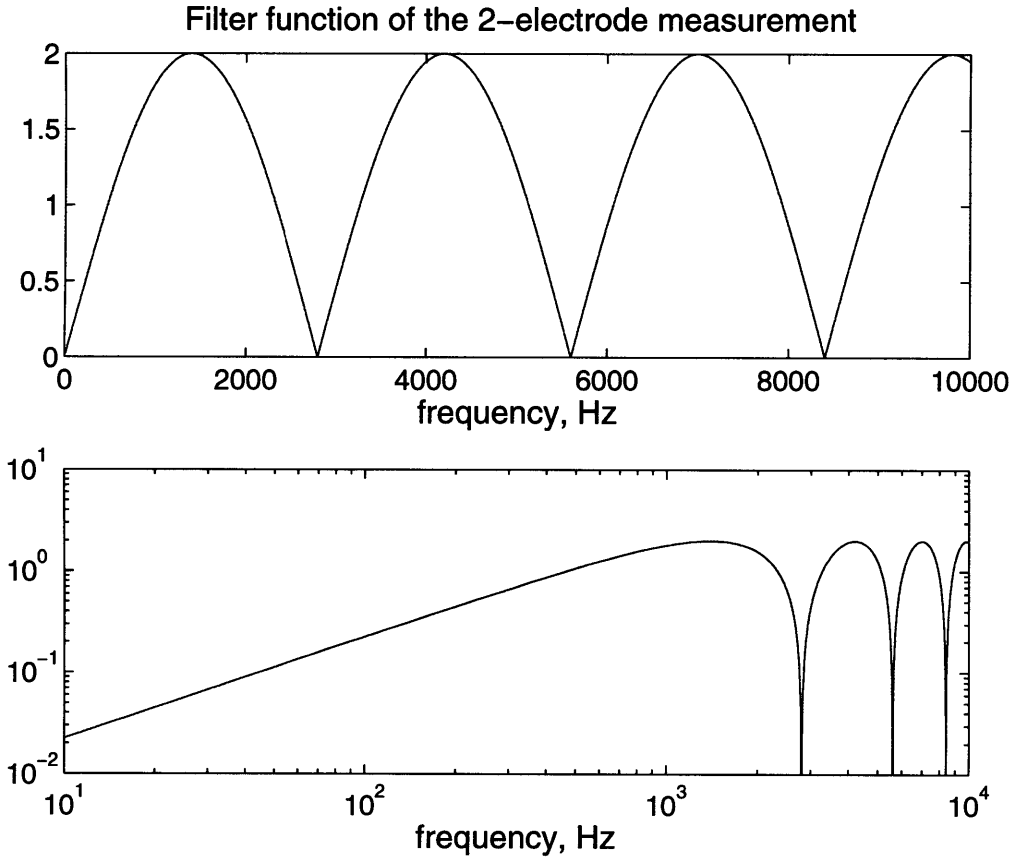

Figure D-3: The sensitivity function $\frac{|A_{2el}|}{|\Phi_a|}(\omega)$ of the 2-electrode measurement with a $0.5m$ distance between electrodes. Zeros of the sensitivity function $\frac{|A_{2el}|}{|\Phi_a|}(\omega)$ correspond to the frequencies at which the distance between the electrodes is a multiple of a Stoneley wavelength.

Appendix E

Instrument response of the measuring devices

In Chapter 4 we presented electroseismic data recorded using a high-frequency source. The amplitude-versus-frequency dependence of the electroseismic signals has a "dip" at the $800Hz$ frequency. To rule out the possibility of this "dip" being caused by the instrument response of our measuring devices, we measured this instrument response directly in the lab.

To measure the instrument response we placed the lead electrodes into a water tank and added a small amount of salt to the water so that the DC impedance between the electrodes was the same as that measured when the electrodes were in a borehole. We connected an AC current source consecutively with the electrodes, borehole cable and the data acquisition system. We kept the current amplitude constant and varied the current frequency. Figure E-1 shows the amplitude of the signal recorded by the data acquisition system at different frequencies normalized by the amplitude recorded at the frequency of $300Hz$. Figure E-1 demonstrates that the instrument response

is flat up to the frequency of $1500Hz$. Thus, the "dip" in the amplitude-versus-frequency dependence of the electroseismic signals at $800Hz$ was not caused by the instrument response.

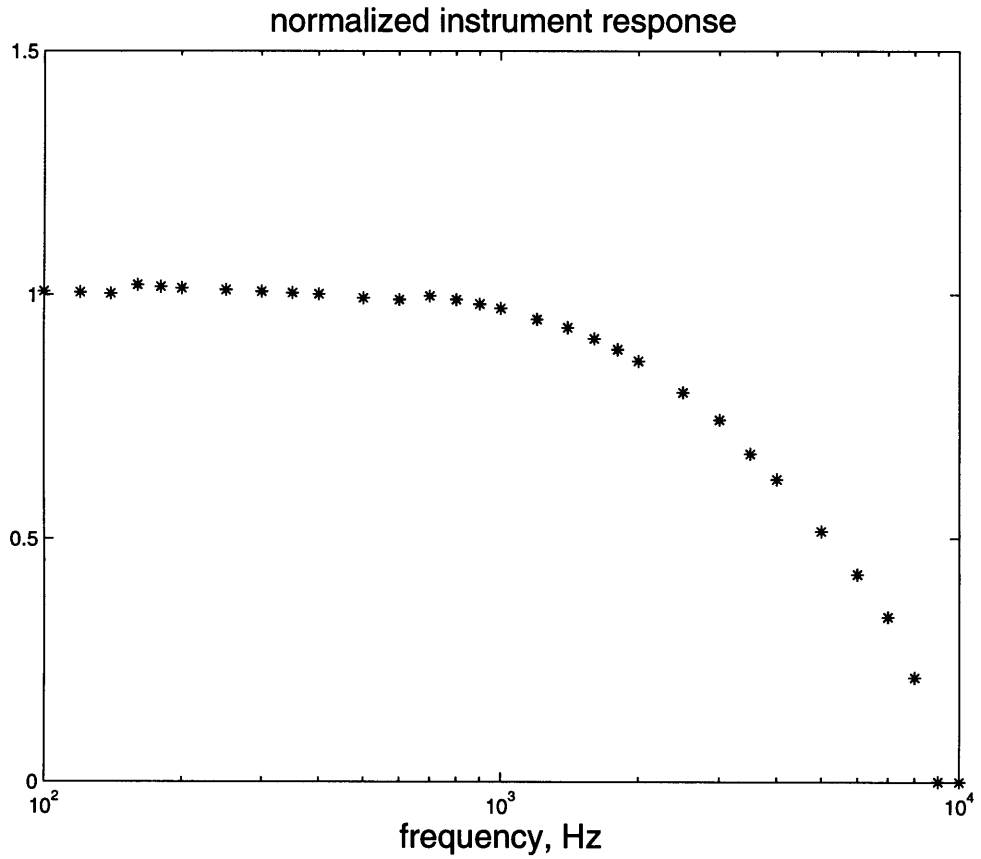

Figure E-1: The instrument response of our measurement device (data acquisition system — cable — electrode — water —electrode — cable). The instrument response is nearly constant up to the frequency of $1500Hz$.